View metadata, citation and similar papers at core.ac.uk
brought to you by CORE
provided by Digital Repository at the University of Maryland

ABSTRACT

Title of dissertation: LINEAR AND NONLINEAR ANALYSIS OF A GYRO-PENIOTRON OSCILLATOR AND STUDY OF START-UP SCENARIO IN A HIGH ORDER MODE GYROTRON

Muralidhar Yeddulla,
Doctor of Philosophy, 2005

Dissertation directed by: Professor Thomas Antonsen Jr.
Electrical Engineering Department

The Cyclotron Resonant Maser (CRM) is a device in which electrons gyrating in an external magnetic field produce coherent EM radiation. A DC electron beam current must be converted to an AC beam current to create RF energy. There are two possible approaches: phase bunching (O-type) and spatial segregation (M-type). In phase bunching, electrons are either accelerated or decelerated depending on when the electrons enter the interaction region, causing phase bunching. The electron bunches are then slowed down by the RF field for energy extraction. Not all electrons lose energy; some even gain energy. In spatial segregation, electrons entering the interaction region at different times are deflected in different directions. With an appropriate spatially varying RF field, all electrons can lose energy leading to very high conversion efficiency.

A CRM with a smooth walled cylindrical waveguide interaction cavity and an annular electron beam passing through it can generate very large amount of RF

energy. Depending on the electron beam position a gyrotron (O-type device) and a gyro-peniotron (M-type device) are possible.

In this work, first, a nonlinear theory to study CRMs with a smooth walled cylindrical waveguide interaction cavity is presented. The nonlinear set of differential equations are linearized to study the starting conditions of the device. A gyro-peniotron operating in the $TE_{0,2}$ - mode is studied using the theory presented. It is found that a gyro-peniotron operating in a low order mode can be self excited without mode competition from gyrotron modes, leading to the possibility of a very efficient high power RF source. A higher order mode gyro-peniotron experiences severe mode competition from gyrotron modes. The cavity Q required for gyro-peniotron operation is very high, which can lead to excessive heat in the cavity walls due to ohmic losses. Hence, a gyro-peniotron operation seems practical only in low order modes and in short pulses. Second, an existing linear theory of gyrotrons is extended to include effects of magnetic field tapering, cavity wall profile, finite beam thickness, velocity spread and axially dependent beam coupling to the fields of competing modes. Starting currents are calculated for the operating and the most dangerous competing mode in a 140 GHz gyrotron, which was developed at Communications and Power Industries (CPI). Start-up scenario of this device is also studied using the non-stationary code MAGY, which is a tool for modeling slow and fast microwave sources.

LINEAR AND NONLINEAR ANALYSIS OF A GYRO-PENIOTRON OSCILLATOR AND STUDY OF START-UP SCENARIO IN A HIGH ORDER MODE GYROTRON

by

Muralidhar Yeddulla

Dissertation submitted to the Faculty of the Graduate School of the
University of Maryland, College Park in partial fulfillment
of the requirements for the degree of
Doctor of Philosophy
2005

Advisory Committee:

Professor Thomas Antonsen Jr., Chair/Advisor
Dr. Gregory Nusinovich, Co-Advisor
Professor Victor Granatstein
Professor Thomas E. Murphy
Professor James Drake

To my mother for all her love.
If there is such a thing as God's Love, It cannot be better than Mother's Love.

ACKNOWLEDGMENTS

It is with a heart full of gratitude that I thank my adviser Prof. Thomas Antonsen Jr. for giving me an opportunity to work in a very challenging and exciting field and guiding me through it for the past four years. No words will be enough to thank Dr. Gregory Nusinovich who as my co-adviser has taught me very patiently through many hours every week, the intricacies of gyro-devices. I am indeed fortunate for having had an opportunity to work with such wonderful teachers and researchers.

I thank Prof. Victor Granatstein for encouraging me to come to the University of Maryland and for being on my dissertation committee. I also thank Prof. James Drake and Prof. Thomas Murphy for agreeing to be on my dissertation committee. Many thanks are also due to Dr. Alexander Vlasov who helped me greatly with the use of the code MAGY.

I also thank my advisers during my Masters at the Banaras Hindu University, India, Prof. B.N. Basu and Dr. P.K. Jain for introducing me to the field of gyro devices and for encouraging me in my research pursuits.

I will forever be indebted to my friend Mangipudi Ramesh without whose help and encouragement at a very critical stage of my life, I could not have taken up graduate studies. I thank him from the bottom of my heart.

I am indeed very fortunate to have had a wonderful office mate, Paul Cassak.

Paul has been my friend, confidant and a very helpful office-mate always ready to help or discuss anything whether it be research problems, physics, mathematics, politics or philosophy! I also had a wonderful time in the company of my other office-mate Haihong Che who has always enlivened the office with her cheerfulness. Special mention is also due to Prof. Niranjan Ramachandran, Kaipa Vinod and Ayush Gupta for all their help and for being my friends.

I also thank my other friends Ashwin, Sreyas, Dr. Prasad, Manoj, Kartik, Dinesh, Arun, Vikas, Chia Ying Huang, Alexander Sinitsin, Roland, Vamsi, Asitav, Ajuer and many others because of whom life as a graduate was such a pleasant and memorable experience. I should also mention my music teacher Raghavendra Batni who made life a joy with his music. My thanks are also due to the supporting staff of our institute and especially to Mohini for being always helpful and full of cheer.

Finally, the most important people in my life - my parents, brothers and sister. My father is physically handicapped, yet, he has shown through his life that there is no adversity human spirit cannot conquer. My mother has always been full of love and patience. I can never thank my parents enough for everything they have done for me. They are the source of the highest inspiration for me. I lovingly thank my two brothers and sister for always being there for me.

Contents

List of Figures

Chapter 1

Introduction

1.1 Importance of Cyclotron Resonance Masers

Cyclotron Resonance Masers (CRMs) belong to a class of microwave devices known as fast wave devices. In these devices, the phase velocity of the electromagnetic (EM) wave is greater than the speed of light in the interaction region where the interaction between the EM wave and an intense beam of electrons takes place. The first publications on the CRM mechanism appeared in 1958-59 [3, 4, 5]. A CRM was successfully tested in the early 1960's in the USSR and was reported in [6] in 1967. This first CRM generated a very modest power of 6W Continuous Wave (CW) power at 9.1 GHz. The next major development also happened in the USSR when high average power millimeter wave CRM oscillators (known as gyrotrons) were developed. The first U.S. gyrotron oscillator was developed at the Naval Research Laboratory in 1980[7]. Since then there has been tremendous progress in the technology of these devices at many different places throughout the world. In

recent times, there have been significant advances in microwave tube technology for generation of megawatt level, long-pulse (approaching CW operation) EM waves in the millimeter and sub-millimeter wavelength regions [8]. CRMs have proved to be the most successful devices in this regard.

One of the major research thrusts in the USA today is the development of controlled fusion reactors. EM radiation is required for plasma formation, heating, current drive, profile control and diagnostics. The confined plasmas are heated with microwaves and millimeter waves. Ion Cyclotron Resonance Heating (ICRH) requires frequencies of $\sim$ 100 MHz; lower hybrid heating requires 0.5 - 5 GHz; and Electron Cyclotron Resonance Heating (ECRH) requires $>$ 100 GHz. Depending on the scale of the reactors, the microwave power required for this heating ranges from several megawatts to tens or even hundreds of megawatts. While microwave sources for ICRH and lower hybrid heating were available for a very long time, high power sources required for ECRH were possible only with the advent of gyrotrons. Gyrotrons have been reliably used in the ECRH experiments. In the frequency range and power levels required for ECRH, no other EM source has been as efficient as a gyrotron. In the past few years gyrotrons delivering $>$ 1 MW power at frequencies $>$ 100 GHz in long pulses ($>$ 1 second) have been developed successfully [8]. This can be a very important factor for the success of the future fusion reactors. At present, research in gyrotrons is being focused on how to further improve the output power levels, efficiencies and pulse duration which can significantly reduce the costs of fusion experiments.

1.2 Statement of the problems addressed

In this work we are mainly concerned with the operation of gyrotrons and gyro-peniotrons. Both these devices belong to a class of CRMs in which a beam of electrons gyrate through a metallic cavity in the presence of a strong external magnetic field. Though several different configurations are possible for these devices, in this work we study only a configuration where an annular beam of electrons from a Magnetron type Injection Gun (MIG) pass through a cylindrical cavity while interacting with EM waves.

Gyro-peniotrons have a potential for very high efficiency operation ($> 90\%$). However, the gyro-peniotron interaction mechanism is weak compared to that of a gyrotron. Therefore, modes operating in the strong gyrotron interaction mechanism are generally more likely to trigger ahead of a gyro-peniotron mode causing the latter mode to be suppressed. In this work we study the conditions under which a gyro-peniotron can operate.

We have developed a nonlinear theory for gyrotrons and gyro-peniotrons which can be used to study the electron motion (including the guiding center motion) and the evolution of EM modes inside a cylindrical cavity structure. This nonlinear theory can also be used to study mode competition when multiple modes are present. We have also developed a linear theory using the set of differential equations describing the electron interaction developed in the nonlinear theory. We have studied the starting conditions for the excitation of a $TE_{0,2}$ - gyro-peniotron mode and potential mode competition due to gyrotron modes using the linear theory. Using the

nonlinear theory we have studied the efficiency of the $TE_{0,2}$ - mode under various operating conditions.

We have found that when operated in low order TE modes like the $TE_{0,2}$ - mode, a gyro-peniotron can be excited with no competition from neighboring gyrotron modes. Thus, development of a very high power and a highly efficient gyro-peniotron oscillator seems possible. Within our knowledge, this is the first time that the possibility of self excitation of a gyro-peniotron oscillator is being reported.

Another problem that we have addressed in this work is mode competition in high power ($>$ 1 MW) and high frequency ($>$ 100 GHz) gyrotrons. In order to operate at these levels of power and frequency, the gyrotron should necessarily be designed to work at a very high order mode. As the density of modes around such a high order mode is high, more than one mode can satisfy the self excitation conditions which can lead to mode competition. It is a very difficult design problem to ensure that the device operates only at the desired mode while suppressing all other competing modes.

We have studied a 140 GHz gyrotron developed by Communication and Power Industries which is capable of delivering $\sim$ 1 MW in long pulses in the $TE_{28,7,1}$ - mode. When the initially designed device was tested it was found that an undesirable counter rotating $TE_{-25,6,1}$ - mode dominated. We have studied this problem using a non-stationary code, MAGY, and also an existing linear theory which we have extended to account for non-ideal conditions like the tapering in magnetic field and cavity structure, electron velocity spread and finite thickness of the electron beam.

Our study indicates that the electron beam was positioned where the coupling with the undesirable $TE_{-25,8,1}$ - mode was slightly higher than for the designed $TE_{28,7,1}$ - mode. CPI has redesigned the device where the electron beam was positioned for maximum coupling with the desired mode. It was experimentally verified that in the new design the required mode alone dominates, which we have also verified using our linear theory and MAGY studies.

1.3 Basic operation of CRM devices

There are many different configurations possible to produce coherent radiation based on electron cyclotron maser instability. Depending on the beam characteristics and its position inside the interaction region, various CRMs like gyrotrons, peniotrons, gyro-peniotrons, cyclotron auto resonant masers and auto resonant peniotrons are possible. In any CRM, before the electrons enter the interaction region, the electron beam constitutes a DC current. This DC beam current has to be converted into AC current to create RF energy. In general in a CRM, electrons gyrate in an external magnetic field and move axially through an interaction region. As the electrons move in helical orbits, the electron energy is distributed between the transverse (orbital) and axial velocities. As the electrons pass through the interaction region, they interact with the EM waves present in the interaction region. Usually, CRMs operate in transverse electric (TE) EM modes. The transverse velocity components of electrons interact with the transverse electric field of the TE modes. This interaction between the EM wave and the electrons converts the elec-

tron beam current from DC to AC. When the electron cyclotron frequency ω_{c_0} (or its harmonic $s\omega_{c_0}$) and the Doppler-shifted wave frequency, $\omega - k_z v_z$, satisfy the cyclotron resonance condition, $\omega - k_z v_z \approx s\omega_{c_0}$, it is possible to generate coherent EM radiation. Here ω is the angular frequency of the EM wave, k_z is the axial wave number and v_z is the axial velocity of the electrons. For the EM wave to grow the electrons should, on an average, give up more energy than they absorb from the EM wave.

Electrons can interact with the EM waves in two different ways. If some electrons lose their energy and others gain energy from the EM wave in each cyclotron period of their interaction with the EM wave, then due to the relativistic dependence of cyclotron frequency on electron energy, the electrons start to gyrate with slightly different frequencies which results in the orbital or phase bunching. If the frequency of the interacting mode, ω, slightly exceeds the cyclotron frequency of the electron (or its harmonic), the phase bunched electrons find themselves in regions of decelerating electric field of the interacting TE mode, then the bunched electrons continue to give up their kinetic energy to the growing EM wave. Fig.1.1 shows how the bunching process happens in a ring of electrons in a gyrotron. This type of electron wave interaction characterized by electron phase bunching, is similar to that in linear-beam devices (klystrons, TWT's, BWO's) whose operation is also based on electron bunching. All such devices are known as O-type devices and, correspondingly, the electron-wave interaction in them is usually referred to as O-type interaction.

On the other hand there is another interaction mechanism where all electrons,

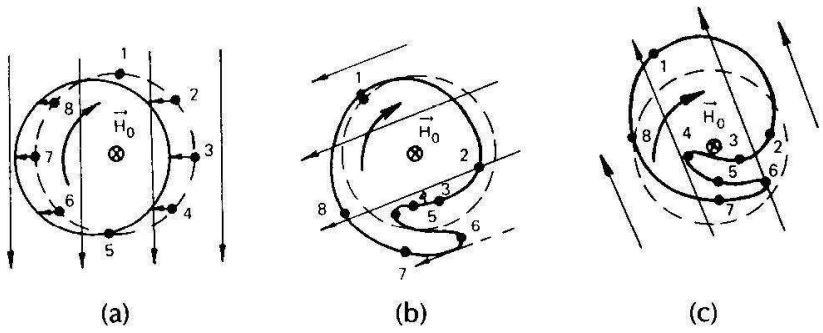

Figure 1.1: Interaction in a ring of electrons differing in the initial phase of gyration with a circularly polarized RF electric field **E**. (a) Initial modulation of electrons by the RF field. The electron ring is shifted under the action of crossed fields (**E** and $\mathbf{H_0}$). (b) Inertial phase (orbital) bunching caused by the difference in the cyclotron frequencies of electrons. (c) Deceleration of the electron bunch in the RF field having frequency slightly higher than the initial cyclotron frequency of electrons.(Reproduced from [1])

irrespective of their phase relation to the RF electric field, give up their kinetic energy. In this interaction all the electrons encounter both accelerating and decelerating RF fields in every cyclotron period. As electrons enter the interaction region with different phase relations to the RF field, each electron is spatially deflected in a different direction. The action of the transversely nonuniform RF fields on the electrons can be such that the electrons encounter stronger decelerating fields than accelerating fields. As the RF electric field and the DC magnetic field, B_0, are perpendicular to each other, there exists a $\mathbf{E} \times \mathbf{B}$ drift of the electrons which causes the electron guiding centers to drift. The electron orbits drift in different directions, causing spatial segregation of the electron orbits. This type of interaction characterized by a drift in guiding centers and spatial segregation of the electrons is known as the M-type interaction. Correspondingly, the devices based on electron motion in crossed fields (magnetrons and their varieties) are known as M-type devices.

Due to the nature of O-type interaction, not all electrons are gathered in a bunch to give up their kinetic energy; some actually absorb energy from the EM wave. On the contrary, as all electrons give up their kinetic energy in M-type interaction, there are no "bad" electrons. Hence, M-type interaction is more efficient in energy conversion than O-type interaction. In general, in CRMs both O-type and M-type interactions take place. However, when O-type interaction is dominant a CRM is popularly known by the name gyrotron and when M-type interaction is dominant the device is categorized as a peniotron [9].

O-type interaction dominates when the electron beam is positioned for maximum coupling with the operating TE mode, which causes phase bunching. As there

is no special cavity geometry necessary to achieve this, a smooth-wall cylindrical structure is generally used for the resonant cavity of a gyrotron (which is an O-type device) to increase the power handling capacity of the device. Though gyrotrons are capable of delivering large amounts of output power, their overall energy conversion efficiency is only $\sim 30 - 40\%$ [8]. The reason for this is twofold. (a) Gyrotrons usually operate at frequencies near cutoff. Near cutoff the RF magnetic fields are very weak and have very little effect on the electron motion. The transverse RF electric field that is present can affect only the transverse component of the electron velocity. So, neither the electric and magnetic RF fields affect the axial component of the velocity of the electrons. Therefore, a significant amount of energy associated with electron axial motion does not participate in energy conversion. (b) Not all electrons find themselves in a favorable phase with respect to the EM wave, to give up their transverse kinetic energy. So, not all the transverse kinetic energy of the electrons is converted into useful energy. To enhance the overall efficiency, depressed collectors can be used to recover part of the unused energy from the spent beam [10].

In conventional peniotrons, a thin helical beam is placed at the center of a double-pair ridged waveguide as shown in Fig. 1.2 [2, 11]. As the EM field is concentrated near the ridges of such a waveguide, there is a transversely nonuniform interaction between the electrons and the RF wave, meeting the requirements for M-type interaction. Though a conventional peniotron has higher efficiency than a gyrotron, from the point of view of high-power operation, it is inferior because (a) the usable electron beam current is limited to a value much smaller than that of

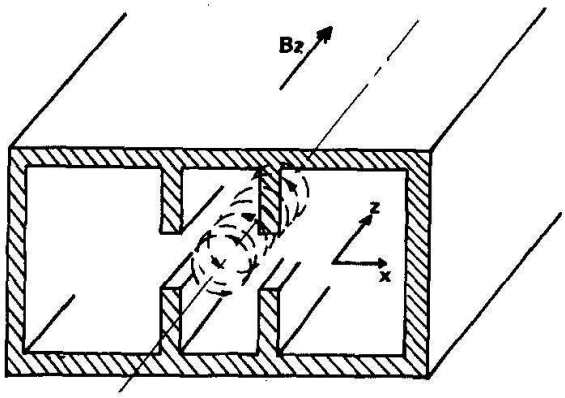

Figure 1.2: Double pair ridged waveguide structure for a travelling wave peniotron (Reproduced from [2])

a gyrotron as only a thin pencil beam of electrons (not an annular beam) can be used and (b) extremely high RF electric fields arise near the ridges. However, for the same interaction structure as that of a conventional gyrotron (a smooth-wall waveguide), it is possible to obtain peniotron operation by positioning the electron beam such that the center of the electron orbits in each beamlet coincides with a null of the interaction mode. Such a hybrid device is known as gyro-peniotron and was first proposed by Ono and others in 1984 [2]. Then, just the field non-uniformity on electron orbits will cause spatial segregation of electrons due to M-type effects. Such a device can combine the advantages of high-power operation of a gyrotron and the high efficiency of a peniotron.

In both O-type and M-type interaction mechanisms, for energy to be extracted from the electron beam the frequency of the EM wave, ω, and the electron cyclotron frequency ω_{c_0} have to be related by the following beam-mode dispersion relation

$$\omega \pm k_z v_z \cong s\omega_{c_0} \tag{1.1}$$

where k_z is the axial wave number, v_z is the axial velocity of the electron beam, $\omega_{c0} = eB_0/\gamma m_0 c$ is the cyclotron frequency of an electron in a magnetic field B_0, s is the harmonic number ($s = p$ for gyrotrons, $s = 2p$ for double pair ridged waveguide peniotrons and $s = 2p - 1$ for gyro-peniotrons, where p is an integer [2]), e is the electron charge, c is the velocity of light in free space, m_0 is the electron rest mass and γ is the relativistic factor. The product $k_z v_z$ represents the Doppler shift in the cyclotron frequency. The '$\pm$' sign in (1.1) corresponds to a wave propagating backwards or forwards, respectively.

In general, the electrons interact not only with the electric field of the TE mode, but also with the RF magnetic field (see e.g., [12]). The RF electric field changes the electron's energy and consequently the orbital cyclotron frequency ω_{c0} causing electron bunching (O-type interaction). At the same time the RF electric field causes a radial drift of the electron orbits (M-type interaction). The transverse RF magnetic field acting upon gyrating electrons yields the axial component of the RF Lorentz force, which affects the axial velocity of electrons causing the axial bunching of electrons. The axial bunching mechanism, which acts on the Doppler shift term $k_z v_z$, was first discussed in [3, 13, 14]. The two mechanisms, orbital and axial bunching, proceed in such a way as to offset each other's bunching process. The orbital bunching dominates in the case of fast waves ($\omega/k_z > c$) and the axial bunching dominates in the case of slow waves ($\omega/k_z < c$). There is also a regime when k_z is close to ω/c. When $k_z = \omega/c$, these two bunching mechanisms completely cancel each other [15]. Remarkably, this effect of mutual cancellation of changes in the cyclotron frequency and axial velocity in the cyclotron resonance condition for

a wave with $k_z = \omega/c$, (1.1) manifests itself even in the case of a single electron. For such a particle, once the cyclotron resonance condition (1.1) is fulfilled at the entrance to the interaction space, it is maintained throughout the interaction region. This effect is known as auto-resonance [16, 17]. The O-type CRM which operates near the auto-resonance is known as the Cyclotron Auto Resonant Maser (CARM), first suggested by Petelin in 1974 [18]. As both the transverse as well as axial component of the electron kinetic energy is converted into useful energy, the CARM potentially has a very large conversion efficiency [19]. There is an added advantage of lower magnetic field requirement in a CARM driven by relativistic electron beam, due to the Doppler frequency up-shift when compared to CRM operation [20, 21].

When operation is close to auto-resonance the O-type interaction is suppressed, as the azimuthal and axial bunching effects cancel each other, making the M-type interaction visible. Thus, it is possible to obtain dominant M-type interaction either by placing the beam where there is zero coupling with the mode that can be excited due to O-type bunching, or by operating close to the auto-resonance or a combination of both. In 1987, Baird and others proposed a new device known as the Auto Resonant Peniotron (ARP) where a peniotron works in an auto-resonant regime similar to a CARM [22]. As ARPs combine both the peniotron as well as auto resonance interactions, the electron kinetic energy can be fully converted into useful RF energy. Therefore, an ARP has a potential for close to 100% energy conversion efficiency [22, 23, 24, 25].

Working in the auto-resonant regime requires an electron beam with very small electron velocity spread. As the relation (1.1) should be tightly balanced

throughout the interaction period for auto-resonance to be sustained, there is very little tolerance to any variation in axial velocity component v_z. It has been observed that even a 1% velocity spread is generally not tolerated for auto-resonance devices [21]. Thus, an electron gun producing a very high quality, high-energy beam will be necessary for proper auto-resonance operation. As the current density of the electron beam increases, the velocity spread due to space charge effects increases as well, affecting the beam quality. Thus very large beam currents are not possible for auto-resonance operation, limiting the output power possible. The maximum efficiency that has been recorded for a CARM is only 26% (see [26]), due to the limitations of the electron gun.

1.4 Some comments on previous works on gyro-peniotron

The gyro-peniotron oscillator was first proposed by Ono *et al.*, in 1984[2]. Using a nonlinear theory they have shown that a gyro-peniotron oscillator can generate very high power at high efficiencies. However, they had assumed an electron beam with unrealistically high beam power in their simulations because of which it is difficult to assess the practical feasibility of a gyro-peniotron from their results.

In 1985 Vitello and Ko published a linear analysis of a gyro-peniotron [27]. According to the theory they developed it seems unlikely that a gyro-peniotron mode can be self excited when the beam is placed on the waveguide "null" of the

RF mode to be excited. Therefore, they propose that the electron beam be placed away from the RF null for self excitation of the gyro-peniotron mode. However, [2] predicts that the electron beam has to be placed right on the RF null for maximum efficiency operation. Moreover, Vitello and Ko also conclude that even when the electron beam is placed away from the null, due to severe mode competition from gyrotron modes, the gyro-peniotron mode cannot be excited.

There are several research papers available in the literature where gyrotron amplifiers are studied. Many of these papers develop generalized dispersion equations that accounts for both O-type as well as M-type effects to study the linear characteristics of the amplifier. It has been observed that the dispersion equation in some papers [28, 21, 29] show that a gyro-peniotron mode can have a linear growth when the electron beam is placed on the RF null while the dispersion equation given in other literature [27, 30, 9, 31] show that the gyro-peniotron mode cannot have linear growth for the same beam position.

In [32, 33], Döhler shows that it is necessary to include a dipole current term due to the periodic radial deformations of the electron beamlets when deriving the dispersion equation. He shows that only when this dipole current term is included the dispersion equation will show a term responsible for the growth of a gyro-peniotron mode when the electron beam is placed on the RF null. Therefore, it seems that if a dispersion equation that predicts no growth when the device is configured as a gyro-peniotron, then it is likely that the dipole current which Döhler discusses in [33] is neglected.

In the present work we have developed a linear theory for a gyro-peniotron

oscillator where we consider perturbations in transverse momentum, phase and guiding center position of the electron. Our results show that self excitation conditions can be fulfilled for a gyro-peniotron even when the electron beam is positioned on the RF null. Also, the non-linear theory we have developed in this work shows the possibility of excitation of a gyro-peniotron mode in the linear regime.

1.5 Mode competition in gyrotron oscillators

If the output power of the gyrotrons is to be increased, then the size of the interaction cavity needs to be increased in order to handle the increased levels of ohmic losses of microwave power in the cavity walls. Then the device needs to operate at high order modes. As the order of the operating mode increases, the device needs to operate in an increasingly denser spectrum of competing modes. This can lead to mode competition from these "parasitic" modes. For efficient operation the device should operate only at the design mode. If any other mode is established, then the operation of the device will necessarily be less efficient. As gyrotrons are constructed for efficient operation in the required mode alone, it is an extremely difficult problem to ensure that the required mode dominates over all other modes even for a gyrotron [34, 35, 36]. In order to ensure that only the design mode is established, it is necessary to understand many factors that contribute to the excitation of modes in a gyrotron. Generally, it is more likely that the mode whose self excitation conditions are first satisfied during the voltage and current rise during the start-up of the device will be established. This is because the mode that starts

growing first is more likely to suppress any other competing mode. Therefore, it is a good design idea to ensure the design mode is triggered ahead of other competing modes. However, sometimes it is not possible to trigger the design mode ahead of parasitic modes due to the characteristics of the electron gun being used as well as due to the very high density of competing modes. In such a situation the design should ensure that though a parasitic mode is first triggered, it should either go out of resonance or get suppressed while the design mode gets established during start-up. Therefore, any design of a gyrotron requires a careful study of start current characteristics as well as the start-up scenario.

We have made an in-depth study of the start-up scenario in a 140 GHz gyrotron being developed by Communications and Power Industries (CPI) for electron cyclotron current drive in a new German stellarator Wendelstein-7X. This gyrotron operates in the $TE_{28,7,1}$–mode delivering almost 1 MW-level output power in near CW operation. The first design of this device generated an undesirable counter-rotating $TE_{-25,8,1}$–mode . We have studied the problem by extending an existing linear theory [37] for start current analysis to include the effects of magnetic field tapering, cavity profile, finite beam thickness, velocity spread and axially dependent beam coupling to the fields of competing modes [35]. Our studies suggest that the radial position of the electron guiding centers is the most critical parameter that determines which mode survives the mode competition. It was found both theoretically and experimentally that the start-up in an improved gyrotron results in satisfactory operation.

1.6 Thesis outline

In chapter 2, a brief working principle of gyrotrons and gyro-peniotrons is presented along with the issues of soft and hard excitation of microwave oscillators. In chapter 3 we discuss the various regimes of operation of a CRM using a dispersion relation developed by Li, Park and Hirshfield [28]. In chapter 4 we present a derivation of nonlinear equations governing electron beam-wave interaction and multimode analysis of a CRM in a cylindrical cavity. In chapter 5 we develop a linear theory using the nonlinear equations developed in chapter 4. In chapter 6, we present extensive analysis of a gyro-peniotron working in the TE_{02}-mode using nonlinear theory. We also present the starting conditions under which a gyro-peniotron mode can be excited and possible mode competition due to gyrotron modes using linear theory.

In chapter 7, a theory for the calculation of start current that includes non-ideal beam characteristics, magnetic field profile and cavity profile is described. In chapter 8, an in-depth analysis of a CPI 140 GHz gyrotron using the theory developed as well as using the non-stationary code MAGY is presented.

In chapter 9 we discuss results of this work and possibilities for future work.

Chapter 2

Working principle of gyrotrons and gyro-peniotrons

In both gyrotrons and gyro-peniotrons an annular beam of electrons gyrate through a smooth walled cylindrical cavity interaction region in the presence of a strong DC magnetic field. As the electrons stream down the interaction cavity, they interact with EM waves. On an average, the electrons lose energy to the wave causing the EM wave to grow. The difference between the gyrotron and gyro-peniotron lies in the way the electrons interact with the EM wave. This depends on where the beam is positioned with respect to the EM wave. We will examine both mechanisms in turn. For our analysis, we shall consider a $TE_{0,2}$ - mode in a cylindrical waveguide, though the discussion is valid for any other mode.

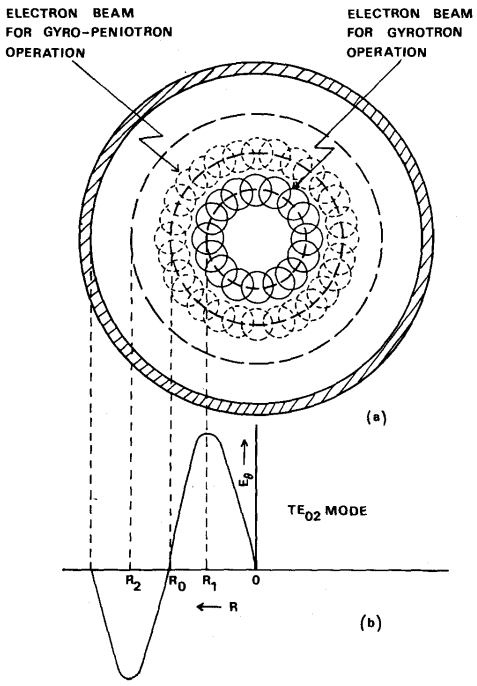

Figure 2.1: (a) Cross-section of interaction space of a gyrotron and a gyro-peniotron operating in the $TE_{0,2}$ - mode; (b) RF electric field distribution in the radial direction. (Reproduced from [2])

2.1 Fundamental harmonic gyrotron

In a fundamental harmonic gyrotron, the electron beam is placed in regions where there is maximum interaction with the mode with which it is interacting. Fig.2.1 shows a cross section of the interaction region with the annular electron beam. The beam is represented by a set of circles placed along the annulus as shown. Each circle represents an electron "beamlet" which is a cross-sectional view of the path of an electron as it gyrates in the presence of an external DC magnetic field. The annulus with solid circles represents the electron beam placed for maximum interaction with the operating $TE_{0,2}$ - mode which is ideal for fundamental harmonic gyrotron interaction. The annulus with dashed circles represents an electron

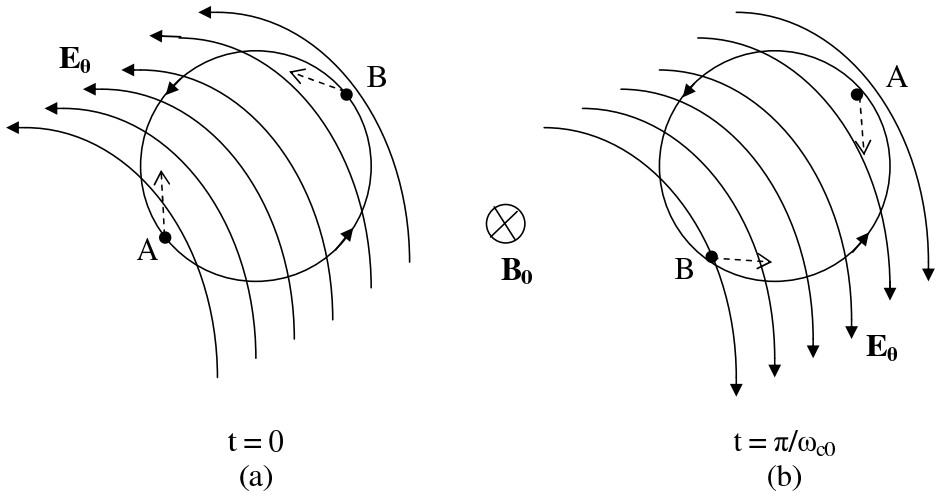

Figure 2.2: Gyration of two test electrons over one period of the gyro-cycle for fundamental harmonic gyrotron interaction

beam positioned for gyro-peniotron interaction. We shall take up gyro-peniotron interaction in the next section.

The gyrotron is generally operated close to the waveguide cutoff when the axial wave number is very small. The electron beam is assumed to be sufficiently thin that the RF electric field does not vary much over the thickness of the beam. For synchronous interaction,

$$\omega \cong \omega_{c_0}$$

where ω is the frequency of the RF field, ω_{c_0} is the electron cyclotron frequency.

Let us consider a beamlet in which all electrons are distributed uniformly at the entrance of the interaction cavity. To simplify the discussion, let us consider two "test" electrons which are opposite in phase with each other as shown in Fig.2.2a. Let us call these electrons "electron A" and "electron B". For the direction of the RF electric field shown, electron A is accelerated while electron B is decelerated. After

half gyro cycle ($t = \pi/\omega_{c_0}$), the direction of the RF electric field reverses (Fig.2.2b). Thus electron A which was initially accelerated continues to be accelerated, gaining kinetic energy from the RF wave, while electron B continues to be decelerated losing energy to the RF wave. After one complete RF cycle ($t = 2\pi/\omega_{c_0}$), the phase relationship between the electrons and the RF electric field will be similar to that at time $t = 0$ (Fig.2.2a).

An electron that is accelerated gains energy while an electron that is decelerated loses energy. As the cyclotron frequency is given by

$$\omega_{c_0} = \frac{eB_0}{\gamma m_0 c}$$

an electron that gains (loses) energy will have a larger (smaller) relativistic factor γ and hence smaller (larger) cyclotron frequency. Thus electron A will fall back in phase while electron B will move forward in phase (as shown by the dotted line arrows in Fig.2.2) and tend to phase bunch after a few gyro-cycles.

If the electrons and RF wave are in perfect synchronism, i.e., if $\omega = \omega_{c_0}$, then those electrons that are initially accelerated will continue to be accelerated and those electrons initially decelerated will continue to be decelerated throughout the interaction process. Thus, there will be no net exchange of energy between the electrons and the EM wave. In order for the EM wave to grow, there should be net transfer of energy from the electrons to the wave. To achieve this, there should be a slight mismatch in the synchronism condition such that

$$\omega \gtrsim \omega_{c_0}$$

when those bunched electrons in the accelerating phase move into the decelerating

phase. Then, as the bunched electrons are all decelerated, a net transfer of energy from the electrons to the EM wave becomes possible which leads to the growth of the EM wave. However, it should be remembered that there will always be a few "bad" electrons that are not gathered in the bunch which find themselves in the accelerating phase of the RF electric field, and hence absorb energy from the RF fields. Hence, the efficiency of a gyrotron is limited. It should also be noted that the interaction process in a gyrotron has very little effect on the guiding center position of the electrons.

2.2 Second harmonic gyrotron

Let us now consider the case where the electron beam is positioned as shown by the dotted line circles (beamlets) in Fig. 2.1 such that the guiding centers of the electron beamlets are located at the RF null of the $TE_{0,2}$ - mode. For operation in the second harmonic, the RF frequency is approximately twice the cyclotron frequency:

$$\omega \cong 2\omega_{c_0}.$$

The RF electric field has opposite phase on either side of the guiding center. We will consider four test electrons as shown in Fig.2.3a. Electrons A and C are initially accelerated and fall back in phase while electrons B and D are unaffected as they move perpendicular to the RF electric field. After a quarter gyro-cycle, the RF electric field changes phase by 180^0 (Fig. 2.2b). Now, electrons B and D are in decelerating phase and gain in phase while electrons A and C are unaffected. In the

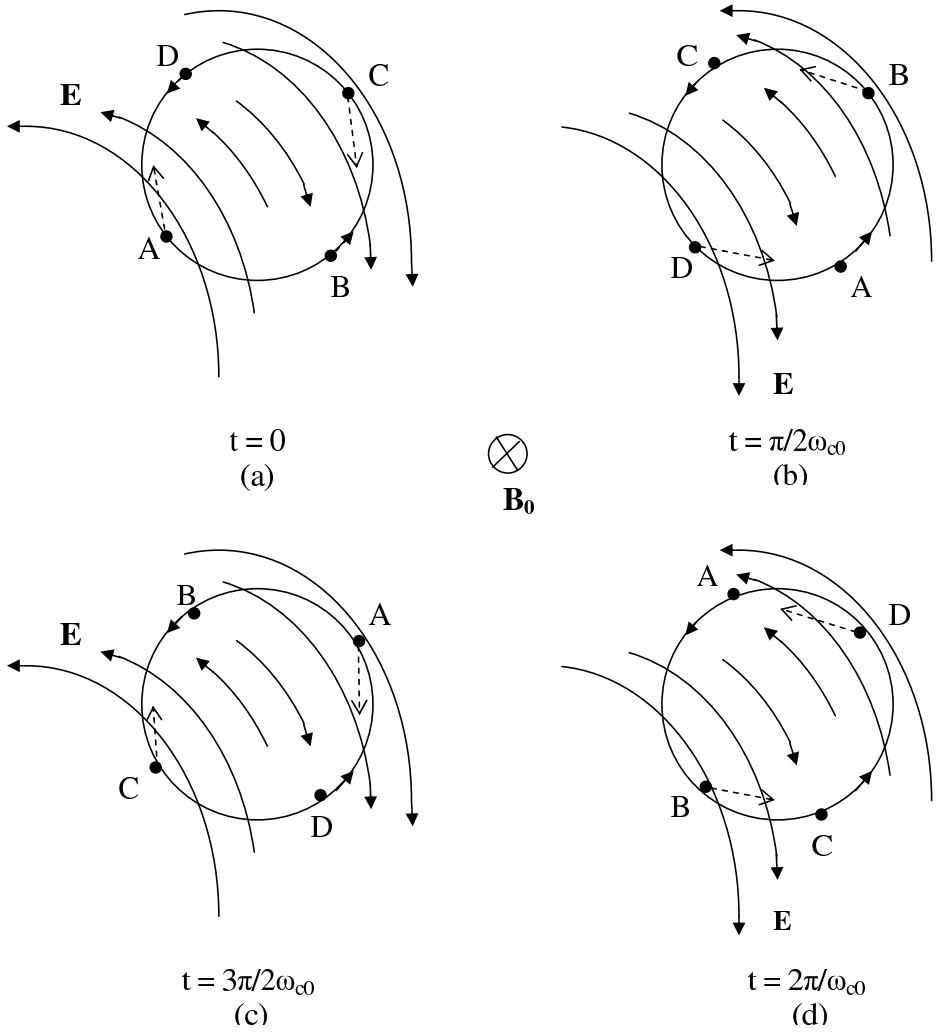

Figure 2.3: Gyration of four test electrons over one period of the gyro-cycle for second harmonic gyrotron interaction

process, electrons A and B tend to phase bunch so also electrons C and D. At half gyro-cycle, from Fig.2.2c, we see that electrons A and C are once again decelerated while electrons B and D are unaffected. At three quarters of a gyro-cycle electrons B and D are accelecrated (Fig.2.2d) while electrons A and C are unaffected. The cycle is then repeated over many gyro-cycles. Thus, we see that electrons A and C are always decelerated while electrons B and D are always accelerated if $\omega = 2\omega_{c_0}$, thus forming two sets of electron bunches. If $\omega \gtrsim 2\omega_{c_0}$, then both bunches find themselves in decelerating regions of the RF electric field and the EM wave can grow.

2.3 Gyro-peniotron

In the case of a gyro-peniotron, the electron beam is positioned as shown by the dotted line circles (beamlets) in Fig. 2.1, just as in the case of a second harmonic gyrotron described in the previous section. However, for a gyro-peniotron, the operation is in the fundamental (or odd) harmonic. An axial cross-sectional view of a CRM with the beam positioned for gyro-peniotron interaction is shown in Fig. 2.4. In order to study this case we consider two test electrons A and B entering the interaction region in the accelerating and decelerating phase as shown in Fig. 2.5 and Fig. 2.6, respectively.

As the orbital velocity of electron A increases due to the RF electric field, its Larmor radius also increases following the relation $\omega_{c_0} = v_\perp / r_L$ where $v_\perp$ is the electron orbital velocity and r_L is its Larmor radius (see Fig.2.5a). Correspondingly, the Larmor radius of electron B reduces (see Fig.2.6a). After a half gyro-cycle, the

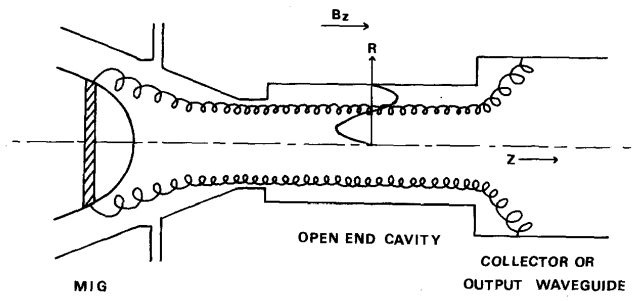

Figure 2.4: Structure for a gyro-peniotron oscillator operating in the $TE_{0,2,1}$ cavity mode. (Reproduced from [2])

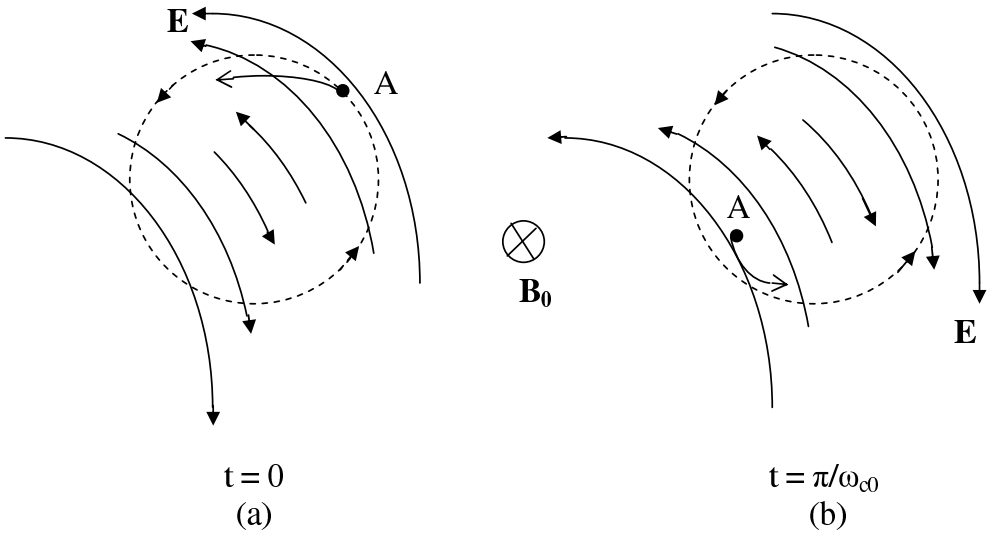

Figure 2.5: Gyration of test electron A, entering in the decelerating phase, over one period of the gyro-cycle for fundamental harmonic gyro-peniotron interaction

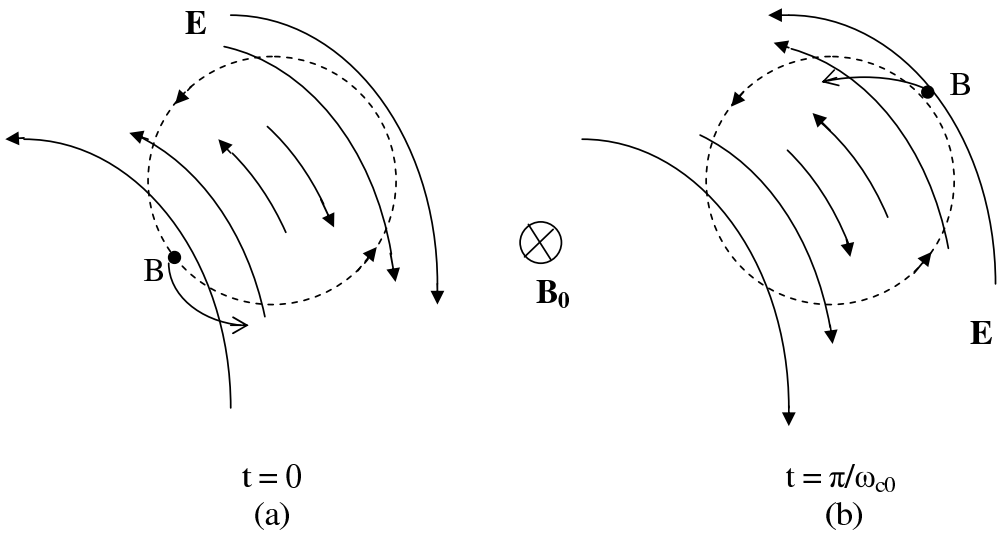

Figure 2.6: Gyration of test electron B, entering in the accelerating phase, over one period of the gyro-cycle for fundamental harmonic gyro-peniotron interaction

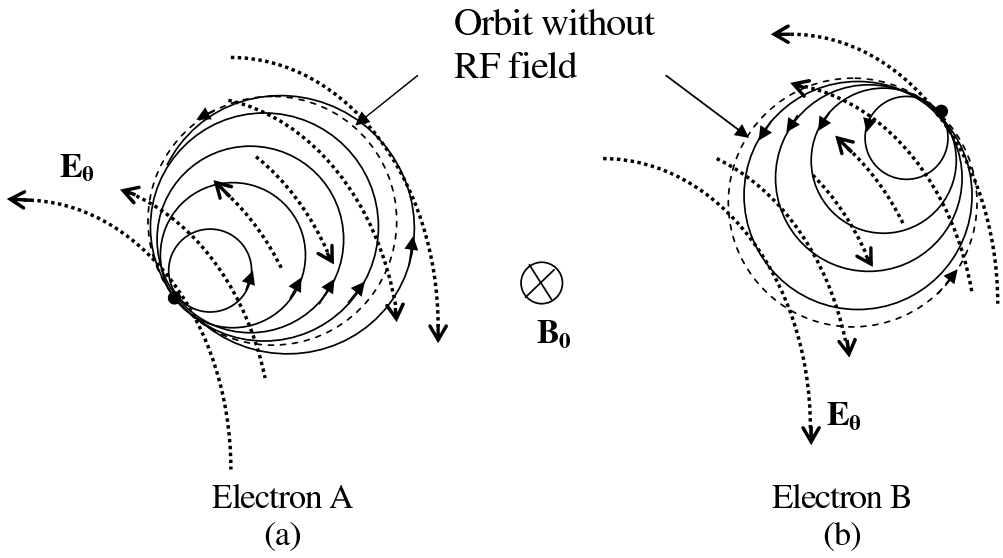

Figure 2.7: Gyro-peniotron interaction causing electron segregation accompanied by guiding center motion

phase of the RF electric field changes by 180^0. Electron A will find itself in an decelerating phase, but in a stronger electric field due to its larger Larmor radius as can be seen in Fig. 2.5b. In contrast, after a half gyro-cycle, electron B will find itself in an accelerating field, but in a weaker electric field due to its smaller Larmor radius as can be seen from Fig. 2.6b. Thus, both electrons A and B encounter stronger decelerating than accelerating electric fields in each gyro-cycle while their Larmor radius progressively reduces as shown in Fig. 2.7.

An important consequence of this interaction mechanism is that the guiding center of the electrons also moves away from its initial position after each gyro-cycle. As can be observed from Fig. 2.7, the electron guiding centers move in different directions which leads to electron segregation in contrast to electron bunching that happens in gyrotron interaction. Another important observation to be made is that though each electron is both decelerated as well as accelerated while interacting with the RF electric field, the amount of deceleration is greater than acceleration for all electrons. Thus, all electrons give up more energy than they take from the RF fields. This leads to a very high efficiency interaction as there are no "bad" electrons that, on an average, only absorb energy from the RF fields.

Chapter 3

Dispersion relation for a CRM

In this chapter we present a dispersion relation developed in [28] for a CRM amplifier with an annular electron beam in a cylindrical waveguide that includes the effects of both O-type and M-type interactions discussed earlier. In chapter 4 and chapter 5 we will develop a nonlinear theory and a linear theory from first principles for a CRM oscillator working close to cutoff. However, the purpose of studying the dispersion relation presented in this chapter is to identify different regimes of operation in a CRM depending on the electron beam position and other beam characteristics. This dispersion relation is completely general and includes both O-type and M-type interaction effects and is given by

$$\left(\frac{\omega^2}{c^2} - k_z^2 - k_\perp^2\right) = \hat{I}\left\{\frac{\beta_\perp^2\left(\omega^2 - k_z^2 c^2\right)}{\left(\Delta\omega_s\right)^2} O_s - \frac{\left(\omega - k_z v_{z_0}\right)}{\left(\Delta\omega_s\right)} M_s\right\}. \tag{3.1}$$

where ω is the angular frequency of operation, k_z and $k_\perp$ are the axial wavenumber and waveguide cutoff wavenumber respectively. The quantitiy c is the velocity of light in free space, $\beta = v_\perp/c$, and $v_\perp$ is the transverse velocity and v_{z_0} is the electron

axial velocity. The quantity $\hat{I}$ is a constant whose value depends on the electron beam current and geometry of the interaction waveguide. The term $\Delta\omega_s$ is the electron cyclotron detuning factor given by

$$\Delta\omega_s = \omega - k_z v_{z_0} - s\omega_{c_0}, \tag{3.2}$$

where s is the cyclotron harmonic resonance number and ω_{c_0} is the electron cyclotron frequency. Near resonance, $\Delta\omega_s \simeq 0$. The terms O_s and M_s are given by

$$O_s = \left[J_{m-s}(k_\perp R_c) J'_s(k_\perp r_L)\right]^2 \tag{3.3}$$

$$M_s = 2O_s - 2k_\perp r_L J^2_{m-s}(k_\perp R_c) J'_s(k_\perp r_L) J''_s(k_\perp r_L) - \frac{k_\perp^2 r_L^2}{2}\Psi. \tag{3.4}$$

The term Ψ in (3.4) is the factor that is responsible for peniotron interaction which is given by

$$\begin{aligned}\Psi \;=\; & -\frac{2k_\perp^2}{k_\perp r_L}\Bigg\{ \left[(m-s)J'_{s+1}(k_\perp r_L) + \frac{s+1}{k_\perp r_L}J_{s+1}(k_\perp r_L)\right] J_{m-(s+1)}(k_\perp R_c) \\ & - \left[(m-s)J'_{s-1}(k_\perp r_L) + \frac{s-1}{k_\perp r_L}J_{s-1}(k_\perp r_L)\right] J_{m-(s-1)}(k_\perp R_c) \\ & - \frac{1}{2}k_\perp r_L \left[J'_{s+2}(k_\perp r_L) J^2_{m-(s+2)}(k_\perp R_c) + J'_{s-2}(k_\perp r_L) J^2_{m-(s-2)}(k_\perp R_c)\right] \Bigg\}\end{aligned} \tag{3.5}$$

Here m is the azimuthal mode number, R_c is the electron guiding center radius and r_L is the electron Larmor radius.

The terms O_s and M_s in the (3.1) are factors that contribute to the O-type and M-type interaction respectively. In (3.1), we note that the term O_s is divided by $(\Delta\omega_s)^2$ while M_s is divided by $(\Delta\omega_s)$. Thus, when the O_s and M_s terms are of the same order, O-type interaction dominates as $\Delta\omega_s$ is small. This, in general, is the case for gyrotron operation when the term containing M_s in (3.1) may be neglected.

There are various ways in which M-type interaction effects may be made visible:

- by positioning the beam where the interacting EM mode has very small O-type interaction with the electron beam such that $J_{m-s}(k_\perp R_c)$ is very small. This may be achieved by placing the electron guiding center on the "null" of the EM field where the gyrotron coupling becomes zero.
- by operating far from waveguide cutoff when $k_z \simeq \omega/c$ and
- by reducing the transverse component of the velocity $\beta_{\perp 0}$ which leads to a reduced electron velocity pitch factor.

The M_s term contains factors that cause peniotron action associated with the transverse drift of electron guiding centers. Depending on how the O-type effects are suppressed, peniotron or auto-resonance or both effects become visible. When the operation is close to waveguide cutoff ($k_z \to 0$) and when $J_{m-s}(k_\perp R_c) \to 0$, peniotron action dominates. When operation is far from cutoff ($k_z \to \omega/c$), autoresonance effects become visible.

At this point we wish to make a few comments on the linear theory that has been published in the literature by various researchers to address the CRM interaction in the linear regime (for example, see [28, 38, 30, 9, 27, 21, 31, 32, 33]). In most of these works a linear equation similar to the dispersion relation (3.1) has been derived to account for all possible interaction mechanisms in a CRM. However, the emphasis in most papers is to study gyrotron interaction and very few papers address the peniotron interaction specifically [27, 33].

We have found that the dispersion relation presented in many papers does not contain the term Ψ shown in (3.5) [27, 30, 31]. In the absence of the term Ψ, we can see from (3.3) and (3.4) that both O_s and M_s terms in (3.1) will become zero when the electron beam is placed with its guiding center on the "null" of the operating mode when $J_{m-s}(k_\perp R_c) = 0$. Under these conditions the right hand side of (3.1) becomes zero and one can expect no excitation of the EM mode. This implies that a gyro-peniotron mode cannot be excited when the electron beam is placed where $J_{m-s}(k_\perp R_c) = 0$. Based on this implication, Vitello and Ko in their paper [27] suggest that in order to excite a gyro-peniotron mode the beam guiding center has to be positioned away from the null of the EM mode to be excited.

From (3.5) we see that the term Ψ will not become zero when $J_{m-s}(k_\perp R_c) = 0$. Thus, the dispersion equation (3.1) derived by Li *et al.*, [28], shows that gyro-peniotron mode can be excited *even* when the electron beam is placed where the electron guiding center coincides with the null of the EM mode to be excited. Thus, we see that there is a discrepancy in the literature about the possibility of exciting a gyro-peniotron mode when $J_{m-s}(k_\perp R_c) = 0$.

Döhler addresses this particular issue in [32, 33] where he shows that the term Ψ in (3.4) is due to a dipole current caused by the periodic radial deformations of the beamlets in the electron beam. He points out that when the aforementioned dipole current is neglected as done by Chu *et al.*, in [38], the term Ψ in (3.4) becomes zero. Then excitation of a gyro-peniotron mode when $J_{m-s}(k_\perp R_c) = 0$ cannot be expected.

Therefore, it seems that the dipole current caused by the periodic deformation

of the beamlets is not accounted for if the dispersion equation indicate that a gyro-peniotron interaction is not possible when $J_{m-s}(k_\perp R_c) = 0$. In deriving (3.1) Li *et al.*, [28], have accounted for the dipole current and we can see from (3.5) that $\Psi \neq 0$ when $J_{m-s}(k_\perp R_c) = 0$, leading to the possibility of excitation of a gyro-peniotron mode.

3.1 Regimes of operation of a gyro-device

The dispersion equation (3.1) is a fourth order equation in k_z, with four roots. Wave growth is possible when there exists a non-zero imaginary part for the roots of the dispersion equation. Four different regimes of operation can be recognized under which electron energy in a CRM device can be extracted for wave growth.

3.1.1 Gyrotron

When the device operates close to waveguide cutoff, $k_z \to 0$, the axial momentum is constant and the axial bunching is negligible. Also, if the electron guiding center is positioned for maximum interaction with the EM wave, for the given mode $J_{m-s}(k_\perp R_c)$ is at its peak, the term O_s will have a large value as can be seen from (3.3). When the device operates in this regime, O-type interaction dominates and it is known as the gyrotron regime. The electron interaction with the EM wave depends on the relative phase between the individual electron and the wave. As each electron is in relatively different phase with the wave, the changes in electron energy is different for each electron. Thus, their cyclotron frequencies differ and

electrons tend to bunch. When the cyclotron resonance mismatch between the EM wave and the electron cyclotron frequency is in a proper range ($\omega - k_z v_z > s\omega_{c_0}$), the bunched electrons are decelerated by the EM wave causing growth in the EM wave.

3.1.2 Peniotron

In a peniotron, as in a gyrotron, the device can operate close to cutoff. However, the electron guiding center is positioned where $J_{m-s}(k_\perp R_c) \to 0$, causing O_s term to become very small (see equation (3.3)), which suppresses O-type interaction. Under this condition, electrons interact with the EM wave due to the M-type interaction (the last term in RHS of (3.4)). This interaction causes the electrons to both accelerate and decelerate in each gyro cycle. The electrons, on average, give up more of their kinetic energy (decelerate) than absorb RF energy (accelerate) during every electron gyro-cycle accompanied by a drift in the guiding center. As all electrons interact in such a way as to, on an average over each gyro cycle, give up their orbital kinetic energy, the maximum orbital conversion efficiency of a peniotron can be much higher than in a gyrotron.

3.1.3 Cyclotron Auto-Resonant Maser (CARM)

When the electron guiding center is positioned for maximum interaction with a given mode, but operated far from cutoff, the device is said to operate in the Cyclotron Auto-Resonant Maser (CARM) regime. Though $J_{m-s}(k_\perp R_c)$ will be large

due to the electron beam position, due to operation far from cutoff when $k_z \rightarrow \omega/c$ the coefficient of O_s in (3.1) becomes small and O-type effects are suppressed making M-type effects visible. However, the effect on the electrons will be different from that of a peniotron. When $k_z \rightarrow \omega/c$, the RF magnetic field interaction with the electrons which is not visible in gyrotron and peniotron interactions becomes manifest. This interaction which causes axial bunching of the electrons is also known as the Weibel interaction. This bunching proceeds in such a way as to offset the orbital bunching visible in a gyrotron. Thus, in this regime, due to the partial cancellation of the orbital bunching by the axial bunching, O-type effects are partially suppressed. However, as both orbital and axial velocity components of the electrons are involved in the energy conversion process, there is a potential for large energy conversion efficiency in a CARM.

3.1.4 Auto-Resonant Peniotron (ARP)

When the electron beam is positioned for peniotron operation and the operation is far from cutoff, $J_{m-s}(k_\perp R_c) \rightarrow 0$ and $k_z \rightarrow \omega/c$. As can be seen from (3.1) and (3.3), the O-type interaction can be more effectively suppressed. When the device operates in this regime, it is called an auto-resonant peniotron. As in a peniotron, there is no phase bunching of electrons, which can lead to high orbital efficiency. In addition, due to the operation far from cutoff, the RF magnetic field will assist in harnessing the electron energy in the axial velocity component of the electrons. Thus a theoretical efficiency of 100% is possible in this regime which is

known as the Auto-Resonant Peniotron (ARP) regime.

As we have seen, each of the four regimes of operation, viz., gyrotron, peniotron, CARM and APR, is capable of converting electron energy into RF energy. However, each regime has its own advantages and disadvantages. While, gyrotrons have the least conversion efficiency possible of the four regimes, they can operate in very high order modes. So, the interaction cavity dimensions can be large making it possible to generate very high RF power in long pulse or CW operation. CARMs can operate at higher order modes and have a capacity for high conversion efficiency, but their operation is severely limited due to high sensitivity to electron velocity spread. APRs have a very attractive possibility of 100% conversion efficiency. However, the problem of mode competition and sensitivity to electron velocity spread limits its usefulness.

Peniotrons have proved to deliver power at high conversion efficiencies. In order to deliver high powers like in gyrotrons, they have to be configured as gyro-peniotrons in a smooth walled waveguide cavity [2]. But operation in high order modes is not possible for a gyro-peniotron due to mode competition from gyrotron modes. The power level at which a gyro-peniotron can work is limited as at low order modes the interaction waveguide's radius is small.

Chapter 4

Nonlinear equations governing electron beam-wave interaction

Generally, in a gyrotron interaction the electron "guiding centers" closely follow the magnetic field lines. For an annular beam, all electrons in each beamlet will gyrate about the same axis of rotation with very little change in the guiding center radius. To reduce computational complexity, a gyrotron analysis is usually carried out assuming that the guiding center radius remains constant throughout the interaction for all electrons in a beamlet, with very little error [9]. Also, for a gyrotron, the interaction between the beam and the RF wave closely satisfies the condition $\omega \cong s\omega_{c_0}$ for many cyclotron orbits, where s is the cyclotron harmonic number. The electrons have very little interaction with other harmonics and may be neglected. Thus, we can use simple gyro-averaged equations to solve the equations of motion in a gyrotron. This further saves computational time.

In contrast, in peniotron interactions the electrons in a beamlet do not follow a

constant guiding center like in a gyrotron. Therefore, we have to include the guiding center motion of the electrons also in the analysis of a peniotron. Also, peniotron interactions involve more than one harmonic interaction [39]. Hence, we cannot use gyro-averaged equations to solve the equations of motion as in the analysis of a gyrotron. The number of harmonics that need to be considered depends on the structure of the interaction region [39].

In this chapter we derive both the equations describing the gyro motion as well as the guiding center motion of the electrons as the electrons stream down along the axis of the interaction region while interacting with the RF wave. For completeness we have included the effects of the RF magnetic field on the electron motion in our derivation. However, when the device is operated close to the waveguide cutoff number, as in gyrotrons and peniotrons, the effects of RF magnetic field may be neglected. When the device operation is far from cutoff, as in Cyclotron Auto Resonant Masers (CARM) and Auto Resonant Peniotrons (ARP), the effect of RF magnetic field becomes very important. For successful operation far from cut-off, the electron beam should have very small velocity spread ($< 1\%$) which is generally very hard to achieve [21]. In this study we restrict ourselves to studying the device close to cut-off. Hence, in our analysis we neglect the effects of RF magnetic fields.

For high Q interaction cavities, it may be assumed that the electron transit time is very small compared to the rise time (Q/ω) of the RF amplitude. Based on this assumption we present a scheme to study the temporal evolution of EM modes, which follows from the method given in [9].

4.1 Guiding center formulation

For a mildly relativistic electron beam (such beams are generally used in gyrotrons), the equation describing electron motion may be written as (in Gaussian units),

$$\frac{d\mathbf{u}}{dt} + \frac{e}{m_0}\left(\frac{\mathbf{u}}{\gamma c} \times B_0\hat{z}\right) = \mathbf{a} \tag{4.1}$$

where

$$\mathbf{a} = -\frac{e}{\gamma m_0}\left(\mathbf{E_1} + \frac{\mathbf{u}}{c} \times \mathbf{B_1}\right)$$

Subscripts "0" and "1" denote DC and RF terms, respectively. e is the electron charge, m_0 is the electron rest mass, c is the velocity of light in free space, B_0 is the external magnetic field and γ is the relativistic mass factor. $\mathbf{u} = \gamma\mathbf{v}$, where $\mathbf{v}$ is the electron velocity. We will be assuming that the nature of the electron trajectories does not change substantially in the presence of RF fields from the unperturbed trajectories [39].

$\mathbf{r}$ and $\mathbf{u}$ can be written as a vector combination of "perpendicular" and "axial" components.

$$\mathbf{r} = \mathbf{r}_\perp + z\hat{\mathbf{z}}$$

$$\mathbf{u} = \mathbf{u}_\perp + u_z\hat{\mathbf{z}}$$

where $\mathbf{r}_\perp = x\hat{\mathbf{x}} + y\hat{\mathbf{y}}$ and $\mathbf{u}_\perp = u_x\hat{\mathbf{x}} + u_y\hat{\mathbf{y}}$. From Fig.4.1 we see that the transverse position vector may be written as a combination of the guiding center position (X, Y), Larmor radius r_L and gyro-phase θ.

$$\mathbf{r}_\perp = (X + r_L\cos\theta)\hat{\mathbf{x}} + (Y + r_L\sin\theta)\hat{\mathbf{y}}. \tag{4.2}$$

The amplitude of $\mathbf{u}_\perp$ may be written as

$$|\mathbf{u}_\perp| = u_t = r_L \Omega_0, \tag{4.3}$$

where $\Omega_0 = eB_0/m_0c$. (Note that $\omega_c = \Omega_0/\gamma$. For the present analysis it is convenient to show the relativistic factor γ explicitly in the denominator of the cyclotron frequency).

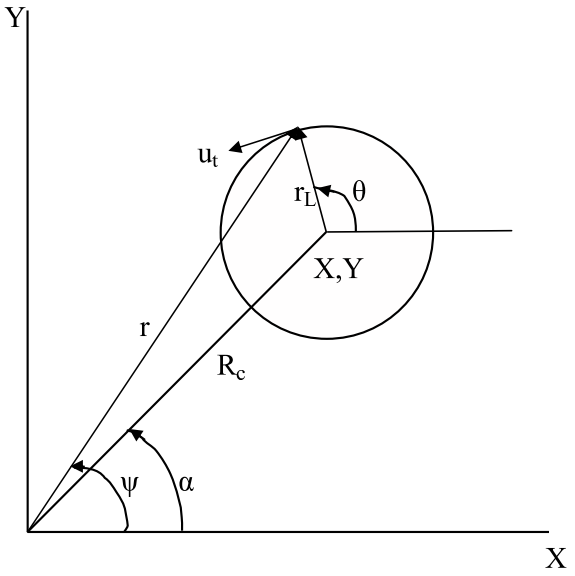

Figure 4.1: Projection of the electron orbit on the cross-sectional plane of the interaction region showing the guiding center ((X,Y) or (R_c, α)), electron position ((r, ψ) in waveguide frame and (r_L, θ) in guiding center frame) and transverse component of $\mathbf{u}$

From Fig. 4.1 we see that $u_x = -u_t \sin\theta$ and $u_y = u_t \cos\theta$. Then,

$$\mathbf{u}_\perp = -u_t \sin\theta \hat{\mathbf{x}} + u_t \cos\theta \hat{\mathbf{y}}. \tag{4.4}$$

In complex notation, we define

$$r_\perp = x + iy = X + iY + r_L e^{i\theta} \tag{4.5}$$

and

$$u_\perp = \gamma \frac{dr_\perp}{dt} = i u_t e^{i\theta} \tag{4.6}$$

From (4.3), (4.5) and (4.6),

$$\frac{dX}{dt} + i\frac{dY}{dt} = -\left[\frac{dr_L}{dt} + i r_L \left(\frac{d\theta}{dt} - \frac{\Omega_0}{\gamma}\right)\right] e^{i\theta}. \tag{4.7}$$

Separating real and imaginary parts in (4.7), we have

$$\begin{aligned} \frac{dX}{dt} &= -\frac{dr_L}{dt}\cos\theta + r_L\left(\frac{d\theta}{dt} - \frac{\Omega_0}{\gamma}\right)\sin\theta \\ \frac{dY}{dt} &= -\frac{dr_L}{dt}\sin\theta - r_L\left(\frac{d\theta}{dt} - \frac{\Omega_0}{\gamma}\right)\cos\theta \end{aligned} \tag{4.8}$$

The axial velocity of the electron is given by

$$\frac{dz}{dt} = \frac{u_z}{\gamma} \tag{4.9}$$

Separating the "perpendicular" and "axial" components of motion in (4.1), we have in complex notation

$$\frac{du_\perp}{dt} - i\frac{\Omega_0}{\gamma} u_\perp = a_x + i a_y \tag{4.10}$$

$$\frac{du_z}{dt} = a_z \tag{4.11}$$

Combining (4.3) and (4.10) and separating real and imaginary parts, we get

$$\frac{du_t}{dt} = a_y \cos\theta - a_x \sin\theta \tag{4.12}$$

$$\frac{d\theta}{dt} = \frac{\Omega_0}{\gamma} - \frac{1}{u_t}\left(a_x \cos\theta + a_y \sin\theta\right) \tag{4.13}$$

and

$$\frac{du_z}{dt} = a_z. \tag{4.14}$$

Equations (4.8), (4.9), (4.11), (4.12) and (4.13) form a complete set of equations for the electron motion with the appropriate RF acceleration components:

$$\begin{aligned} a_x &= -\frac{e}{m_0}\left[E_x + \frac{u_y B_z}{c\gamma} - \frac{u_z B_y}{c\gamma}\right] \\ a_y &= -\frac{e}{m_0}\left[E_y + \frac{u_x B_z}{c\gamma} - \frac{u_z B_x}{c\gamma}\right] \\ a_z &= -\frac{e}{m_0}\left[E_z + \frac{u_y B_x}{c\gamma} - \frac{u_x B_y}{c\gamma}\right]. \end{aligned} \tag{4.15}$$

For a cylindrical waveguide the RF fields may be considered as a sum of many cylindrical modes which are (we consider only TE modes with the axis of reference at the center of the waveguide)

$$\begin{aligned} E_r &= \sum_m i E_{0_m}\left(\frac{m J_m(k_{\perp_m} r)}{k_{\perp_m} r}\right) f_m(z) e^{i(\omega_m t - m\psi + \varphi_m)} \\ E_\psi &= \sum_m E_{0_m} f_m(z) J'_m(k_{\perp_m} r) e^{i(\omega_m t - m\psi + \varphi_m)} \\ E_z &= 0 \\ B_\psi &= -\sum_m \frac{E_{0_m} c}{\omega_m}\left(\frac{m J_m(k_{\perp_m} r)}{k_{\perp_m} r}\right) \frac{df_m(z)}{dz} e^{i(\omega_m t - m\psi + \varphi_m)} \\ B_r &= -\sum_m i \frac{E_{0_m} c}{\omega_m} \frac{df_m(z)}{dz} J'_m(k_{\perp_m} r) e^{i(\omega_m t - m\psi + \varphi_m)} \\ B_z &= -\sum_m i \frac{k_{\perp_m} E_{0_m} c}{\omega_m} J_m(k_{\perp_m} r) f_m(z) e^{i(\omega_m t - m\psi + \varphi_m)}, \end{aligned} \tag{4.16}$$

where $m, E_{0_m}, \omega_m, k_{\perp_m}, \varphi_m$ and $f_m(z)$ are the azimuthal mode number, field amplitude, angular frequency, cutoff wave number, phase and axial field profile for a given mode, respectively.

It is convenient to move the reference from the center of the cylindrical waveguide

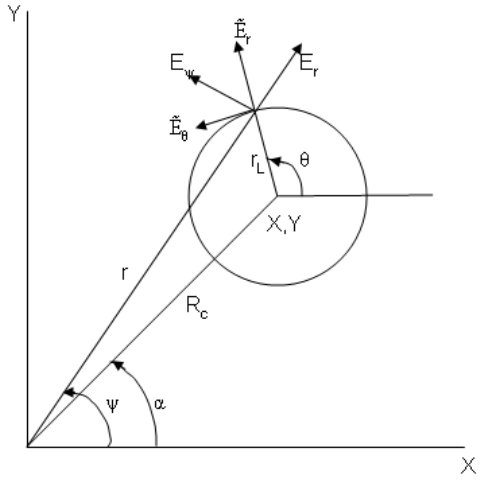

Figure 4.2: Projection of the electron orbit on the cross-sectional plane of the interaction region showing the guiding center ((X,Y) or (R_c, α)), electron position ((r, ψ) in waveguide frame and (r_L, θ) in guiding center frame), RF electric field in the waveguide frame (E_r, E_ψ) and guiding center frame $(\tilde{E}_r, \tilde{E}_\theta)$

to the electron guiding center, we use Graf's theorem (see for example [40])

$$
\begin{aligned}
\tilde{E}_r &= \sum_m \sum_{s=-\infty}^{\infty} iE_{0_m} f_m(z) J_{m-s}(k_{\perp_m} R_c) \left(\frac{sJ_s(k_{\perp_m} r_L)}{k_{\perp_m} r_L} \right) e^{i(\omega_m t - s(\theta-\alpha) - m\alpha + \varphi_m)} \\
\tilde{E}_\theta &= \sum_m \sum_{s=-\infty}^{\infty} E_{0_m} f_m(z) J_{m-s}(k_{\perp_m} R_c) J'_s(k_{\perp_m} r_L) e^{i(\omega_m t - s(\theta-\alpha) - m\alpha + \varphi_m)} \\
\tilde{E}_z &= 0 \qquad (4.17) \\
\tilde{B}_\theta &= -\sum_m \sum_{s=-\infty}^{\infty} \frac{E_{0_m} c}{\omega_m} J_{m-s}(k_{\perp_m} R_c) \left(\frac{sJ_s(k_{\perp_m} r_L)}{k_{\perp_m} r_L} \right) \frac{df_m(z)}{dz} e^{i(\omega_m t - s(\theta-\alpha) - m\alpha + \varphi_m)} \\
\tilde{B}_r &= -\sum_m \sum_{s=-\infty}^{\infty} i \frac{E_{0_m} c}{\omega_m} J_{m-s}(k_{\perp_m} R_c) \frac{df_m(z)}{dz} J'_s(k_{\perp_m} r_L) e^{i(\omega_m t - s(\theta-\alpha) - m\alpha + \varphi_m)} \\
\tilde{B}_z &= -\sum_m \sum_{s=-\infty}^{\infty} i \frac{k_{\perp_m} E_{0_m} c}{\omega_m} J_{m-s}(k_{\perp_m} R_c) J_s(k_{\perp_m} r_L) f_m(z) e^{i(\omega_m t - s(\theta-\alpha) - m\alpha + \varphi_m).}
\end{aligned}
$$

From Fig.4.2

$$
\begin{aligned}
A_x &= \tilde{A}_r \cos\theta - \tilde{A}_\theta \sin\theta \\
A_y &= \tilde{A}_\theta \cos\theta + \tilde{A}_r \sin\theta \qquad (4.18)
\end{aligned}
$$

where $\tilde{A}$ represents either **E** or **B** RF fields, in the reference frame of the guiding center.

Combining (4.12)-(4.14), (4.15) and (4.18), we get

$$\begin{aligned} \frac{du_t}{dt} &= -\frac{e}{m_0}\left(\tilde{E}_\theta + \frac{u_z \tilde{B}_r}{c\gamma}\right) \\ \frac{d\theta}{dt} &= \frac{\Omega_0}{\gamma} + \frac{e}{m_0 u_t}\left(\tilde{E}_r + \frac{u_t \tilde{B}_\theta}{c\gamma}\right) \\ \frac{du_z}{dt} &= \frac{e}{m_0}\frac{u_t \tilde{B}_r}{c\gamma} \end{aligned} \tag{4.19}$$

In the next section we will be considering the temporal evolution of EM modes. For cavities with a large Q-factor, the time evolution of the modes is much slower than the electron transit time through the cavity. In order to distinguish the two time scales, for convinience, we change the variable t in (4.8), (4.9) and(4.19) to the variable z by the following transformation.

$$\frac{d}{dt} = \frac{u_z}{\gamma}\frac{d}{dz}.$$

Using this transformation in (4.19), combining it with (4.17) and taking only the

real parts, we have

$$\frac{du_t}{dz} = -\frac{e}{m_0} Re\Bigg\{ \sum_m \sum_{s=-\infty}^{s=\infty} E_{0_m} J_{m-s}(k_{\perp_m} R_c)$$
$$J'_s(k_{\perp_m} r_L) \left[|f_m(z)| \left(\frac{\gamma}{u_z} - \frac{1}{\omega_m} \frac{d\zeta(z)}{dz} \right) - i \frac{u_z k_z}{\gamma \omega_m} - i \frac{k_z}{\omega_m} \frac{d|f_m(z)|}{dz} \right] e^{i\chi_m} \Bigg\}$$
$$\frac{d\theta}{dz} = \frac{\Omega_0}{u_z} + \frac{e}{u_t m_0}$$
$$Re\Bigg\{ \sum_m \sum_{s=-\infty}^{s=\infty} E_{0_m} J_{m-s}(k_{\perp_m} R_c) \Bigg(\frac{1}{\omega_m} \frac{s J_s(k_{\perp_m} r_L)}{k_{\perp_m} r_L} \frac{d|f_m(z)|}{dz}$$
$$+ i \left[\frac{\gamma}{u_z} \frac{s J_s(k_{\perp_m} r_L)}{k_{\perp_m} r_L} - \frac{u_t}{k_{\perp_m}} u_z \omega_m J_s(k_{\perp_m} r_L) \frac{1}{\omega_m} \frac{s J_s(k_{\perp_m} r_L)}{k_{\perp_m} r_L} \frac{d\zeta(z)}{dz} \right] |f_m(z)| \Bigg) e^{i\chi_m} \Bigg\}$$
$$\frac{du_z}{dz} = -\frac{e u_t k_z}{m_0 u_z \omega_m}$$
$$Re\Bigg\{ \sum_m \sum_{s=-\infty}^{s=\infty} i E_{0_m} J_{m-s}(k_{\perp_m} R_c) J'_s(k_{\perp_m} r_L) \left(\frac{d|f_m(z)|}{dz} - i|f_m(z)| \frac{d\zeta}{dz} \right) e^{i\chi_m} \Bigg\} \quad (4.20)$$

where $\chi_m = \omega_m t - s(\theta - \alpha) - m\alpha + \varphi_m - \zeta_m$ and we have assumed a field profile $f_m(z)$ of the form

$$f_m(z) = |f_m(z)| e^{-i\zeta_m(z)}$$

Transforming the equations governing the guiding center motion, (4.8), we get,

$$\begin{aligned} \frac{dX}{dz} &= -\frac{dr_L}{dz} \cos\theta + r_L \left(\frac{d\theta}{dz} - \frac{\Omega_0}{u_z} \right) \sin\theta \\ \frac{dY}{dz} &= -\frac{dr_L}{dz} \sin\theta - r_L \left(\frac{d\theta}{dz} - \frac{\Omega_0}{u_z} \right) \cos\theta \\ \frac{dt}{dz} &= \frac{\gamma}{u_z}. \end{aligned} \quad (4.21)$$

(4.20) and (4.21) form a set of equations describing electron motion inside a cylindrical cavity in the presence of interacting RF fields. It will be useful to remember that equations (4.20) and (4.21) are coupled through θ as well as because $du_t/dz = \Omega_0 dr_L/dz$.

The axial field profile $f_m(z)$ depends on the interaction cavity structure and

also the interaction process between the electrons and the wave. Therefore, for a self-consistent analysis of the electron interaction with the EM wave, a wave equation in $f_m(z)$ has to be solved with (4.20) and (4.21) along with the boundary conditions at the input and output ends of the interaction region. A search procedure is required to find $f_m(z)$ such that the boundary conditions are satisfied.

For multi-mode analysis, the procedure to find the axial field profile for all the modes self consistently as described above becomes computationally highly intensive not only because of the difficulty in matching the number of boundary conditions but also because the total number of electrons to be considered for multimode simulation is quite large (for example see Chapter 4 in [41]). There are self-consistent efficient codes like MAGY that can handle multimode analysis for gyrotrons. However, at the present writing MAGY does not have the capability to study gyro-peniotron effects.

To circumvent this problem, we make a simplifying assumption. We assume that the axial field profile $f_m(z)$ is fixed and does not change due to the interaction between the electrons and the wave. Such an assumption is valid when the diffraction Q-factor is large. Indeed, modern gyrotrons usually have a large diffraction Q. The diffraction Q becomes large when there are large reflections of the EM modes from both ends of the interaction cavity. When the diffraction Q is large the axial structure is fixed and is not changed significantly by the electron beam. In the case of high Q cavities, the axial field profile does not change significantly from the "cold" cavity field profile (i.e., field profile when there is no beam) [9]. A cold cavity field profile is in many cases close to a Gaussian corresponding to a cavity length [35].

We shall therefore use a Gaussian as the fixed axial field profile in all our studies of the gyro-peniotron.

4.2 Multi-mode analysis

The complex amplitude of any RF mode $E_m(t)$ inside the interaction cavity is a function of time due to the interaction of the modes with the electron beam. Though the amplitudes of electric and magnetic fields are usually assumed to be the same, strictly speaking, they are different. The electric and magnetic fields inside a resonator cavity when all the modes present are taken into account is of the form:

$$\mathbf{E} = \sum_m Re\left\{C_m \mathbf{E_m}(\mathbf{r}) e^{i\omega_m t}\right\},\ \mathbf{B} = \sum_m Re\left\{D_m \mathbf{B_m}(\mathbf{r}) e^{i\omega_m t}\right\} \tag{4.22}$$

Using (4.22) in Maxwell's equations

$$\begin{aligned} \nabla \times \mathbf{B} &= \frac{1}{c}\sum_m Re\left\{\left[\frac{dC_m}{dt_s} + i\omega_m C_m\right]\mathbf{E_m} e^{i\omega_m t} + 4\pi \mathbf{j}_{\omega_\mathbf{m}}\right\} \\ \nabla \times \mathbf{E} &= -\frac{1}{c}\sum_m Re\left\{\left[\frac{dD_m}{dt_s} + i\omega_m D_m\right]\mathbf{B_m} e^{i\omega_m t}\right\}, \end{aligned} \tag{4.23}$$

where ω_m is the angular frequency of the mode in the presence of the electron beam. t_s represents the time in "slow" time scale while t (without subscript) represents time in the "fast" time scale. For a "cold" (no beam present) open resonator

$$\nabla \times \mathbf{B_m} = i\frac{\omega_{m_0}}{c}\mathbf{E_m},\quad \nabla \times \mathbf{E_m} = -i\frac{\omega_{m_0}}{c}\mathbf{B_m}. \tag{4.24}$$

Here ω_{m_0} is the cold cavity eigenfrequency for the resonator. Taking the curl of (4.22) while using (4.24) and equating it to (4.23), we get

$$iD_m\omega_{m_0}\mathbf{E_m} = \left(\frac{dC_m}{dt_s} + i\omega_m C_m\right)\mathbf{E_m} + 4\pi\mathbf{j}_{\omega_\mathbf{m}} \tag{4.25}$$

$$C_m = \frac{1}{\omega_{m_0}} \left\{ \omega_m D_m - i \frac{dD_m}{dt_s} \right\} \tag{4.26}$$

Putting (4.26) in (4.25)

$$iD_m \omega_{m_0} \mathbf{E_m} = \left[\frac{1}{\omega_{m_0}} \left(\omega_m \frac{dD_m}{dt_s} - i \frac{d^2 D_m}{dt_s^2} \right) + i \frac{\omega_m}{\omega_{m_0}} \left(\omega_m D_m - i \frac{dD_m}{dt} \right) \right] \mathbf{E_m} + 4\pi \mathbf{j}_{\omega_\mathbf{m}} \tag{4.27}$$

Considering the fact that $\omega_m D_m >> |dD_m/dt|$, $\omega_m dD_m/dt_s >> |d^2 D_m/dt_s^2|$, we get

$$\left[\frac{dD_m}{dt_s} + i(\omega_m - \omega_{m_0}) D_m \right] \mathbf{E_m} = -4\pi \mathbf{j}_{\omega_\mathbf{m}}. \tag{4.28}$$

We have assumed that the mode frequency ω_m does not vary much from the cold cavity frequency ω_{m_0}. So, in getting (4.28) we have assumed $\omega_m/\omega_{m_0} \simeq 1$. Multiplying both sides by $\mathbf{E_m^*}$ and integrating over the resonator volume and introducing the norm of the operating mode

$$N_m = \frac{1}{8\pi} \int_V |\mathbf{E_m}|^2 dV = \frac{1}{8\pi} \int_V |\mathbf{B_m}|^2 dV$$

for orthogonal modes we have,

$$\frac{dD_m}{dt_s} + i(\omega_m - \omega_{m_0}) D_m = -\frac{1}{2N_m} \int_V \mathbf{j}_{\omega_\mathbf{m}} \cdot \mathbf{E_m^*} dV \tag{4.29}$$

As we are considering only TE modes, the integral in (4.29) becomes:

$$\int_V \mathbf{j}_{\omega_\mathbf{m}} \cdot \mathbf{E_m^*} dV = \int_V j_{\omega_{m_\perp}} E_m^* dV \tag{4.30}$$

where

$$j_{\omega_{m_\perp}} = \frac{1}{2\pi} \int_0^{2\pi} j_\perp(\mathbf{r}, t) e^{-i\omega_m t} d(\omega_m t)$$

and

$$\mathbf{j}_\perp = -\frac{I_0}{u_{z_0}} \mathbf{u}_\perp(\mathbf{r}, t)$$

The electric field along the perpendicular motion of the electron is

$$E_m^* = f_m^*(z) \sum_{s=-\infty}^{s=\infty} J_s'(k_{\perp_m} r_L) J_{m-s}(k_{\perp_m} R_c) e^{-i[(s-m)\alpha - s\theta]} \tag{4.31}$$

Equation (4.30) can be written as

$$\begin{aligned} \int_V \mathbf{j}_{\omega_\mathbf{m}} \cdot \mathbf{E}_\mathbf{m}^* dV = \frac{1}{(2\pi)^3} \int_0^{2\pi} d(\omega_m t_s) j_\perp(\mathbf{r}, t) e^{-i\omega_m t} \\ \times \int_0^{2\pi} d\theta \int_0^{2\pi} d\alpha \int_{-L/2}^{L/2} dz |E_m| e^{i[s(\theta-\alpha)+m\alpha-\varphi_m]}. \end{aligned} \tag{4.32}$$

As the electrons are discretely distributed, we write the integral in (4.32) as a summation over $\omega_m t$, θ and α to account for the distribution of electrons in time and space.

$$\int_V \mathbf{j}_{\omega_\mathbf{m}} \cdot \mathbf{E}_\mathbf{m}^* dV = \frac{1}{N_{\theta_p} N_{t_q} N_{\alpha_r}} \sum_{p,q,r} \int_{-L/2}^{L/2} dz \frac{I_0}{u_{z_0}} u_\perp |E_m| e^{i[s(\theta_p - \alpha_r) + m\alpha_r - \omega t_q - \varphi_m]}, \tag{4.33}$$

where N_{θ_p}, N_{t_q}, and N_{α_r} are the number of electrons distributed about the gyro angle, time and azimuth, respectively. p, q and r subscripts represent the corresponding electrons. For cylindrical cavities, the norm N_m is

$$N_m = \frac{c^2}{4\omega_m^2} (\nu_{m,p}^2 - m^2) J_m^2(\nu_{m,p}) \int_{-L/2}^{L/2} |f_m(z)|^2 dz \tag{4.34}$$

The complex frequency for the m^{th} mode inside the cavity may be written as

$$\omega_{m_0} = \omega_{m_0}' + i \frac{\omega_{m_0}'}{2Q_m}$$

where Q_m is the Q-factor for the m^{th} mode. For a high Q cavity we can, to a good approximation, assume that the real part of the cold cavity frequency ω_{m_0}' is equal to ω_m. Putting (4.33) and (4.34) in (4.29) and taking the amplitude of the electric

field for the m^{th} mode as $E_{0_m} = D_m$, we have

$$\frac{dE_{0_m}}{dt_s} = -\frac{\omega_m}{2Q_m}E_{0_m} + \frac{2\omega_m^2 I_0}{N_{\theta_p}N_{t_q}N_{\alpha_r}u_{z_0}c^2(\nu_{m,p}^2 - m^2)J_m^2(\nu_{m,p})\int_{-L/2}^{L/2}|f_m(z)|^2dz}$$
$$\cdot\sum_{p,q,r}\int_{-L/2}^{L/2}u_\perp f_m^*(z)\sum_{s=-\infty}^{s=\infty}J_{m-s}(k_\perp R_c)J_s'(k_{\perp_m}r_L)e^{i[s(\theta_p-\alpha_r)+m\alpha_r-\omega t_q-\varphi_m]} \tag{4.35}$$

4.3 Method of solution

In this work we are interested only in the operation of a gyrotron and a gyro-peniotron. As the RF magnetic fields have negligible effect on the working of a CRM in these regimes of operation, we will neglect their effects. In this section we rewrite (4.20) in a normalized form where we neglect RF magnetic fields. All our calculations in the next chapter will be based on the equations presented in this section.

We make the following normalizations:

$$\overline{r}_L = \frac{r_L}{a},\ \overline{R}_c = \frac{R_c}{a},\ \overline{X} = \frac{X}{a},\ \overline{Y} = \frac{Y}{a},\ \overline{z} = \frac{z}{a},\ \overline{u} = \frac{u}{c}$$

$$\overline{k} = ka,\ \overline{t} = t\omega,\ \overline{\omega} = \frac{a\omega}{c},\ \ \overline{E}_0 = \frac{ea}{m_0c^2}E_0,\ \overline{I}_0 = \frac{2e}{m_0c^3}I_0$$

Using the above normalizations in (4.20), (4.21) and (4.35) and neglecting the effect of RF magnetic fields, we get the following set of equations that may be used for multimode studies of gyrotrons or gyro-peniotrons.

$$
\begin{aligned}
\frac{d\overline{u}_t}{d\overline{z}} &= -\frac{\gamma}{\overline{u}_z} Re\Big\{ \sum_m \sum_{s=-\infty}^{s=\infty} \overline{E}_{0_m} J_{m-s}(\overline{k}_\perp \overline{R}_c) J_s'(\overline{k}_\perp \overline{r}_L) |f(\overline{z})| e^{i\chi_m} \Big\} \\
\frac{d\theta}{d\overline{z}} &= \frac{\overline{\Omega}_0}{\overline{u}_z} - \frac{\gamma}{\overline{u}_z \overline{u}_t} Re\Big\{ \sum_m \sum_{s=-\infty}^{s=\infty} i\overline{E}_{0_m} J_{m-s}(\overline{k}_\perp \overline{R}_c) \frac{s J_s(\overline{k}_\perp \overline{r}_L)}{\overline{k}_\perp \overline{r}_L} |f(\overline{z})| e^{i\chi_m} \Big\} \\
\frac{d\overline{u}_z}{d\overline{z}} &= 0
\end{aligned} \tag{4.36}
$$

$$
\begin{aligned}
\frac{d\overline{X}}{d\overline{z}} &= -\frac{1}{\overline{\Omega}_0} \left[\frac{d\overline{u}_t}{d\overline{z}} \cos\theta - \overline{u}_t \left(\frac{d\theta}{d\overline{z}} - \frac{\overline{\Omega}_0}{\overline{u}_z} \right) \sin\theta \right] \\
\frac{d\overline{Y}}{d\overline{z}} &= -\frac{1}{\overline{\Omega}_0} \left[\frac{d\overline{u}_t}{d\overline{z}} \sin\theta + \overline{u}_t \left(\frac{d\theta}{d\overline{z}} - \frac{\overline{\Omega}_0}{\overline{u}_z} \right) \cos\theta \right] \\
\frac{d\overline{t}}{d\overline{z}} &= \frac{\gamma\overline{\omega}}{\overline{u}_z},
\end{aligned} \tag{4.37}
$$

where $\chi_m = \overline{t} - s(\theta - \alpha) - m\alpha_r + \varphi_m - \zeta_m$. In writing (4.37) we have replaced r_L with u_t/ω_0. (4.36) and (4.37) are true for any electron. The solution for each electron in the fast time scale for the equations (4.36) and (4.37) are used in the slow time scale equation given below. The electrons are assumed to be uniformly distributed in $\overline{t}$, θ and α before they enter the interaction region.

Rewriting (4.35) using the normalized quantities, we get

$$
\begin{aligned}
\frac{d\overline{E}_{0_m}}{d\overline{t}_s} = &-\frac{\overline{E}_{0_m}}{2Q_m} + \frac{\overline{\omega}_m \overline{I}_0}{N_{\theta_p} N_{t_q} N_{\alpha_r} \overline{u}_{z_0} (\nu_{m,p}^2 - m^2) J_m^2(\nu_{m,p}) \int_{-\overline{L}/2}^{\overline{L}/2} |f_m(\overline{z})|^2 d\overline{z}} \\
&\cdot \sum_{p,q,r} \int_{-\overline{L}/2}^{\overline{L}/2} \overline{u}_\perp f_m^*(\overline{z}) \sum_{s=-\infty}^{s=\infty} J_{m-s}(\overline{k}_\perp \overline{R}_c) J_s'(\overline{k}_{\perp_m} \overline{r}_L) e^{i[s(\theta_p - \alpha_r) + m\alpha_r - \overline{t}_q - \varphi_m]} d\overline{z}
\end{aligned} \tag{4.38}
$$

Equations (4.36) and (4.37) form a set of ordinary differential equations which have to be solved simultaneously. It is assumed that the electrons propagate through

the interaction cavity much faster than the cavity fill time. So, in this time scale, it is assumed that the amplitude of the RF fields do not change as each set of electrons traverse through out the interaction region. Therefore, the solution of (4.36) and (4.37) can be used in (4.38) to estimate the change in the amplitude of the RF electric field for a given mode for each increment in time step in the slower time scale ($\overline{t}_s$).

Chapter 5

Linearization of equations governing electron beam-wave interaction

In the previous chapter we derived a set of non-linear differential equations describing the electron motion inside an EM field cavity assuming a fixed axial field profile for the EM field. We have also derived an equation to calculate the time evolution of a given mode (equation (4.38)). In this chapter we will linearize the set of equations (4.36) - (4.38) to study the starting conditions for a given mode for different beam parameters. The linearization process assumes that there is no interaction between orthogonal EM modes in the linear regime.

5.1 Basic equations

For convenience we rewrite (4.36) - (4.38) for a single mode in the following form:

$$\begin{aligned}
\frac{d\overline{u}_t}{d\overline{z}} &= -\overline{F}_1 Re\Big\{ \sum_{s'} J_u^{(s')} f(\overline{z}) e^{i\chi_{s'}} \Big\} \\
\frac{d\theta}{d\overline{z}} &= \frac{\overline{\Omega}_0}{\overline{u}_{z_0}} - \frac{\overline{F}_1}{u_{t_0}} Re\Big\{ \sum_{s'} i J_\theta^{(s')} f(\overline{z}) e^{i\chi_{s'}} \Big\} \\
\frac{d\overline{u}_{z_0}}{d\overline{z}} &= 0
\end{aligned} \tag{5.1}$$

$$\begin{aligned}
\frac{d\overline{X}}{d\overline{z}} &= -\frac{\overline{F}_1}{\overline{\Omega}_0} Re\Big\{ \sum_{s'} f(\overline{z}) \Big[J_u^{(s')} \cos\theta + i J_\theta^{(s')} \sin\theta \Big] e^{i\chi_{s'}} \Big\} \\
\frac{d\overline{Y}}{d\overline{z}} &= -\frac{\overline{F}_1}{\overline{\Omega}_0} Re\Big\{ \sum_{s'} f(\overline{z}) \Big[J_u^{(s')} \sin\theta - i J_\theta^{(s')} \cos\theta \Big] e^{i\chi_{s'}} \Big\} \\
\frac{d\overline{t}}{d\overline{z}} &= \frac{\gamma\overline{\omega}}{\overline{u}_{z_0}}
\end{aligned} \tag{5.2}$$

$$\frac{d\overline{F}_1}{d\overline{t}_s} = -\frac{\overline{F}_1}{2Q} + \hat{I}S, \tag{5.3}$$

where

$$\overline{F}_1 = \frac{\gamma_0 \overline{E}_0}{\overline{u}_{z_0}} \tag{5.4}$$

$$\hat{I} = \frac{\gamma_0 \overline{\omega} \overline{I}_0}{\overline{u}_{z_0}^2 (\nu^2 - m^2) J_m^2(\nu_{m,p}) \int_{-\overline{L}/2}^{\overline{L}/2} |f(\overline{z})|^2 d\overline{z}} \tag{5.5}$$

$$S = \frac{1}{N_{\theta_p} N_{t_q}} \sum_{p,q} \int_{-\overline{L}/2}^{\overline{L}/2} \overline{u}_t f^*(\overline{z}) \sum_{s''} J_u^{(s'')} e^{-i\chi_{s''}} dz. \tag{5.6}$$

N_{θ_p}, N_{t_q} are the total number of electrons initially uniformly distributed in θ and $\overline{t}$, respectively.

$$\begin{aligned}\chi_{s'} &= -\frac{\gamma_0\overline{\omega}}{\overline{u}_{z_0}}\overline{z} - s'(\theta+\theta_{p_0}) + (s'-m)\alpha + \overline{t}_{q_0} \\ \chi_{s''} &= -\frac{\gamma_0\overline{\omega}}{\overline{u}_{z_0}}\overline{z} - s''(\theta+\theta_{p_0}) + (s''-m)\alpha + \overline{t}_{q_0}. \end{aligned} \tag{5.7}$$

We have assumed that the initial phase of the RF field is arbitrarily zero, θ_{p_0} and $\overline{t}_{q_0}$ represent the initial phase of the pth and qth electrons distributed in θ and $\overline{t}$, respectively.

$$J_u^{(s')} = J_{m-s'}(\overline{k}_\perp \overline{R}_c) J'_{s'}(\overline{k}_\perp \overline{r}_L) \tag{5.8}$$

$$J_\theta^{(s')} = J_{m-s'}(\overline{k}_\perp \overline{R}_c) \frac{s' J_{s'}(\overline{k}_\perp \overline{r}_L)}{\overline{k}_\perp \overline{r}_L} \tag{5.9}$$

$$\overline{F}_1 = \frac{\gamma_0 \overline{E}_0}{\overline{u}_{z_0}} \tag{5.10}$$

s' and s'' represent the cyclotron harmonics considered in the "fast" and "slow" time scales, respectively.

5.2 Linearization

In the linear regime we can represent the position, phase and momentum of the electrons as a sum of unperturbed and perturbed quantities. The perturbation is due to the fields of the EM mode under consideration. We will distinguish the unperturbed and perturbed quantities with a "0" and "1" in the subscript. Thus, we write the normalized momentum, phase and normalized guiding center position

of the electron as follows:

$$\overline{u}_t = \overline{u}_{t_0} + \overline{u}_{t_1}, \theta = \theta_0 + \frac{\overline{\Omega}_{p_0}}{\overline{u}_{z_0}}\overline{z} + \theta_1, \overline{X} = \overline{X}_0 + \overline{X}_1, \overline{R}_{c_1} = \frac{\overline{X}_0\overline{X}_1 + \overline{Y}_0\overline{Y}_1}{\overline{R}_{c_0}} = \overline{X}_1\cos\alpha_0 + \overline{Y}_1\sin\alpha_0,$$

$$\alpha = \tan^{-1}\left[\frac{\overline{Y}_0}{\overline{X}_0} + \frac{\overline{Y}_1}{\overline{X}_0} - \frac{\overline{Y}_0\overline{X}_1}{\overline{X}_0^2}\right]. \tag{5.11}$$

In a cylindrical cavity structure that we are considering, due to cylindrical symmetry every beamlet in the annular electron beam experiences the same perturbation. Therefore, we can consider only one beamlet for our analysis. Without loss of generality, we will assume that the initial guiding center of the beamlet lies on the X-axis. So, $\overline{Y}_0 = 0$ and

$$\overline{R}_{c_1} = \overline{X}_1,\ \alpha_1 = \tan^{-1}\frac{\overline{Y}_1}{\overline{X}_0} \simeq \frac{\overline{Y}_1}{\overline{X}_0}. \tag{5.12}$$

Using (5.11) and (5.12) we can write $J_u^{(s'')}$ and $\chi_{s''}$ by Taylor expansion as

$$J_u^{(s'')} = J_{m-s''}(\overline{k}_\perp\overline{R}_{c_0})\left\{J'_{s''}(\overline{k}_\perp\overline{r}_{L_0}) + \frac{\overline{k}_\perp\overline{u}_{t_1}}{\overline{\Omega}_0}J''_{s''}(\overline{k}_\perp\overline{r}_{L_0})\right\}$$
$$+\overline{k}_\perp\overline{R}_{c_1}J'_{m-s''}(\overline{k}_\perp\overline{R}_{c_0})J_{s''}(\overline{k}_\perp\overline{r}_{L_0}) \tag{5.13}$$

$$\chi_{s''} = \chi_{s''_0} + \chi_{s''_1} \tag{5.14}$$

where

$$\chi_{s''_0} = \Delta\overline{\omega}_{s''}\overline{z} - s''\theta_{p_0} + \overline{t}_{q_0} + \zeta,\ \chi_{s''_1} = \frac{\gamma_1\overline{\omega}}{\overline{u}_{z_0}}\overline{z} - s''\theta_1 + (s''-m)\alpha_1$$

$$\Delta\overline{\omega}_s = \frac{\gamma_0\overline{\omega}}{\overline{u}_{z_0}} - s\frac{\overline{\Omega}_0}{\overline{u}_{z_0}}.$$

As $\chi_{s''_1}$ is small we can write

$$e^{i\chi_{s''}} \simeq e^{i\chi_{s''_0}}\{1 + i\chi_{s''_1}\} \tag{5.15}$$

The relativistic factor γ can be expressed as

$$\gamma = \gamma_0 + \gamma_1 = \gamma_0 + \frac{\overline{u}_{t_0}}{\gamma_0}\overline{u}_{t_1}. \tag{5.16}$$

The change in gyro angle θ with the axial coordinate can be written as the sum of unperturbed and perturbed parts as

$$\frac{d\theta}{d\overline{z}} = \frac{d\theta_0}{d\overline{z}} + \frac{d\theta_1}{d\overline{z}}$$

where the unperturbed part is given by

$$\frac{d\theta_0}{d\overline{z}} = \frac{\overline{\Omega}_0}{\overline{u}_{z_0}}$$

and so the perturbed part is then given by (from (5.1))

$$\frac{d\theta_1}{d\overline{z}} = -\frac{\overline{F}_1}{\overline{u}_{t_0}} Re\Big\{ \sum_{s'} i J_\theta^{(s')} f(\overline{z}) e^{i\chi_{s'}} \Big\}. \tag{5.17}$$

The axial field profile $f(\overline{z})$ can be written as a Fourier integral:

$$f(\overline{z}) = \int_{-\infty}^{\infty} \frac{dk}{2\pi} \overline{f}(k) e^{ik\overline{z}}. \tag{5.18}$$

Using (5.16), (5.17) and (5.18) in (5.1) and (5.2) and integrating with respect to $\overline{z}$, we get

$$\overline{u}_{t_1} = -\overline{F}_1 \sum_{s'} J_u^{(s')} Re\Big\{ \int_{-\infty}^{\infty} \frac{dk\overline{f}(k)}{2\pi i} \frac{e^{i(k\overline{z}+\chi_{s'})}}{k + \Delta\overline{\omega}_{s'}} \Big\} \tag{5.19}$$

$$\theta_1 = -\frac{\overline{F}_1}{\overline{u}_{t_0}} \sum_{s'} J_\theta^{(s')} Re\Big\{ \int_{-\infty}^{\infty} \frac{dk\overline{f}(k)}{2\pi} \frac{e^{i(k\overline{z}+\chi_{s'})}}{k + \Delta\overline{\omega}_{s'}} \Big\} \tag{5.20}$$

$$\overline{X}_1 = \frac{\overline{F}_1}{2\overline{\Omega}_0} \sum_{s'} Re\Big\{ \int_{-\infty}^{\infty} \frac{dk\overline{f}(k)}{2\pi i} e^{i(k\overline{z}+\chi_{s'})} \left[\frac{(J_u^{(s')} + J_\theta^{(s')}) e^{-i\frac{\overline{\Omega}_0}{\overline{u}_{z_0}}\overline{z}}}{k + \Delta\overline{\omega}_{s'-1}} + \frac{(J_u^{(s')} - J_\theta^{(s')}) e^{i\frac{\overline{\Omega}_0}{\overline{u}_{z_0}}\overline{z}}}{k + \Delta\overline{\omega}_{s'+1}} \right] \Big\} \tag{5.21}$$

$$\overline{Y}_1 = \frac{\overline{F}_1}{2\overline{\Omega}_0}\sum_{s'} Re\Bigg\{\int_{-\infty}^{\infty}\frac{dk\overline{f}(k)}{2\pi}e^{i(k\overline{z}+\chi_{s'})} \left[\frac{(J_u^{(s')}+J_\theta^{(s')})e^{-i\frac{\overline{\Omega}_0}{\overline{u}_{z_0}}\overline{z}}}{k+\Delta\overline{\omega}_{s'-1}} - \frac{(J_u^{(s')}-J_\theta^{(s')})e^{i\frac{\overline{\Omega}_0}{\overline{u}_{z_0}}\overline{z}}}{k+\Delta\overline{\omega}_{s'+1}}\right]\Bigg\} \tag{5.22}$$

$$\overline{t}_1 = -\frac{\overline{F}_1\overline{\omega u}_{t_0}}{\gamma_0\overline{u}_{z_0}}\sum_{s'} J_u^{(s')} Re\Bigg\{\int_{-\infty}^{\infty}\frac{dk\overline{f}(k)}{2\pi}\frac{e^{i(k\overline{z}+\chi_{s'})}}{(k+\Delta\overline{\omega}_{s'})^2}\Bigg\} \tag{5.23}$$

In (5.21) and (5.22) we have used the identity

$$e^{iA}\cos B = \frac{1}{2}\left\{e^{i(A-B)}+e^{i(A+B)}\right\},\ e^{iA}\sin B = \frac{i}{2}\left\{e^{i(A-B)}-e^{i(A+B)}\right\} \tag{5.24}$$

5.3 Evaluation of the source terms

The source term S given in (5.6) can be written as

$$S = S_{gyro} + S_{penio} \tag{5.25}$$

where

$$S_{gyro} = \frac{1}{N_{\theta_p}N_{t_q}}\sum_{p,q}\int_{-\overline{L}/2}^{\overline{L}/2} d\overline{z}f^*(\overline{z})\sum_{s''}\left\{\overline{u}_{t_1}J_{S_u}^{(s'')} + i\overline{u}_{t_0}\left(\overline{t}_1 - s''\theta_1\right)J_u^{(s'')}\right\}e^{-i\chi_{s''}} \tag{5.26}$$

$$S_{penio} = \frac{\overline{u}_{t_0}\overline{k}_\perp}{N_{\theta_p}N_{t_q}}\sum_{p,q}\int_{-\overline{L}/2}^{\overline{L}/2} d\overline{z}f^*(\overline{z})\sum_{s''}\left\{\overline{X}_1 J_{S_R}^{(s'')} + i\overline{Y}_1 J_{S_\alpha}^{(s'')}\right\}e^{-i\chi_{s''}}. \tag{5.27}$$

S_{gyro} and S_{penio} represent the source terms that contribute to the O-type (gyrotron) and M-type (peniotron) interactions respectively. The terms $J_{S_u}^{(s'')}$, $J_{S_R}^{(s'')}$ and $J_{S_\alpha}^{(s'')}$ are given by

$$J_{S_u}^{(s'')} = J_{m-s''}\left(\overline{k}_\perp\overline{R}_{c_0}\right)\left\{J'_{m-s''}\left(\overline{k}_\perp\overline{r}_{L_0}\right) + \frac{\overline{k}_\perp\overline{u}_{t_0}}{\overline{\Omega}_0}J''_{s''}\left(\overline{k}_\perp\overline{r}_{L_0}\right)\right\}$$

$$J_{S_R}^{(s'')} = J'_{m-s''}\left(\overline{k}_\perp\overline{R}_{c_0}\right)J'_{s''}\left(\overline{k}_\perp\overline{r}_{L_0}\right)$$

$$J_{S_\alpha}^{(s'')} = \frac{J_{m-s''-1}\left(\overline{k}_\perp \overline{R}_{c_0}\right) + J_{m-s''+1}\left(\overline{k}_\perp \overline{R}_{c_0}\right)}{2} J'_{s''}\left(\overline{k}_\perp \overline{r}_{L_0}\right).$$

In order to evaluate S_{gyro}, we put (5.19), (5.20) and (5.23) into (5.26) and using the identity (5.24), we find that the resulting relation has terms with $e^{i(\chi_{s'}+\chi_{s''})}$ and $e^{i(\chi_{s'}-\chi_{s''})}$. The terms in the argument of the exponents are given by

$$\begin{aligned} \chi_{s'} + \chi_{s''} &= (\Delta\overline{\omega}_{s'} + \Delta\overline{\omega}_{s''})\overline{z} - (s' + s'')\theta_{p_0} + 2\overline{t}_{q_0} \\ \chi_{s'} - \chi_{s''} &= (\Delta\overline{\omega}_{s'} - \Delta\overline{\omega}_{s''})\overline{z} - (s' - s'')\theta_{p_0}. \end{aligned} \tag{5.28}$$

As the electrons are assumed to be uniformly distributed in $\overline{t}$ and θ before they enter the interaction region, we see from (5.28) that the average over initial phases in (5.26) for all values of s' and s'' is zero except when

$$s = s' = s''$$

where s is the cyclotron harmonic number at which the device operates.

As the next step in evaluating S_{gyro}, we observe that in (5.26) the integration over the axial coordinate $\overline{z}$ is given by

$$I_{\overline{z}} = \int_{-\overline{L}/2}^{\overline{L}/2} f^*(\overline{z}) e^{ik\overline{z}}. \tag{5.29}$$

All other terms are have no $\overline{z}$ dependence in the linear regime and are not affected by the integration. CRM oscillators usually consist of open resonator cavities and so the axial structure of the RF field, $f(\overline{z})$, can be approximated by a Gaussian function:

$$f(\overline{z}) = e^{-\left(\frac{2\overline{z}}{\overline{L}}\right)^2}. \tag{5.30}$$

For a Gaussian function the limits of integration in (5.29) may be extended to $-\infty$ to $+\infty$ with little error. Thus,

$$I_{\overline{z}} = \int_{-\infty}^{\infty} f^*(\overline{z}) e^{ik\overline{z}} = \frac{\overline{L}}{2}\sqrt{\pi} e^{-\frac{k^2\overline{L}^2}{16}}. \tag{5.31}$$

After performing the procedures given above and noting that the Fourier transform $\overline{f}(k)$ in (5.19), (5.20) and (5.23) is given by

$$\overline{f}(k) = \frac{\overline{L}\sqrt{\pi}}{4}\, e^{-\frac{k^2\overline{L}^2}{16}}, \tag{5.32}$$

we get the following relation for S_{gyro}:

$$S_{gyro} = -\frac{\overline{F}_1\overline{L}^2}{32} J_u^s \\ Re\left\{ i\left[J_{S_u}^{(s)} + s J_\theta^{(s)} \right] \int_{-\infty}^{\infty} dk \frac{e^{-\frac{k^2\overline{L}^2}{8}}}{k + \Delta\overline{\omega}_s} - \frac{\overline{\omega}\,\overline{u}_{t_0}^2 J_u^{(s)}}{\gamma_0 \overline{u}_{z_0}} \int_{-\infty}^{\infty} dk \frac{e^{-\frac{k^2\overline{L}^2}{8}}}{(k + \Delta\overline{\omega}_s)^2} \right\} \tag{5.33}$$

When integrated with respect to k, the other terms inside the argument of $Re\{\ \}$ in (5.33) become imaginary and are therefore neglected. The second integral in (5.33) has a double pole at $k = -\Delta\overline{\omega}_s$. So, we integrate by parts to get

$$\int_{-\infty}^{\infty} dk \frac{e^{-\frac{k^2\overline{L}^2}{16}}}{(k + \Delta\omega_s)^2} = -\frac{e^{-\frac{k^2\overline{L}^2}{16}}}{(k + \Delta\overline{\omega}_s)}\Bigg|_{-\infty}^{\infty} - \frac{\overline{L}^2}{4} \int_{-\infty}^{\infty} dk \frac{k e^{-\frac{k^2\overline{L}^2}{16}}}{k + \Delta\overline{\omega}_s}. \tag{5.34}$$

The first part of (5.34) is equal to zero at the limits of integration. Thus we have reduced (5.33) to an equation with a single pole in the denominator.

The integral over k in (5.33) involves a pole in the path of integration. As we are interested only in the imaginary part of the solution (the real part is multiplied by an i in the argument of $Re\{\ \}$ in (5.33)), we may simply take half the residue of the integral evaluated at $k = -\Delta\overline{\omega}_s$ (this will involve a multiplication by a factor of

πi). Thus we get the following relation for the source due to O-type effects.

$$S_{gyro} = -\frac{\overline{F}_1 \pi \overline{L}^2}{32}\, e^{-\frac{(\Delta\overline{\omega}_s \overline{L})^2}{8}} \left\{ J_u^{(s)} \left[J_{S_u}^{(s)} + s J_\theta^{(s)} - \frac{\overline{L}^2 \Delta\overline{\omega}_s \overline{\omega}\, \overline{u}_{t_0}^2}{4\gamma_0 \overline{u}_{z_0}} J_u^{(s)} \right] \right\} \tag{5.35}$$

Now we proceed to evaluate the source term due to M-type effects, S_{penio}. Putting (5.21) and (5.22) into (5.27) and again using the identity (5.24), we find that the resulting relation has terms with $\exp i(\chi_{s'} + \chi_{s''}) \pm i\frac{\overline{\Omega}_0}{\overline{u}_{z_0}}$ and $\exp i(\chi_{s'} - \chi_{s''}) \pm i\frac{\overline{\Omega}_0}{\overline{u}_{z_0}}$. The terms in the argument of the exponents are given by

$$\begin{aligned}
\chi_{s'} + \chi_{s''} \pm \frac{\overline{\Omega}_0}{\overline{u}_{z_0}}\overline{z} &= \left(\Delta\overline{\omega}_{s'} + \Delta\overline{\omega}_{s''} \pm \frac{\overline{\Omega}_0}{\overline{u}_{z_0}} \right) \overline{z} - (s' + s'' \mp 1)\theta_{p_0} + 2\overline{t}_{q_0} \\
\chi_{s'} - \chi_{s''} \pm \frac{\overline{\Omega}_0}{\overline{u}_{z_0}}\overline{z} &= \left(\Delta\overline{\omega}_{s'} - \Delta\overline{\omega}_{s''} \pm \frac{\overline{\Omega}_0}{\overline{u}_{z_0}} \right) \overline{z} - (s' - s'' \mp 1)\theta_{p_0}.
\end{aligned} \tag{5.36}$$

Assuming an initial uniform distribution of electrons in $\overline{t}$ and θ, we see from (5.36) that the average over initial phases in (5.27) for all values of s' and s'' is zero except when

$$s'' = s' \mp 1.$$

Then,

$$\Delta\overline{\omega}_{s'} - \Delta\overline{\omega}_{s''} \pm \frac{\overline{\Omega}_0}{\overline{u}_{z_0}} = 0.$$

After performing the same operation that led to (5.31), we get the following relation for S_{penio}.

$$\begin{aligned}
S_{penio} = &-\frac{\overline{F}_1 \overline{u}_{t_0} \overline{k}_\perp \overline{L}^2}{64\overline{\Omega}_0} \sum_{s'} \\
&\left[Re\left\{ i \left[\left(J_{S_R}^{(s'+1)} - J_{S_\alpha}^{(s'+1)} \right) \left(J_u^{(s')} - J_\theta^{(s')} \right) \int_{-\infty}^{\infty} dk \frac{e^{-\frac{\overline{k}^2\overline{L}^2}{8}}}{k + \Delta\overline{\omega}_{s'} - \frac{\overline{\Omega}_0}{\overline{u}_{z_0}}} \right.\right.\right. \\
&\left.\left.\left. + \left(J_{S_R}^{(s'-1)} + J_{S_\alpha}^{(s'-1)} \right) \left(J_u^{(s')} + J_\theta^{(s')} \right) \int_{-\infty}^{\infty} dk \frac{e^{-\frac{\overline{k}^2\overline{L}^2}{8}}}{k + \Delta\overline{\omega}_{s'} + \frac{\overline{\Omega}_0}{\overline{u}_{z_0}}} \right] \right\} \right]
\end{aligned} \tag{5.37}$$

Other terms inside the argument of $Re\{\ \}$ become imaginary and so are neglected. In (5.37) there are poles at $k = -\Delta\overline{\omega}_{s'} + \frac{\overline{\Omega}_0}{\overline{u}_{z_0}}$ and $k = -\Delta\overline{\omega}_{s'} - \frac{\overline{\Omega}_0}{\overline{u}_{z_0}}$ in the path of integration in the first and second integral, respectively of (5.37). Therefore, using Cauchy's path integral formula we get

$$S_{penio} = \frac{\overline{F}_1 \overline{u}_{t_0} \overline{k}_\perp \overline{L}^2}{64\overline{\Omega}_0} \sum_{s'} \left[\left(J_{S_R}^{(s'+1)} - J_{S_\alpha}^{(s'+1)} \right) \left(J_u^{(s')} - J_\theta^{(s')} \right) e^{-\left(\Delta\overline{\omega}_{s'} - \frac{\overline{\Omega}_0}{\overline{u}_{z_0}}\right)^2 \frac{\overline{L}^2}{8}} + \left(J_{S_R}^{(s'-1)} + J_{S_\alpha}^{(s'-1)} \right) \left(J_u^{(s')} + J_\theta^{(s')} \right) e^{-\left(\Delta\overline{\omega}_{s'} + \frac{\overline{\Omega}_0}{\overline{u}_{z_0}}\right)^2 \frac{\overline{L}^2}{8}} \right] \tag{5.38}$$

As the device operates at the sth cyclotron harmonic, at resonance $s' = s - 1$ and $s' = s+1$ in the first and second part of (5.38), respectively. All other terms become negligible and we do not consider them. Therefore, we get the following relation for S_{penio}:

$$S_{penio} = \frac{\overline{F}_1 \overline{u}_{t_0} \overline{k}_\perp \overline{L}^2}{64\overline{\Omega}_0} e^{(\Delta\overline{\omega}_s)^2 \frac{\overline{L}^2}{8}} \left[\left(J_{S_R}^{(s)} - J_{S_\alpha}^{(s)} \right) \left(J_u^{(s-1)} - J_\theta^{(s-1)} \right) + \left(J_{S_R}^{(s)} + J_{S_\alpha}^{(s)} \right) \left(J_u^{(s+1)} + J_\theta^{(s+1)} \right) \right] \tag{5.39}$$

We can now write the complete source term S by combining S_{gyro} and S_{penio} which is given by

$$\frac{S}{\overline{F}_1} = -\frac{\pi \overline{L}^2}{32}\ \exp\left\{-\frac{(\Delta\overline{\omega}_s\overline{L})^2}{8}\right\}\left\{J_u^{(s)}\left[J_{S_u}^{(s)} + sJ_\theta^{(s)} - \frac{\overline{L}^2\Delta\overline{\omega}_s\overline{\omega}\,\overline{u}_{t_0}^2}{4\gamma_0\overline{u}_{z_0}}J_u^{(s)}\right]\right.$$
$$\left. + \frac{\overline{k}_\perp\overline{u}_{t_0}}{2\overline{\Omega}_0}\left[\left(J_{S_R}^{(s)} - J_{S_\alpha}^{(s)}\right)\left(J_u^{(s-1)} - J_\theta^{(s-1)}\right) + \left(J_{S_R}^{(s)} + J_{S_\alpha}^{(s)}\right)\left(J_u^{(s+1)} + J_\theta^{(s+1)}\right)\right]\right\} \tag{5.40}$$

For convenience, below we rewrite all the "J" terms in (5.40) that we have defined earlier.

$$J_u^{(s)} = J_{m-s}(\overline{k}_\perp\overline{R}_{c_0})J_s'(\overline{k}_\perp\overline{r}_{L_0})$$

$$J_\theta^{(s)} = J_{m-s}(\overline{k}_\perp\overline{R}_{c_0})\frac{sJ_s(\overline{k}_\perp\overline{r}_{L_0})}{\overline{k}_\perp\overline{r}_{L_0}}$$

$$J_u^{(s+1)} = J_{m-(s+1)}(\overline{k}_\perp\overline{R}_{c_0})J_{s+1}'(\overline{k}_\perp\overline{r}_{L_0})$$

$$J_\theta^{(s+1)} = J_{m-(s+1)}(\overline{k}_\perp\overline{R}_{c_0})\frac{(s+1)J_{s+1}(\overline{k}_\perp\overline{r}_{L_0})}{\overline{k}_\perp\overline{r}_{L_0}}$$

$$J_u^{(s-1)} = J_{m-(s-1)}(\overline{k}_\perp\overline{R}_{c_0})J_{s-1}'(\overline{k}_\perp\overline{r}_{L_0})$$

$$J_\theta^{(s-1)} = J_{m-(s-1)}(\overline{k}_\perp\overline{R}_{c_0})\frac{(s-1)J_{s-1}(\overline{k}_\perp\overline{r}_{L_0})}{\overline{k}_\perp\overline{r}_{L_0}}$$

$$J_{S_u}^{(s)} = J_{m-s}\left(\overline{k}_\perp\overline{R}_{c_0}\right)\left\{J_{m-s}'\left(\overline{k}_\perp\overline{r}_{L_0}\right) + \frac{\overline{k}_\perp\overline{u}_{t_0}}{\overline{\Omega}_0}J_s''\left(\overline{k}_\perp\overline{r}_{L_0}\right)\right\}$$

$$J_{S_R}^{(s)} = J_{m-s}'\left(\overline{k}_\perp\overline{R}_{c_0}\right)J_s'\left(\overline{k}_\perp\overline{r}_{L_0}\right)$$

$$J_{S_\alpha}^{(s)} = \frac{J_{m-s-1}\left(\overline{k}_\perp\overline{R}_{c_0}\right) + J_{m-s+1}\left(\overline{k}_\perp\overline{R}_{c_0}\right)}{2}J_s'\left(\overline{k}_\perp\overline{r}_{L_0}\right).$$

5.4 Starting conditions

The starting conditions for the self excitation of the device are fulfilled when the combined RF losses in the interaction cavity equal the RF gain due to the electron beam-wave interaction. Under such conditions the left hand side of (5.3) becomes zero and we can write the energy balance equation as

$$\frac{2\hat{I}Q\,S}{\overline{F}_1} = 1 \tag{5.41}$$

Using (5.41) we can calculate the self excitation conditions for a given mode.

Chapter 6

Studies on a gyro-peniotron working in the $TE_{0,2}$-mode

In this chapter we use the nonlinear and linear theories that we developed in the last two chapters to study the characteristics of a gyro-peniotron oscillator working in the $TE_{0,2}$ - mode. The device is assumed to operate in the fundamental cyclotron harmonic. We have also analyzed the gyrotron operation for the same mode to compare the operation mechanism of the two regimes viz., gyrotron and gyro-peniotron.

The gyro-peniotron regime is studied in considerable depth over different cavity lengths, magnetic field detuning and RF field amplitude using the nonlinear theory. We have used (4.38) along with (4.36) and (4.37) to study temporal evolution of a gyro-peniotron mode. We have used the linear theory to study the starting conditions for self excitation of the $TE_{0,2}$ - mode for both gyrotron as well as gyro-peniotron operation. As $TE_{-2,2}$ - mode and $TE_{-3,2}$ - mode are the closest

in operating frequency for the $TE_{0,2}$ - mode, we have studied the starting conditions for these two modes also to study the possibility of mode competition.

6.1 Cyclotron harmonics for gyro-peniotron operation

In (4.36), we see that the number of harmonics required to calculate the momentum and phase of the electrons is infinite (from $s = -\infty$ to $s = \infty$). However, it is not only impractical but also unnecessary to consider all the harmonics. We only need to consider those harmonics that are resonant with the RF wave. The contribution from all other harmonics to the electron-wave interaction is negligible. As we can see from (5.40), the cyclotron harmonics that are resonant with the RF wave are s, $s-1$ and $s+1$ where s is the resonant harmonic number at which the device operates. For fundamental cyclotron harmonic operation that we will be studying, we need to consider only $s = 0, 1, 2$ in (4.36).

6.2 Alternate normalization: μ, Δ, F

We will assume that the axial dependence of the field is fixed to be a Gaussian corresponding to a normalized cavity length $\overline{L}$.

$$f(z) = e^{-\left(\frac{2\overline{z}}{\overline{L}}\right)^2}$$

which is a fixed gaussian field structure for a normalized cavity length $\overline{L}$. We will use a fixed gaussian axial field structure for all our studies in this chapter.

The gyrotron community popularly uses the following normalizations for cavity length, magnetic field detuning and field amplitude defined in terms of the normalized quantities given in Section. 4.3, respectively, as (see for example [9, 42])

$$\mu = \pi \left(\frac{\overline{u}_{\perp_0}^2}{\gamma_0 \overline{u}_{z_0}} \right) \left(\frac{\overline{L}}{\overline{\lambda}} \right)$$

$$\Delta = \frac{2\gamma_0^2}{\overline{u}_{\perp_0}^2} \left(1 - \frac{s\overline{\Omega}_0}{\gamma_0 \overline{\omega}} \right)$$

$$F_g = \frac{\overline{E}_0 \gamma_0^3}{\overline{\Omega}_0 \overline{u}_{t_0}^3} J_{m\pm1} \left(\overline{k}_\perp \overline{R}_c \right)$$

where we have considered fundamental harmonic operation. $\overline{R}_c, \overline{L}$ and $\overline{\lambda}$ are the normalized electron beam guiding center radius, normalized and normalized wavelength of the RF wave in free space, respectively. Generally for gyrotron operation, the electron beam is placed where the Bessel function in the equation defining F_g is maximum. When we include the peniotron effects and place the beam near the null of the the RF electric field, F_g becomes zero. As F_g is defined only for a gyrotron where peniotron effects are neglected, this normalized quantity cannot be used to study peniotrons. So, we define another normalized field amplitude, F, for our studies where peniotron effects are not neglected.

$$F = \frac{\overline{E}_0 \gamma_0^3}{\overline{\Omega}_0 \overline{u}_{t_0}^3} J_{m\pm1} \left(\overline{k}_\perp \overline{R}_{c_{max}} \right)$$

Here $\overline{R}_{c_{max}}$ is the normalized radius corresponding to the maximum value of the Bessel function in the preceding equation. The Bessel function in F has a fixed value independent of the beam position. Hence, the results of a peniotron can be readily compared to the results of a gyrotron available in the literature as F_g is the

same as F for a gyrotron as the beam is usually placed at the normalized guiding center radius $\overline{R}_{c_{max}}$.

The efficiency of a CRM is given by

$$\eta = \frac{\gamma_0 - \langle\gamma\rangle}{\gamma_0 - 1} = \left[\frac{u_{\perp_0}^2}{2c^2\gamma_0(\gamma_0 - 1)}\right]\eta_\perp$$

where

$$\eta_\perp = \frac{\frac{u_{\perp_0}^2}{\gamma_0} - \left\langle\frac{u_\perp^2}{\gamma}\right\rangle}{\frac{u_{\perp_0}^2}{\gamma_0}}. \tag{6.1}$$

$< \cdots >$ implies the average over all the electrons. (6.1) is simply the change in the average kinetic energy of the electrons with respect to initial kinetic energy.

We will be assuming a fixed gaussian axial structure for any given mode. Also we assume the following electron beam characteristics: beam current of 40 A, a beam voltage of 80 kV, velocity pitch factor of 1.5. A cavity Q-factor of 4000 is assumed when studying the temporal evolution of modes.

6.3 Guiding center motion and peniotron effects

The functioning of a peniotron is fundamentally different from a gyrotron due to two important effects viz., the motion of the electron guiding center and the slow and fast peniotron effects. Our simulations show that in the case where the electron guiding center is fixed and also in the case when the fast and slow peniotron effects are neglected (by considering $s = 1$ in in (4.36)), there is very little change in the electron energy due to interaction with the RF wave when the electron beam is positioned at the null of the RF electric field. However, when these two effects

are included in the calculations we see that the energy for all electrons changes as they move along the axis of the interaction cavity. Fig. 6.1 shows a typical case of a gyro-peniotron where seventeen electrons experience varying changes in their momentum, progressively losing their energy to the RF wave leading to the growth of the wave. Here we have chosen $\Delta = 0.3$, $\mu = 10$ and $F = 0.8$. Notice the oscillatory nature of the changes of the momentum of the electrons as they move along the axis due to the acceleration and deceleration of the electrons caused by peniotron action. However, overall deceleration is greater than acceleration and therefore, on an average, electrons give up energy to the wave leading to wave growth. We also observe that there are no electrons that have a larger momentum at the end of the interaction region than at the start. So, there is no net absorption of energy from the wave by any electron leading to the possibility of a very large efficiency, when appropriate parameters are chosen.

For the same parameters used in Fig. 6.1, Fig. 6.2 shows the trajectory of four electrons as seen on a plane moving along the axis of the cavity at a rate of the axial velocity of the electrons. It can be seen that the electrons spiral into smaller and smaller orbits whose guiding centers also move away from the initial position. It can also be observed that the electron motion is such that the guiding centers of the electrons move in different directions causing electron spacial segregation. Fig. 6.3 shows the position of the seventeen electrons considered in the simulation at different axial positions as they interact with the EM wave in the gyro-peniotron interaction. It is clear that the electrons do not form bunches, rather they get segregated from each other as they move along the axis of the interaction region.

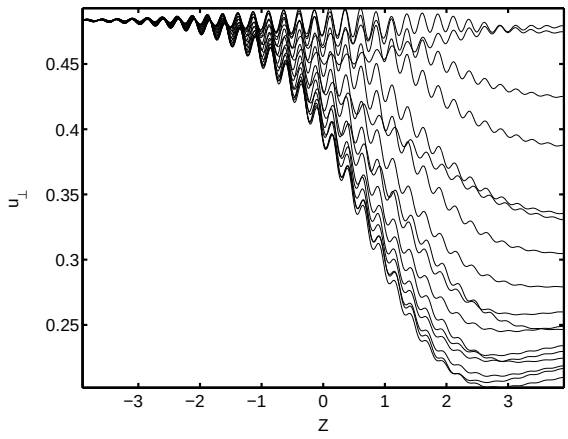

Figure 6.1: Change in normalized electron momentum as the electrons pass through the interaction region due to peniotron action for parameters $\mu = 10$, $\Delta = 0.3$ and $F = 0.8$

To compare the gyro-peniotron interaction described above with gyrotron action, we consider the case of the electron beam placed for maximum interaction with the RF wave as shown in Fig. 2.1. In Fig. 6.4, we have shown the electron positions for different planar positions along the axis of the interaction region for the case of a fundamental harmonic gyrotron working in the $TE_{0,2}$ - mode. We can see that the electrons tend to form bunches. These bunched electrons give up their kinetic energy to the wave. However, we can also see that some of the electrons are not bunched which absorb energy from the wave. Fig. 6.5 shows the change in the normalized transverse momentum of the electrons as they move along the axis of the interaction region for gyrotron interaction. Except for an initial acceleration followed by deceleration, most of the electrons are decelerated monotonically unlike in a gyro-peniotron where the electrons are both accelerated and decelerated in every

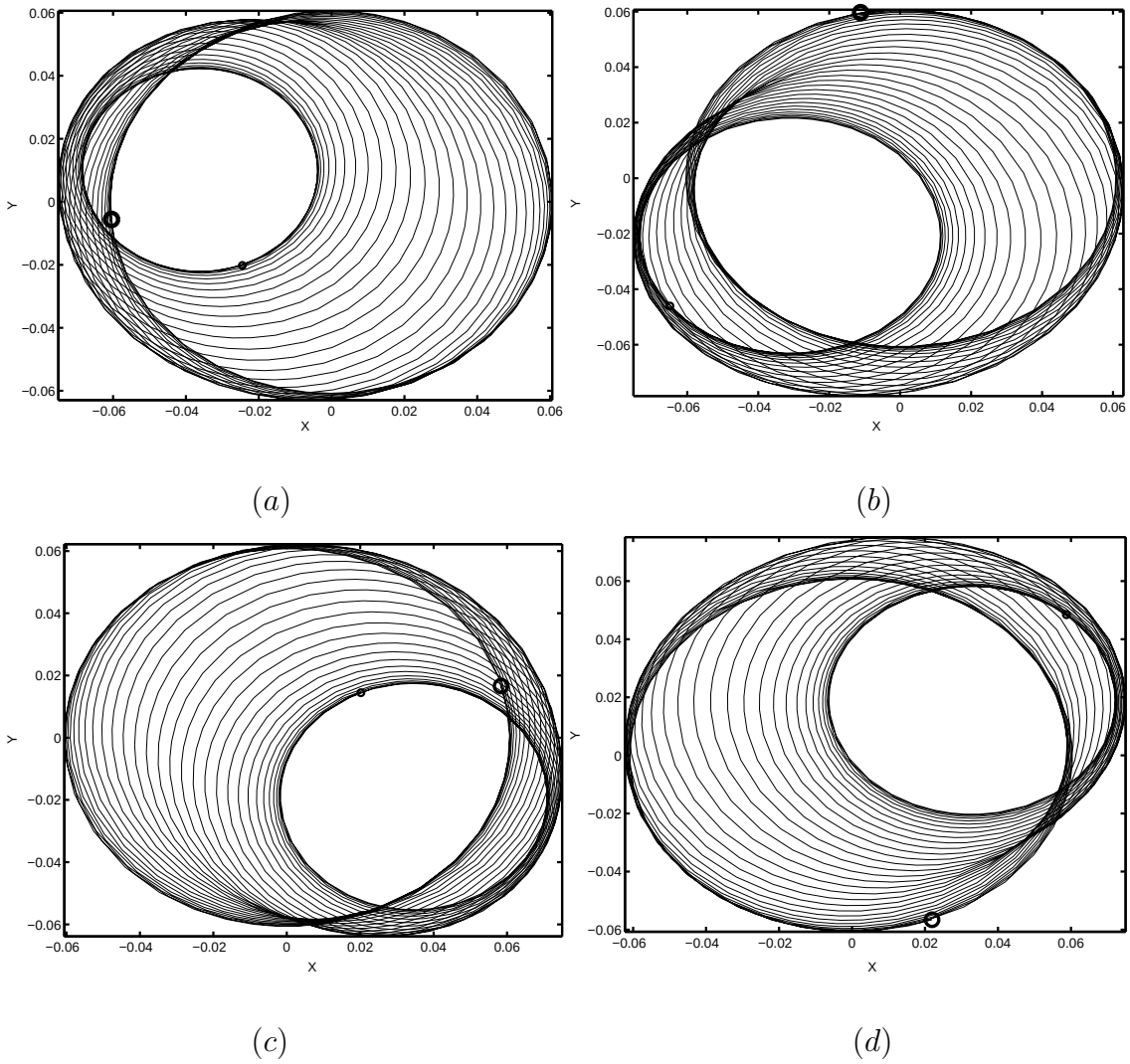

Figure 6.2: Orbital trajectories for four peniotron electrons starting at different RF phase positions. The initial and final positions of the electrons is shown by two small circles, the bigger circle represents the initial position and the smaller circle represents the final position (the origin is taken as the unperturbed guiding center of the electrons).

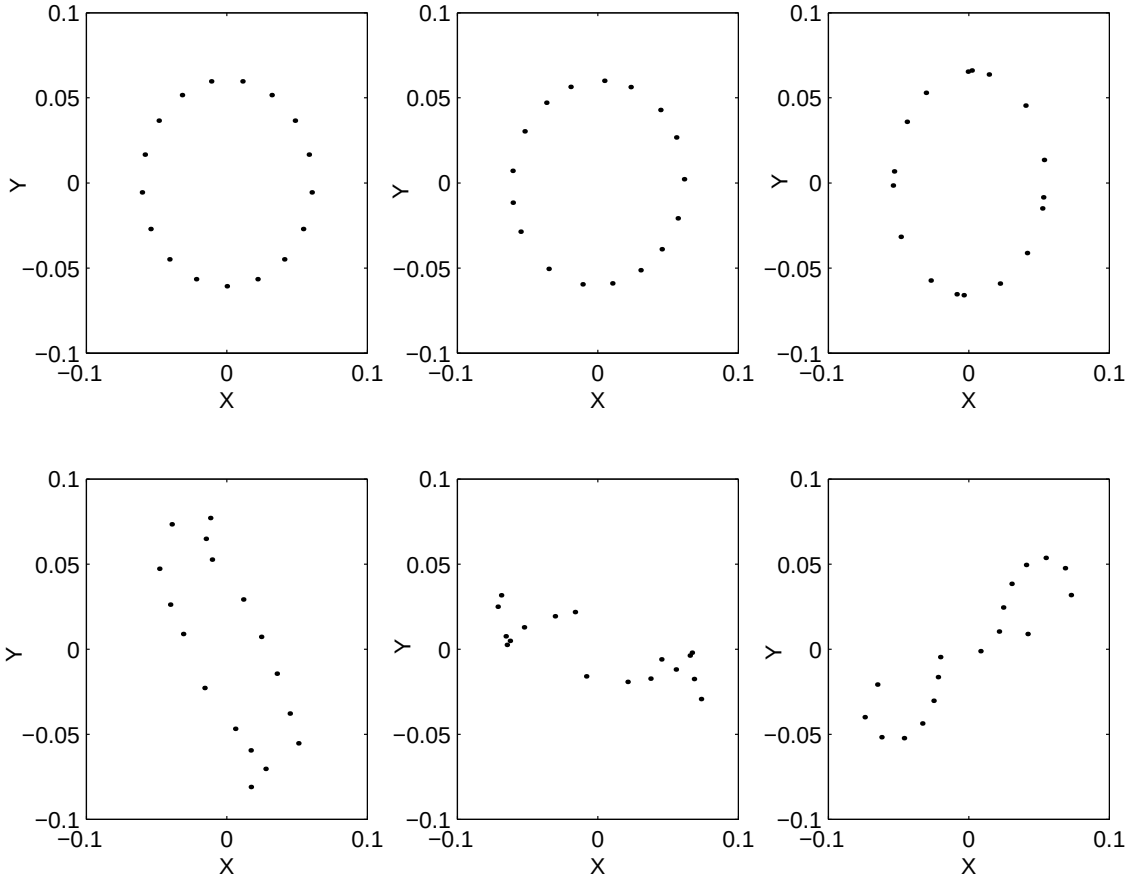

Figure 6.3: Electron segregation in a gyro-peniotron interaction. Projection of electron positions for seventeen electrons considered at different axial positions $z = 0, z = 0.1L, z = 0.25L, z = 0.5L, z = 0.75L$ and $z = L$ (L is the cavity length) for parameters $\mu = 10$, $\Delta = 0.3$ and $F = 0.8$ (the origin is taken as the unperturbed guiding center of the electrons).

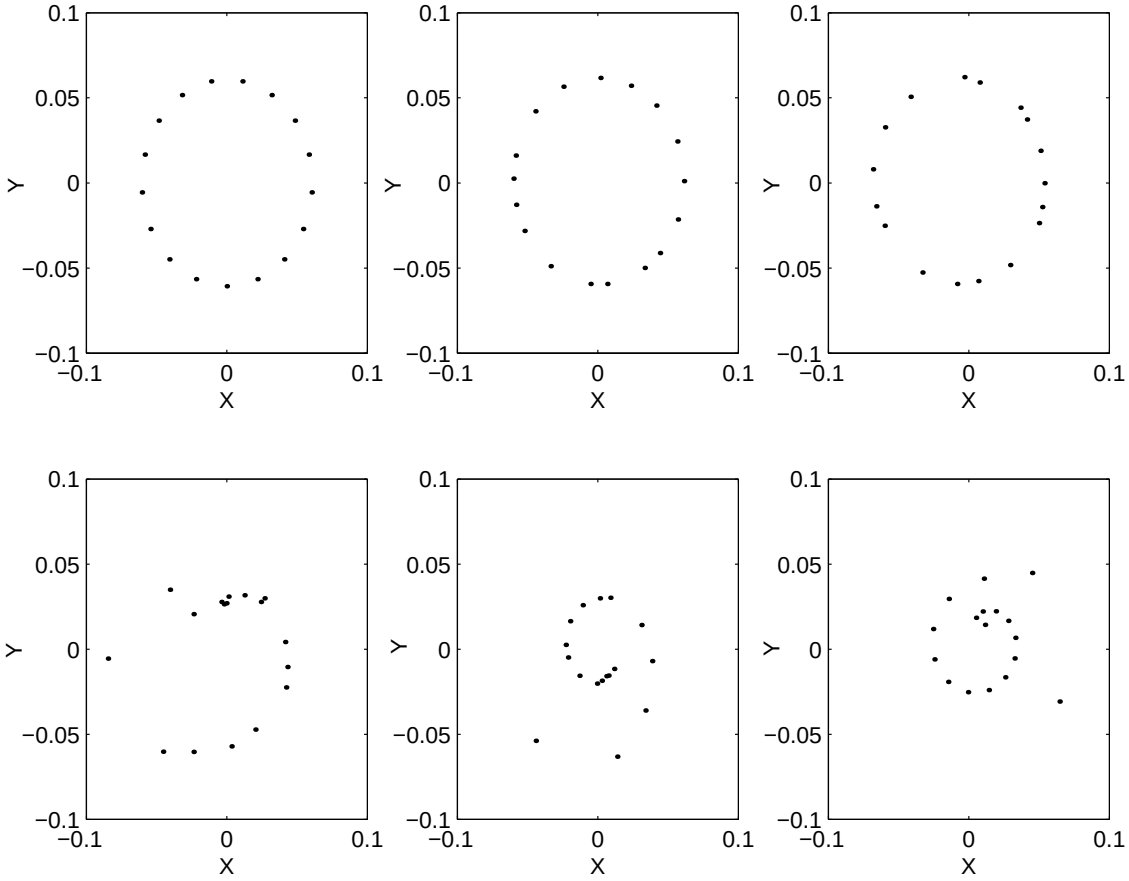

Figure 6.4: Bunching process in a gyrotron interaction. Projection of electron positions for seventeen electrons considered at different axial positions $z = 0, z = 0.1L, z = 0.25L, z = 0.5L, z = 0.75L$ and $z = L$ (L is the cavity length) for parameters $\mu = 10$, $\Delta = 0.3$ and $F = 0.15$ (the origin is taken as the unperturbed guiding center of the electrons).

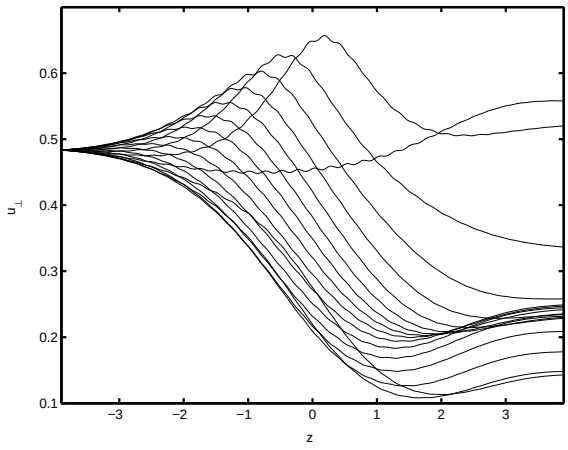

Figure 6.5: Change in normalized electron momentum as the electrons pass through the interaction region due to gyrotron action for parameters $\mu = 10$, $\Delta = 0.3$ and $F = 0.15$.

gyro-cycle throughout the interaction. In this case where we have considered seventeen electrons, we see that for two electrons the transverse momentum increases unlike other electrons whose momentum falls. These electrons which are the same as the unbunched electrons in Fig. 6.4 are in the acceleration phase and absorb energy from the RF wave, thus limiting the device efficiency. Hence, a gyrotron efficiency is limited due to the nature of interaction where some electrons absorb energy from the wave, whereas the gyro-peniotron efficiency can be potentially very high as, on an average, RF energy is not absorbed by any of the electrons.

6.4 Efficiency dependence on F, Δ and μ

The perpendicular efficiency defined in (6.1) of a gyro-peniotron (electron beam radius corresponding to the null of the EM mode) working in the funda-

mental harmonic is dependent on the cavity length (μ), mode amplitude (F), and cyclotron frequency detuning (Δ). As the cavity length is fixed for a device, in our calculations we assume μ as a fixed parameter and calculate the efficiency for various values of Δ and F. In Fig. 6.6 we have shown the change in transverse efficiency with the normalized amplitude F for different magnetic field mismatch Δ. We have considered four different cavity lengths for our study ($\mu = 5, 7.5, 10$ and 15).

We can see that for short cavity lengths ($\mu = 5$), dependence of efficiency on the magnetic field mismatch is small compared to long cavity lengths. Therefore, for short cavity lengths the performance of the device is not affected much by variation in external magnetic field. Another advantage is that generally gyrotrons have very large start current requirements for short cavity lengths. So, mode competition for a gyro-peniotron mode from a gyrotron mode is likely to be less severe for short cavity lengths. However, as can be seen from Fig. 6.6a high efficiencies are possible only for large RF amplitudes F for $\mu = 5$. As power handling capacity of a cavity of short length is limited, it might not be possible to achieve large RF amplitudes and hence large efficiencies.

For longer cavity lengths, say $\mu = 15$, we see from Fig. 6.6d that the efficiency grows faster (at low RF amplitudes) with increase in RF amplitude for smaller values of magnetic field mismatch Δ. However, for larger Δ, the efficiency starts to grow only at larger RF amplitudes. This indicates that the small signal growth rate is higher for smaller Δ. However, for small Δ, we see that the efficiency saturates at a low level, then falls off before it rises again with increase in RF amplitude. In a free running oscillator, it is unlikely that the RF amplitude will rise beyond

the first saturation point for a given Δ. An increase in RF amplitude beyond the first efficiency saturation point will reduce the efficiency which in turn will reduce the RF power (and RF amplitude) in the cavity. Thus, in order to achieve high levels of efficiencies from low starting RF amplitudes, the design should incorporate a start-up scenario where the oscillations are triggered at a low value of Δ and as the RF amplitude grows, Δ may be tuned to larger values (by changing the electron gun parameters). As can be seen from Fig. (6.6)d, when the RF amplitude is large enough, the efficiency grows to high levels for a large Δ, which is in the hard excitation regime. It should also be noted that for a cavity length of $\mu = 15$, an efficiency $> 90\%$ can be achieved for a relatively low RF amplitude compared to a cavity length of $\mu = 5$.

It should be noted that this kind of start-up scenario for longer cavities might be difficult because the magnetic field mismatch Δ has to be increased precisely as the RF amplitude increases. If Δ is increased too fast the RF amplitude may not be large enough to fulfill sustainable oscillatory conditions. Also, for cavity lengths $\mu > 15$, the mode competition from gyrotron modes can be stronger. Therefore, for a gyro-peniotron, the cavity length should neither be too short so that the cavity can handle large enough power and at the same time the cavity length should not be too long so that the competition from gyrotron modes is not too strong as well as to reduce the complexity of the start-up scenario. We have shown perpendicular efficiency curves for different Δ as a function of normalized RF amplitude for $\mu = 7.5$ and $\mu = 10$ in Fig. 6.6b and Fig. 6.6c, respectively. We can see from these figures that a cavity length of $\mu = 10$ seems to be a good compromise in terms of power

handling capacity and small signal growth rate.

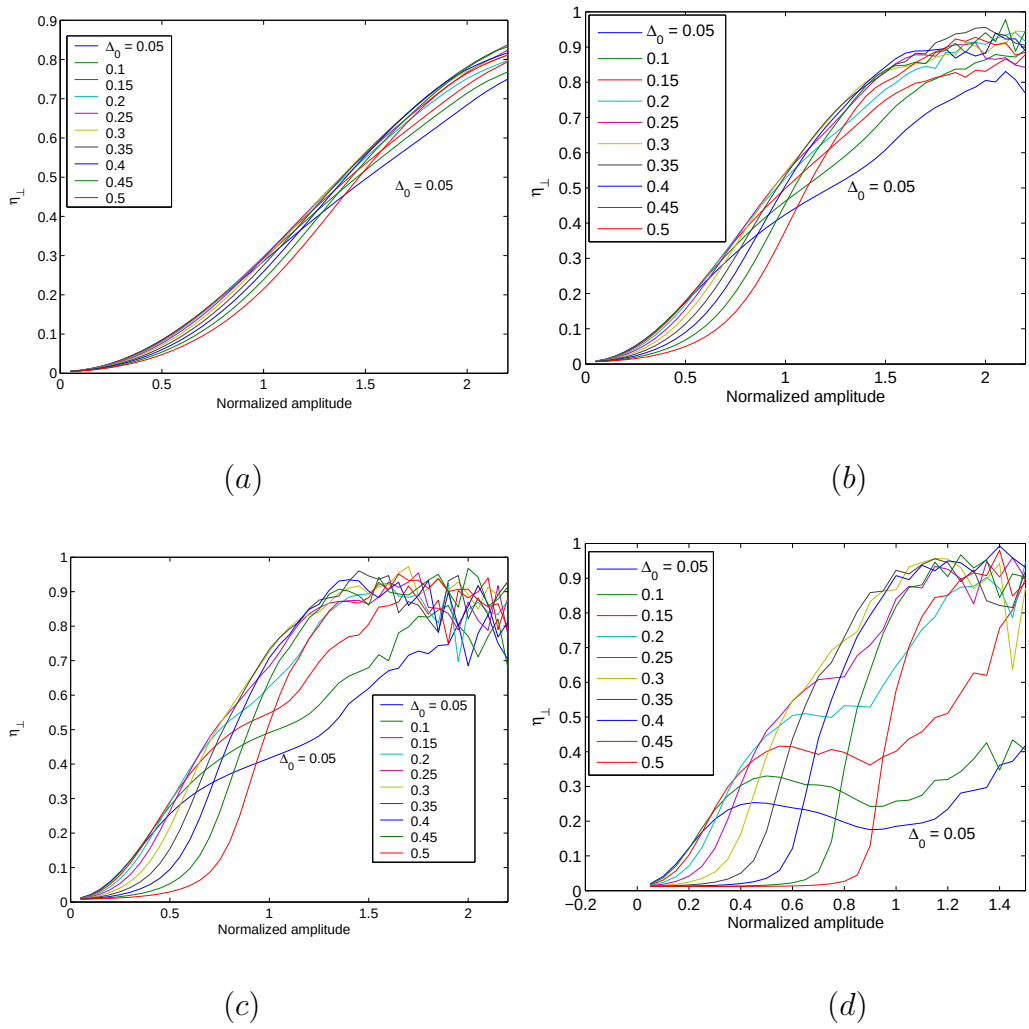

Figure 6.6: Transverse efficiency as a function of normalized mode amplitude F, for different magnetic field mismatch Δ_0 for (a) $\mu = 5$, (b) $\mu = 7.5$, (c) $\mu = 10$ and (d) $\mu = 15$

It will be convenient to present the results of Fig. 6.6 as a single contour plot of the efficiency $\eta_\perp$ in the Δ - F plane. However, it would be more useful to plot the contours in terms of a normalized current parameter I_0 defined by

$$I_0 = 0.47 \times 10^{-3} IQ \frac{\gamma_0^3 c^4}{u_{\perp_0}^3 u_{z_0}} \left[J_{m-1}\left(k_\perp R_{c_{max}}\right)\right]^2 \left[J_m^2(\nu)(\nu^2 - m^2)\int_0^L |f|^2 dz\right]^{-1} \quad (6.2)$$

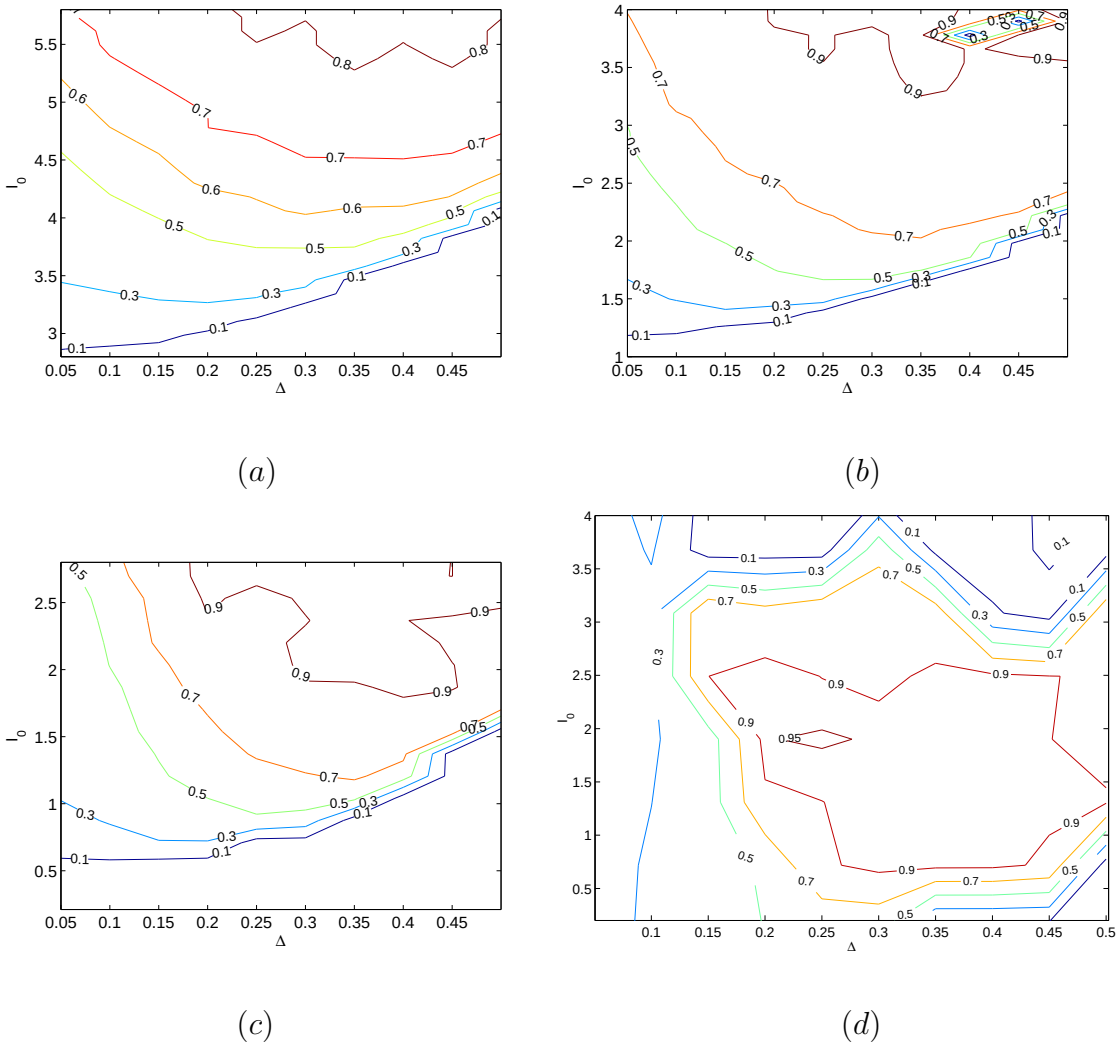

Figure 6.7: Contour plot of transverse efficiency $\eta_\perp$ as a function of normalized beam current I_0 and magnetic field mismatch Δ for fundamental cyclotron interaction for normalized cavity lenghts of (a) $\mu = 5$, (b) $\mu = 7.5$, (c) $\mu = 10$ and (d) $\mu = 15$

where I is the beam current (in amperes). I_0 is related to F through the energy balance equation

$$F^2 = \eta_\perp I_0 \tag{6.3}$$

We can see from Fig. 6.7 that for shorter cavity lengths like $\mu = 5$, a very large I_0 is needed in order to achieve high perpendicular efficiencies. From (6.2) we see that a large I_0 implies that either the cavity Q or the beam current I should be large. A large Q cavity implies that more energy is stored inside the cavity which may lead to unacceptable levels of cavity wall heating. Though a large beam current can increase the efficiency, it can lead to large amount of RF power generated which can also cause wall heating. I_0 can also be large when the electron velocity pitch factor is small. However, when the electron velocity pitch factor is small, the overall efficiency of the device becomes small as the energy in the axial component of the electron velocity is not converted into wave energy. All these factors make a gyro-peniotron working at short cavity lengths not very attractive.

In long cavities ($\mu > 15$), maximum efficiency regions ($> 90\%$) can be achieved at relatively low cavity Q and beam current I as can be seen from Fig. 6.7d. However, we see from Fig. 6.6 that a very large RF amplitude is required to attain high efficiency at large Δ. So, in order to reach the high efficiency regimes, a start-up scenario should be established such that the device is first triggered at very low Δ and then as the ampitude of the wave increases the detuning should be increased to reach high efficiency regions. From these considerations it seems a cavity length

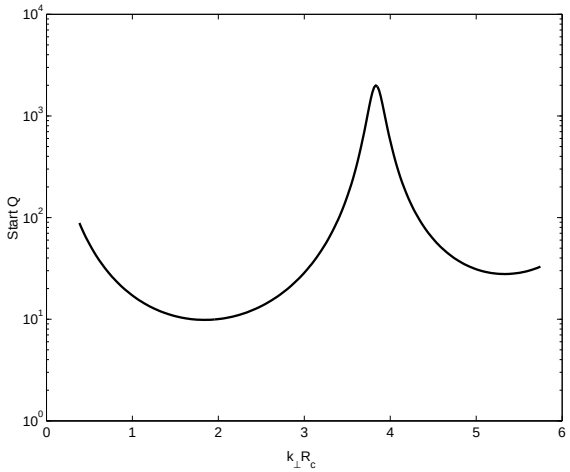

Figure 6.8: Start Q as a function of beam radius for a cavity length $\mu = 10$ and magnetic detuning $\Delta = 0.2$. Start Q is minimum when the beam is positioned for gyrotron interaction (< 10) and maximum when the beam is positioned for gyro-peniotron interaction (~ 2000).

of $\mu = 10$ seems to be a reasonable compromise.

6.5 Starting conditions for gyro-peniotron

The self excitation conditions for a given mode are satisfied when the combined losses in the interaction cavity are balanced by the RF gain due to the interaction between the RF wave and the electron beam. We will use equation (5.41) to estimate the minimum Q that is necessary for self excitation of a mode for various operating parameters that may be calculated from (5.40) and (5.5).

We have assumed a beam voltage of 80kV, a beam current of 40 A and a velocity pitch factor of 1.5 in all the results presented in this section.

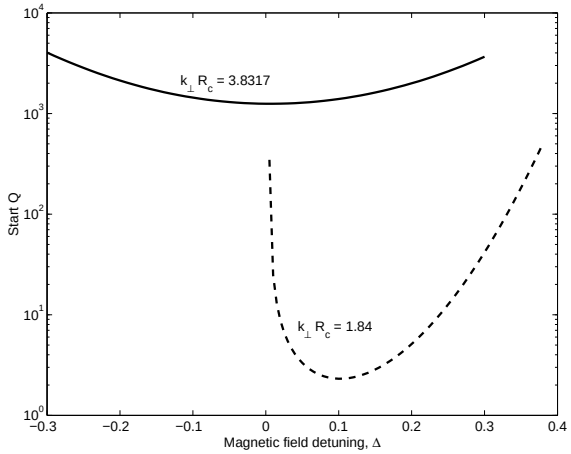

Figure 6.9: Start Q as a function of magnetic field detuning, Δ, for the electron beam positioned for gyro-peniotron interaction (solid line) and for gyrotron interaction (dashed line) for a normalized cavity length $\mu = 10$.

In Fig. 6.8 we have shown the minimum Q required for self excitation as a function of beam radius. We can see from Fig. 6.8 that when the electron beam is positioned for gyrotron interaction ($k_\perp R_c = 1.84$), the start Q is very low (< 10). It should be noted that usually for optimum operation of a gyrotron, the start Q is higher when the detuning factor $\Delta \sim 0.5$. From Fig. 6.8 we also note that when the electron beam is positioned at the RF null ($k_\perp R_c = 3.8317$) when the M-type gyro-peniotron effects dominate, the start Q is very high (~ 2000). This implies that for a gyro-peniotron to self excite either a high Q interaction cavity or a high power electron beam is necessary.

Fig. 6.9 shows start Q as a function of magnetic field detuning, Δ, for a fixed cavity length of $\mu = 10$. It can be seen that for negative detuning a gyrotron's self excitation conditions are not fulfilled as the electrons absorb energy from the

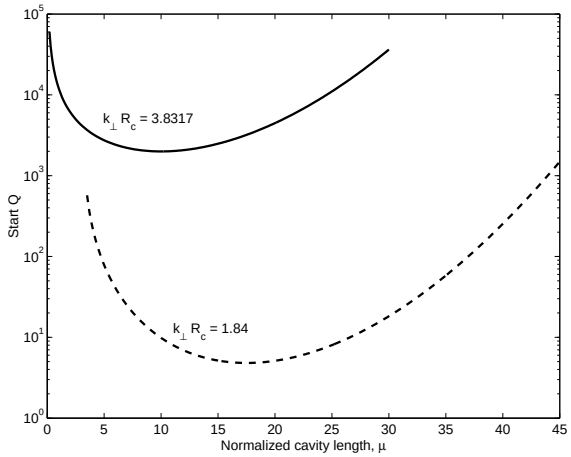

Figure 6.10: Start Q as a function of normalized cavity length μ for the electron beam positioned for gyro-peniotron interaction (solid line) and for gyrotron interaction (dashed line) for a magnetic field detuning $\Delta = 0.2$.

RF fields. But in the case of gyro-peniotron, we see that self excitation conditions are fulfilled even for negative detuning. Moreover, the start Q is the least for zero detuning and increases symmetrically about zero detuning. Such symmetry with respect to the detuning is a general feature for all M-type devices.

Fig. 6.10 shows start Q as a function of normalized cavity length, μ, for a magnetic field detuning of $\Delta = 0.2$. We can see that for the detuning parameter considered, the gyro-peniotron interaction has the lowest start Q for a cavity length, $\mu \simeq 10$ while the gyrotron interaction has the lowest start Q for $\mu \simeq 18$.

6.6 Mode competition

The factor $(k_{\perp}R_{wall})$ gives the eigenvalue of a given mode. Here $k_{\perp}$ is the transverse wave number inside the interaction region for the mode under consideration and R_{wall} is the interaction cavity wall radius. The frequency of operation for a given mode is proportional to its eigenvalue. The eigenvalue spectrum becomes denser as the order of modes increases. As a gyro-peniotron requires a very large Q or a high power electron beam, the chances of a gyro-peniotron mode exciting in a low order mode is greater than in high order modes. The $TE_{0,2}$ - mode is the lowest order mode that can operate in the gyro-peniotron regime. As the density of modes around a low order mode is small, the number of competing modes for this mode will be relatively less.

The eigenvalue for the $TE_{0,2}$ - mode is 7.0156. The closest modes to the $TE_{0,2}$ - mode in the eigenvalue spectrum are the $TE_{-2,2}$ - mode and the $TE_{-3,2}$ - mode with eigenvalues of 6.7062 and 8.0153, respectively. Therefore, we will consider these two modes as possible candidates for mode competition for the $TE_{0,2}$ - mode. All other modes are too far in the eigenvalue spectrum to pose serious mode competition for the $TE_{0,2}$ - mode. The '-' sign in the subscript in $TE_{-2,2}$ and $TE_{-3,2}$ indicates that the RF field of those modes rotate in a direction opposite to the electron gyro motion.

Fig. 6.11 shows the start Q as a function of the normalized cyclotron frequency for three modes $TE_{-2,2}$, $TE_{0,2}$ and $TE_{-3,2}$ for a cavity length $\mu = 10$ and beam position corresponding to the null of the $TE_{0,2}$ - mode. The minimum start Q for

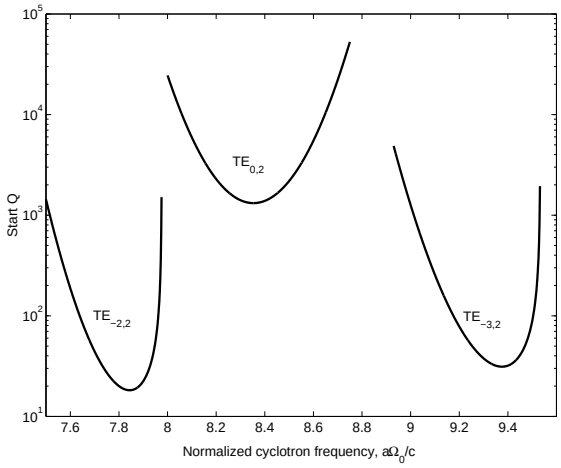

Figure 6.11: Start Q as a function of normalized cyclotron frequency $\overline{\Omega}_0$, for $TE_{-2,2}$, $TE_{0,2}$ and $TE_{-3,2}$ modes for an electron beam radius corresponding to the null of the $TE_{0,2}$ - mode.

the $TE_{0,2}$ - mode is ~ 1250 at $\Omega_0 = 8.35$. We can see from Fig. 6.11 that the two possible competing modes $TE_{-2,2}$ and $TE_{0,2}$ have much lower minimum start Q than that of the gyro-peniotron $TE_{0,2}$ - mode. However, it can be observed that for the cyclotron frequency at which the gyro-peniotron mode operates, the two competing $TE_{-2,2}$ and $TE_{0,2}$ modes do not satisfy the requirements for self excitation.

This result shows that the gyro-peniotron mode operating in the $TE_{0,2}$ - mode can be excited without mode competition from any gyrotron mode if its self excitation conditions are fulfilled. This shows that it may be possible to develop a gyro-peniotron that can deliver very high powers at a very high efficiency.

We have also studied the mode competition for a gyro-peniotron working at a higher order mode viz., $TE_{0,4}$. The adjacent modes in the eigenvalue spectrum for this mode are $TE_{-2,4}$ and $TE_{-3,4}$ modes. The electron beam radius corresponds to

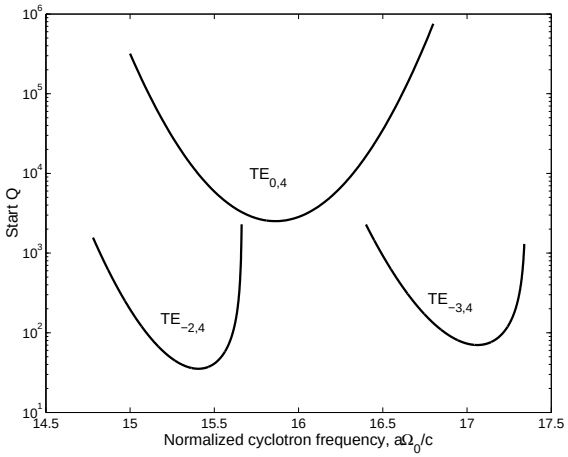

Figure 6.12: Start Q as a function of normalized cyclotron frequency $\overline{\Omega}_0$, for $TE_{-2,4}$, $TE_{0,4}$ and $TE_{-3,4}$ modes for an electron beam radius corresponding to the first null of the $TE_{0,4}$ - mode.

the first RF null of the $TE_{0,4}$ - mode. We see from Fig. 6.12 that the minimum start Q required for the gyro-peniotron mode is ~ 2400 which is nearly double that of the minimum start Q that for the lower order $TE_{0,2}$ - mode. We also observe that for a normalized cyclotron frequency range of 15.4 to 15.7 the $TE_{-2,4}$ - mode has lower start Q than the $TE_{0,4}$ - mode and can potentially compete with the gyro-peniotron mode. However, $TE_{-3,4}$ - mode is out of range to pose any serious mode competition to the gyro-peniotron mode. Though the $TE_{-2,4}$ - mode can suppress the gyro-peniotron mode, there is still a range of cyclotron frequencies over which only the $TE_{0,4}$ - mode can be excited ($15.72 < \Omega_0 < 16.3$) and so gyro-peniotron operation seems possible at even this high order mode.

From these results we see that a gyro-peniotron mode has the possibility of self excitation without serious mode competition from gyrotron modes. However, when

operated at higher order modes there are chances of mode competition form gyrotron modes and at very high order modes gyrotron modes will most likely suppress gyro-peniotron modes.

6.7 Temporal evolution of a gyro-peniotron mode

We have seen from the linear analysis of the previous section that a gyro-peniotron operating in the $TE_{0,2}$ - mode does not experience mode competition from gyrotron modes that are adjacent in the eigenvalue spectrum. Therefore it is enough to study the evolution of a gyro-peniotron mode without considering any other mode.

We have used equations (4.36) and (4.37) to calculate the transverse momentum, gyro-phase and guiding center motion of the electrons as they stream down the interaction cavity, in the fast time scale. We have assumed a fixed Gaussian axial field structure in our calculations as done for other simulations in this chapter. The numerical solution of (4.36) and (4.37) is then used in (4.38) to calculate the amplitude of the RF wave for the next time step in the temporal evolution of the RF wave. This procedure is repeated until the mode amplitude "saturates". We have assumed a normalized cavity length $\mu = 10$ and a detuning factor $\Delta = 0.2$ in this simulation. In Fig. 6.13 we show the temporal evolution of a gyro-peniotron mode operating in the $TE_{0,2}$ - mode where the initial amplitude of the RF wave is very low. We can see from Fig. 6.13 that the gyro-peniotron mode can be excited at a low amplitude and follows a linear growth at low RF amplitude confirming

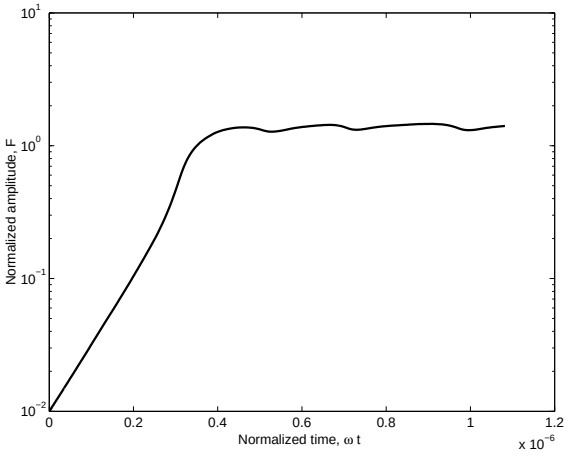

Figure 6.13: Temporal evolution of a $TE_{0,2}$ - mode starting at a low amplitude, operating in the gyro-peniotron regime with a normalized cavity length $\mu = 10$ and a cyclotron frequency detuning factor $\Delta = 0.2$.

the conclusions of the linear theory that a gyro-peniotron can be self excited. The mode then grows non-linearly to eventually saturate at around a normalized mode amplitude $F \simeq 1.4$. From Fig. 6.6, we see that for the cavity length and detuning factor considered, the device transverse efficiency is around 90%.

This result shows that a high power, highly efficient gyro-peniotron oscillator that can be self excited seems possible. However, it should be noted that such high power generation can have severe limitations for CW operation of the device due to the heat generated in the cavity walls. For example, for a gyro-peniotron operating in the $TE_{0,2}$ - mode, at $35GHz$, with a cavity length of $\mu = 10$ and a magnetic field detuning $\Delta = 0.2$, the ohmic power loss in the cavity wall is about $36kW/cm^2$. This ohmic power loss is almost an order higher than what the present cooling systems for vacuum devices can handle. Therefore, the high efficiency gyro-peniotrons can

only be operated in short pulses so that the heat generated in the cavity due to ohmic losses can be within manageable limits.

Chapter 7

Start currents in an overmoded gyrotron

The gyrotrons being developed for electron cyclotron resonance plasma heating and current drive in fusion reactors generate MW-level powers in long pulses approaching continuous wave (CW) operation [8]. In order to keep the power density of ohmic losses in the gyrotron cavity within manageable limits, the interaction space in these gyrotrons should be sufficiently large. This necessitates the operation in a high order mode in the presence of many competing modes. For optimum performance, the device should be designed such that the desired mode dominates and suppresses all other modes during the transition of the device parameters to the operating point. Such selective excitation of the desired mode is an extremely difficult problem due to the presence of many competing modes [43, 44, 34, 45]. Therefore, studying the start-up scenario in the design of such a gyrotron operating at high-order modes is extremely important.

One of the methods used to study the start-up scenario is to study the start currents required to trigger each of the competing modes. The mode for which the self-excitation conditions will be fulfilled first during the voltage and current rise is likely to dominate the mode competition. In principle, some non-linear effects are also possible. Other modes can be triggered by the presence of the first mode to reach large amplitude. So, it is also important to study these effects in order to make sure that the required mode alone dominates the mode competition. We have presented an analysis based on the use of the linear theory in [35] and nonlinear theory in [46].

In this chapter we extend the linear theory developed in [37] to calculate start currents in a gyrotron. We have included such non-ideal characteristics as finite beam thickness, electron velocity spread and magnetic field tapering as well as the effect of magnetic field tapering on beam coupling to the RF fields of a given mode.

7.1 Governing equations for start current

The self-excitation conditions for a gyrotron are fulfilled when the RF power radiated in a given mode exceeds the combined losses in the device. Neglecting non-linear effects, the balance equation for the power of losses and the power radiated by an ideal electron beam with no spread in guiding center radii and velocities can be given by (cf. [37, 18])

$$I_0\chi'' = 1. \tag{7.1}$$

Here χ'' is the imaginary part of the linearized dielectric susceptibility of an electron beam, which will be determined below, and I_0 is a normalized beam current parameter. In accordance with [37], this parameter can be defined as

$$I_0 = 8\frac{eI_b}{\gamma_0 m_0 c^3} Q \frac{\beta_{\perp_0}^{2(s-3)}}{(\pi/\lambda)} \int_0^L |f(z)|^2 dz \left(\frac{s^s}{2^s s!}\right)^2 G(R_b), \tag{7.2}$$

where I_b is the beam current, s is the cyclotron resonance harmonic number, Q is the quality factor accounting for ohmic and diffraction losses, $\beta_{\perp_0}$ is the initial orbital electron velocity normalized to the speed of light, R_b is the electron guiding center radius, the function $f(z)$ describes the axial structure of the resonator field, and $k_\perp$ is the transverse wave number. The last term in (7.2), $G(R_b) = J_{m\pm s}^2(k_\perp R_b)/(\nu^2 - m^2)J_m^2$, is usually called the coupling impedance. Here $\nu = k_\perp R_w$ is the eigenvalue of the operating $TE_{m,p}$ - mode. In a cylindrical cavity of a wall radius R_w, ν is the pth root of the equation $J'_m(\nu) = 0$, which is the boundary condition for a given mode. Use of equations (7.1) and (7.2) also assumes that the axial field profile and quality factor Q are those of the empty (or cold) cavity. Usually this requires that the Q-factor be sufficiently large.

In the framework of the linear theory, the imaginary part of χ for an ideal electron beam propagating in a constant external magnetic field is given by [18]

$$\chi'' = -\left(s + \frac{\partial}{\partial \Delta}\right) \left| \int_0^{\zeta_{out}} f(\zeta) e^{i\Delta\zeta} d\zeta \right|^2. \tag{7.3}$$

Here $\zeta = \pi(\beta_{\perp_0}^2)(z/\lambda)$ is the normalized axial coordinate and ζ_{out} is the exit coordinate of the interaction space; the normalized cyclotron resonance mismatch is $\Delta = (2/\beta_{\perp_0}^2) \cdot ((\omega - s\omega_{H_0})/\omega)$ and ω_{H_0} is the electron cyclotron resonance frequency.

However, in a "real" situation, the magnetic field is not uniform and the electron beam has a finite radial thickness and a finite velocity spread. These factors, when considered, can affect the balance equation (7.2).

The non-uniformity of the magnetic field has two consequences. It causes the normalized cyclotron resonance mismatch Δ and the electron guiding center radius R_b to vary along the axial coordinate. The effect of the axial dependence of $\Delta(\zeta)$, has been considered in [37], which changes the relation for χ'' to

$$\chi'' = -\left(s + \frac{\partial}{\partial \Delta}\right)\left|\int_0^{\zeta_{out}} f(\zeta)\exp\left(i\left(\Delta_0\zeta + \int_0^{\zeta} s\widetilde{\Delta}d\zeta'\right)\right)d\zeta\right|^2. \tag{7.4}$$

Here, we represented Δ as $\Delta_0 + \widetilde{\Delta}$, with Δ_0 being the constant part of the cyclotron resonance mismatch and $\widetilde{\Delta} = (2/\beta_{\perp_0}^2)\cdot((1 - B_0(\zeta))/B_0)$ describing the effect of magnetic field tapering.

When the electron beam has a non-zero radial thickness ΔR_b, electrons with different R_b have different coupling strengths to a mode. In order to take this effect into consideration, we introduce

$$\varphi(R_b) = \frac{J_{m\pm s}(k_\perp R_b)}{J_{m\pm s}(k_\perp \overline{R}_b)}. \tag{7.5}$$

Here $\overline{R}_b \equiv \overline{R}_b(z)$ is the average radial position of the electron beam. Then, an additional averaging over the beam distribution in R_b should be made in (7.1). The average radial position of the beam relative to its position at the entrance to the interaction region can be determined assuming electron guiding centers follow magnetic field lines,

$$\overline{R}_b(z) = \overline{R}_b(0)\sqrt{\frac{B_0(0)}{B_0(z)}}. \tag{7.6}$$

This variation in the radial position of the beam affects the coupling impedance along the axial direction. To take this into account, we introduce

$$\phi[\overline{R}_b(z)] \equiv \frac{J_{m\pm s}[k_\perp(z)\overline{R}_b(z)]}{J_{m\pm s}[k_\perp(0)\overline{R}_b(0)]}. \tag{7.7}$$

So, while the function $\varphi(R_b)$ given by (7.5) describes the effect of beam thickness, the function $\phi[\overline{R}_b(0)]$ describes the effect of magnetic field tapering as well as tapering of the cavity wall radius through $k_\perp(z) = \nu/R_w(z)$. To include the effect of finite beam thickness and variation of radial beam position we have taken the weighted average of the product of χ'' and $G(R_b)$, over the non-zero beam thickness while including the factors $\phi(\zeta)$ and $\varphi(R_b)$ inside the integral in (7.4), which gives

$$\langle \chi'' G \rangle_{R_b} = -G(\overline{R}_b(0)) \left(s + \frac{\partial}{\partial \Delta_0} \right) \left| \int_0^{\zeta_{out}} \hat{f}(\zeta) \int_{\overline{R}_b - \Delta R_b/2}^{\overline{R}_b + \Delta R_b/2} W_R(R_b) \varphi(R_b) dR_b d\zeta \right|^2 \tag{7.8}$$

Here $\langle \cdots \rangle$ indicates the weighted average of a function, $G(\overline{R}_b(0))$ is the interaction impedance for the average electron beam radius at the entrance of the interaction region, $\hat{f}(\zeta) = f(\zeta)\phi(\zeta)exp(i(\Delta_0\zeta + \int_0^\zeta \tilde{\Delta} d\zeta'))$ and $W_R(R_b)$ is the distribution function for the radial beam spread defined such that

$$\int_{\overline{R}_b - \Delta R_b/2}^{\overline{R}_b + \Delta R_b/2} W_R(R_b) dR_b = 1.$$

An electron beam with all electrons having the same total kinetic energy can have a non-uniform distribution of electron velocities in the axial and perpendicular directions constituting a "velocity spread". We shall consider a normalized perpendicular velocity spread for the electron beam (in monoenergetic beams, the axial velocity spread $\Delta\beta_{||}$ can be expressed via $\Delta\beta_\perp$). When the effect of velocity spread is in-

cluded, the balance equation has to be averaged over this spread. This results in the following expression for the start current, I_b^{st}:

$$I_b^{st} = \frac{2\pi(mc^3\gamma_0/e)\cdot(1/\lambda)\int_0^L |f(z)|^2 dz}{[s^s/(2^{s-2}s!)]^2 Q \int_{\beta_{\perp_0}-\Delta\beta_{\perp_0}/2}^{\beta_{\perp_0}+\Delta\beta_{\perp_0}/2} W_\beta(\beta_{\perp_0})\beta_{\perp_0}^{2(s-3)} \langle \chi'' G\rangle_{R_b}\, d\beta_{\perp_0}}. \tag{7.9}$$

Here $W_\beta(\beta_{\perp_0})$ is the distribution function for the velocity spread defined such that

$$\int_{\beta_{\perp_0}-\Delta\beta_{\perp_0}/2}^{\beta_{\perp_0}+\Delta\beta_{\perp_0}/2} W_\beta(\beta_{\perp_0}) d\beta_{\perp_0} = 1.$$

This quantity gives the beam current required to start a growing RF wave for the mode under consideration for a given mean beam energy and electron pitch angle. The relation (7.9) is quite general because it takes into account external magnetic field tapering, tapering in the cavity wall radius, finite beam thickness, beam velocity spread and the cold cavity RF field profile.

Chapter 8

Mode competition in a 140 GHz CPI gyrotron

When a gyrotron is turned on, it takes a finite time for the gun voltage and current to reach the final design value. It is during this rise time that the electromagnetic oscillations start and grow in the cavity of the gyrotron. In a high order mode gyrotron, it is possible that parasitic modes can get excited along with the desired mode during this period. Therefore, it is very important to choose such a start-up scenario which will ensure the excitation of the desired mode and suppress all parasites [47].

The CPI gyrotron under study is a 140GHz, long pulse or CW gyrotron capable of delivering 1MW power in the $TE_{28,7,1}$ - mode. This gyrotron is designed to operate at a beam voltage of 80kV and a beam current of 40A. The initial design has led to the development of a gyrotron that delivers a maximum output power of only 500kW. Tuning the solenoid magnetic field to reach a higher efficiency operating point has

resulted in the generation of an undesired counter-rotating parasitic mode, $TE_{-25,8,1}$. As the quasi-optical mode converter is designed to convert only the co-rotating modes, a power from the contra-rotating mode could not be extracted. In order to study the cause of the dominance of the undesired mode and the possible remedy, extensive simulation analysis were performed using the self-consistent non-stationary code MAGY [48] and start current analysis using the linear theory developed in the last chapter. Some of the conclusions of this study were incorporated when the gyrotron was redesigned. Here, we present in brief the results of this study.

8.1 Initial results of MAGY simulation

For our simulations, we have considered two different magnetic field profiles for which experimental results are available. The difference in magnetic field is less than two percent at the center of the cavity. However, the higher magnitude magnetic field (B_{0_1}) corresponds to the 500kW power output that was observed while the lower magnitude magnetic field (B_{0_2}) corresponds to the higher efficiency design value.

We have assumed that no significant oscillations are triggered below a beam voltage of 50kV, because at lower voltages the beam power associated with electron gyration is too small. So, we started our simulations for both magnetic field profiles from a beam voltage of 50kV. The output data from this simulation was used as the starting point for the next level of simulation when the beam voltage was 55kV. This process was repeated for every 5kV increment in the beam voltage with the

corresponding changes in beam current and orbital to axial electron velocity ratio.

Preliminary investigations involved single mode simulations for the $TE_{28,7,1}$ and $TE_{-25,8,1}$ modes. We found that the output power for both modes and for both axial magnetic field profiles can be of the order of 1 MW. This confirmed our suspicion that the $TE_{-25,8,1}$ mode can be highly competitive. In order to verify if any other modes are involved in the mode competition, the simulations were repeated with triplets of almost equidistant modes, Triplet1 ($TE_{27,7,1}$, $TE_{28,7,1}$, $TE_{29,7,1}$) and Triplet2 ($TE_{-24,8,1}$, $TE_{-25,8,1}$, $TE_{-26,8,1}$). The results showed that only the $TE_{28,7,1}$ - mode is excited in the case of Triplet1 for both magnetic field profiles. In the case of Triplet2 with magnetic field B_{0_1}, $TE_{-26,8,1}$ was first excited between a beam voltage of 55kV and 60kV. At higher voltages, $TE_{-25,8,1}$ - mode was excited which suppressed the $TE_{-26,8,1}$ mode. However, for the magnetic field profile B_{0_2}, only the $TE_{-25,8,1}$ - mode was excited. To verify the effect of the observed $TE_{-26,8,1}$ mode in the presence of both Triplet1 and Triplet2 for the field profile B_{0_1}, the simulations were repeated when both the triplets were present for this magnetic field. The results closely followed those when only Triplet2 is present. Thus, it became clear that only $TE_{-25,8,1}$ is the most important parasite as found experimentally.

After figuring out that the only serious competition is posed by $TE_{-25,8,1}$ - mode, we confined ourselves to the case when only $TE_{28,7,1}$ and $TE_{-25,8,1}$ modes are present. When simulations were performed for the field profile B_{0_1} we found that only the $TE_{-25,8,1}$ - mode was excited (Fig.8.1). This is contrary to the experimental observation where 500 kW of power was observed for the $TE_{28,7,1}$ - mode. However, for the case of field profile B_{0_2} the simulation results were very similar to those with

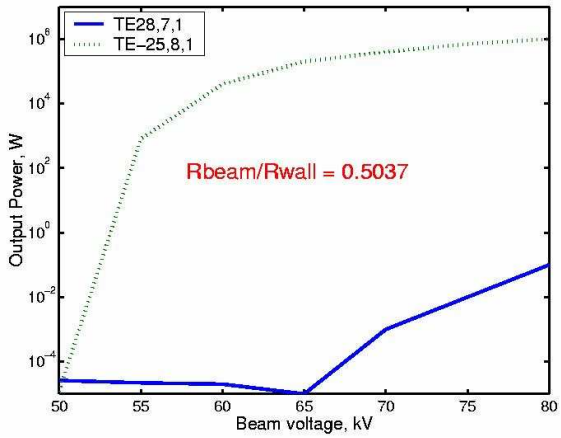

Figure 8.1: Average output power for the $TE_{28,7,1}$ and $TE_{-25,8,1}$ modes with rise in beam voltage for the beam radius used in the experiment with magnetic field profile B_{0_1}. The simulation results for field profile B_{0_2} are very similar.

B_{0_1} (Fig. 8.1) as expected.

8.2 Start current analysis

We shall consider the 140 GHz, fundamental harmonic ($s = 1$), long-pulse gyrotron being developed at CPI for studying the start currents of competing modes using the formalism developed in the previous chapter. Note that, in principle, we can use (7.9) to calculate the start current for any mode at any beam voltage given the pitch factor for the electron beam. From the studies done using the non-stationary code MAGY we have concluded that the only two modes that are of importance to this study are the $TE_{28,7,1}$ and the $TE_{-25,8,1}$ [46]. The electron beam characteristics (voltage, current, pitch-ratio) used in this study were obtained from the simulations of the electron gun using the software EGUN for discrete voltage

values between 50kV and 80kV with 5kV increments [49]. The intermediate data points were interpolated between every two data points. In the results involving start current calculations, where we plot both the electron beam current and the start current as functions of the beam voltage, the first point of intersection of these two curves gives the beam voltage and beam current, at which the corresponding mode is excited. As the cavity fill time Q/ω for the device considered is much shorter than the voltage and current rise times of the device, it is likely that the mode that starts first will grow and, as a result, suppress all other modes. (This is also borne out of nonlinear simulations [46]).

Since we have included many factors in our consideration, it makes sense to analyze them in a successive manner.

A. Effect of radial position on the electron beam

In our search for the reason the $TE_{-25,8,1}$ - mode suppressed the design mode $TE_{28,7,1}$ in the CPI 140 GHz gyrotron that was initially designed, we have studied the interaction impedance for the two modes as a function of radial position. In Fig. 8.2, we have plotted the interaction impedance for the two modes of interest; the beam radius here is normalized to the cavity wall radius. The solid vertical line shows the normalized beam position in the middle of the interaction region ($z = 5$cm). We can see clearly that the beam position at the center of the cavity is favorable for interaction with the $TE_{-25,8,1}$ - mode as it has slightly higher coupling impedance with this mode than for the $TE_{28,7,1}$ - mode.

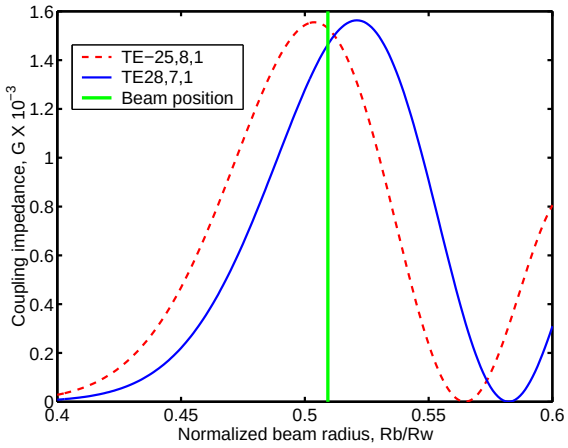

Figure 8.2: Variation of interaction impedance for the two modes with radius normalized to cavity wall radius and the relative position of the beam in the middle of the cavity ($z = 5$cm)

Fig.8.3 shows the interaction impedance for the actual electron beam radial position for the two modes of interest along the interaction length. We can see that at the entrance of the interaction region the $TE_{28,7,1}$ - mode has a larger interaction impedance than the $TE_{-25,8,1}$ - mode but it is lower inside the cavity region. As most of the beam-wave interaction happens in the cavity region, it is likely that the $TE_{-25,8,1}$ - mode dominated in accordance with the experimental results.

In order to see whether the radial position of the beam affects mode competition, we have chosen the radial position of the beam so as to coincide with the peak interaction impedance for the $TE_{28,7,1}$ - mode at the center of the cavity, for interaction impedance studies. In this case, shown in (8.3)b, it is very clear that now the desired mode has a larger interaction impedance than for the $TE_{-25,8,1}$ - mode in the region where most of the beam-wave interaction occurs. From this

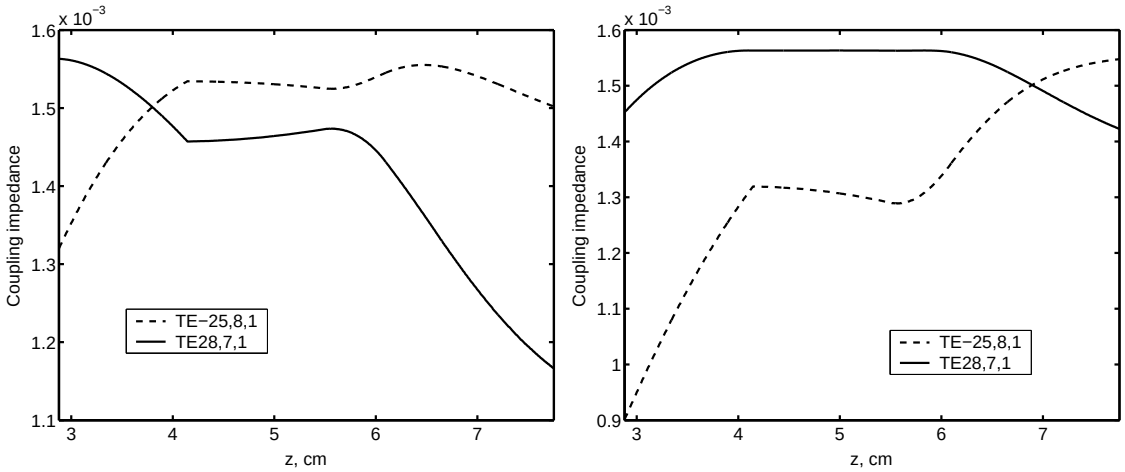

(a) **(b)**

Figure 8.3: Coupling impedance of the electron beam as a function of axial position for two modes with beam radius corresponding to (a) the design value, (b) the peak interaction impedance for $TE_{28,7,1}$ - mode at the center of the cavity

observation, it follows that the radial electron beam position is a very important factor that determines which mode dominates the mode competition and even a 1% variation in this position can play a critical role in the mode competition.

B. Difference between Gaussian and actual $f(z)$

Typically, the axial structure of the RF field $f(z)$ in conventional resonators of length L, open in the axial direction, is described by a Gaussian function with a constant phase (see for example [37, 50]). However, in a gyrotron the RF field profile differs from the ideal Gaussian function. Also, the phase is not constant over the length of the interaction region. Fig. 8.4 shows the typical Gaussian profile and cold cavity profile $|f(z)|$ for $TE_{28,7,1}$ and $TE_{-25,8,1}$ modes of the CPI gyrotron

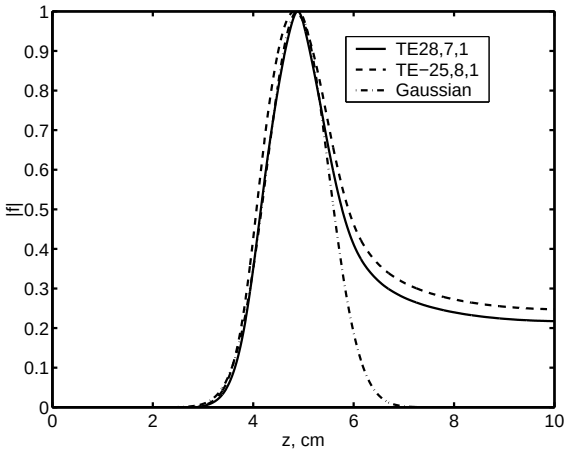

Figure 8.4: Normalized amplitude of cold-cavity RF field profile for $TE_{28,7,1}$, $TE_{-25,8,1}$ modes, and a Gaussian profile

cavity as calculated by MAGY. The cavity length L for the Gaussian function was chosen to match $1/e$ times the maximum value of $|f(z)|$ for the $TE_{28,7,1}$ - mode on the entrance side of the cavity. It can be seen that the cold cavity $|f(z)|$ follows closely that of a Gaussian function only over the entrance side of the interaction region and has higher amplitude towards the exit region. Fig. 8.5 shows the phase of $f(z)$ for the two modes along the axis of the device. The variation of phase along the axis for the two modes is almost the same. The cavity wall has a straight section between $z = 4.14$ cm and $z = 5.52$ cm with a down-taper on the entrance side and a smooth up-taper on the exit side. We will see later how the difference in actual RF field profile from a Gaussian profile affects start current. Note that, in principle, this difference is a known issue (see, for example, [51], chapter 3), but in gyrotrons operating at relatively low-order modes there were some reasons to neglect it.

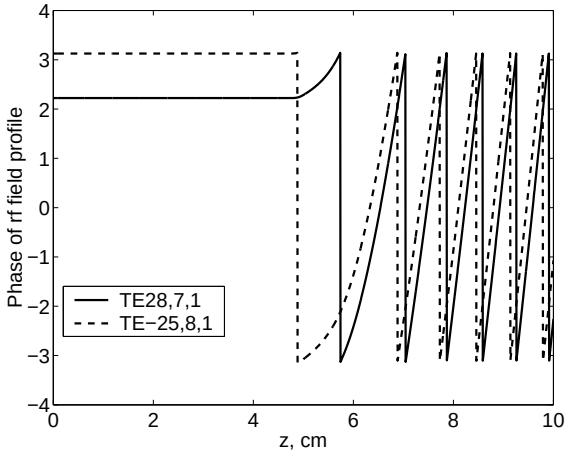

Figure 8.5: Phases of cold-cavity RF field profile for $TE_{28,7,1}$ and $TE_{-25,8,1}$ modes

C. Effect of inhomogeneity of external magnetic field

We have shown in section 7.1 that the inhomogeneity of the external magnetic field can affect the imaginary value of the electron beam susceptibility as well as the coupling impedance.

In order to demonstrate the effect of $B_0(z)$ on start currents we calculated these currents for the simple case of a Gaussian function, $f(z)$, for both modes. In Fig. 8.6 we have plotted the start currents calculated for an interaction length of $2L$ for two cases: (a) when the magnetic field is uniform, equal to the peak value of B_0, the cavity wall radius is constant and equal to the value at the center of the cavity, and the beam radius R_b is equal to its value at the entrance of the interaction region, and (b) for the actual magnetic field profile $B_0(z)$ with the beam radius $R_b(z)$ dependent on $B_0(z)$ (corresponding to the interaction impedance of Fig. 8.3a). A constant cavity wall radius is considered, as in case (a). In both cases, we have considered an "ideal" beam with no electron velocity spread and zero radial beam

thickness.

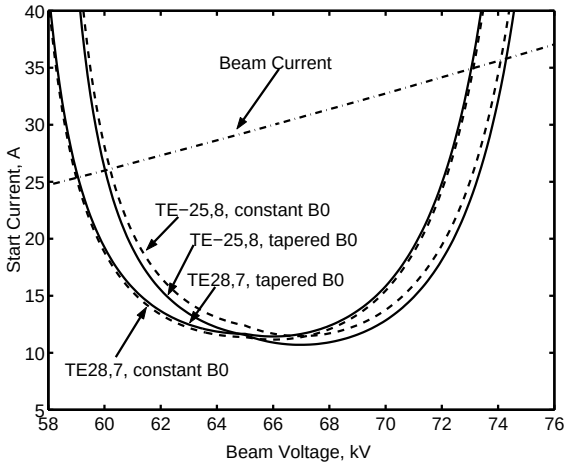

Figure 8.6: Start currents for $TE_{28,7,1}$ and $TE_{-25,8,1}$ modes for a Gaussian RF field profile for both modes for an interaction length equal to $2L$. Dashed curves indicate the start current for a constant magnetic field equal to its peak value, constant cavity wall radius, and beam radius equal to that at the output of the electron gun. Solid curves are for the actual magnetic field profile and cavity wall radius

From Fig. 8.6, we see that a tapered magnetic field $B_0(z)$ has some effect on the start current for the $TE_{-25,8,1}$ - mode and hardly any effect on the $TE_{28,7,1}$ - mode. Our calculations indicate that for a given tapering of the magnetic field, the effect of $B_0(z)$ on detuning Δ alone (and hence on I_b^{st}), is a minor effect compared to that due to the variation of the beam coupling (not shown separately in the figure). The effect of cavity wall tapering $R_w(z)$ is small for a Gaussian RF field profile, as $f(z)$ is very small where $R_w(z)$ is tapered. We have found that the start currents in Fig.8.5 experience very little change when variation in $R_w(z)$ is also considered. But, for a non-Gaussian RF profile, the tapering in $R_w(z)$ can have a considerable

effect on start currents, as we shall see later. Otherwise, in both cases, viz., B_0 constant and $B_0(z)$, the electron beam current line crosses the $TE_{28,7,1}$ - mode start current curve before crossing the $TE_{-25,8,1}$ - mode start current curve, contrary to experimental observation, where $TE_{-25,8,1}$ - mode was the dominant mode.

D. Effect of axial structure of the RF field $f(z)$, its phase variation and interaction length

The actual profile $f(z)$ differs from a Gaussian profile as seen from Fig. 8.4. For all our calculations, we have fixed the entry coordinates of the interaction region at $z = 2.88$ cm. For $z < 2.88$ cm, we see from Fig. 8.4 that $|f(z)|$ has insignificant value, and so has been neglected in our calculations. However, it is much more difficult to fix the exit coordinates in our calculations because it is difficult to accurately predict in advance where the resonant interaction between electrons and outgoing radiation stops. This resonance is disturbed in the output up-taper, first, by the magnetic field decrease, and second by the fact that the phase of $f(z)$ is not constant over the length of the interaction region (Fig. 8.5). The latter fact can lead to some concerns about the validity of our approach, which is based on the use of gyro-averaged equations. For averaging the equations for electron motion over fast gyrations, it is necessary to assume that the changes in phase of $f(z)$ over each cycle of the gyrating electrons are negligibly small. So, this approach is valid only if the electron pitch length is much smaller than the phase cycle of $f(z)$. As we see from Fig. 8.5, the phase of $f(z)$ is constant over some length of the interaction

region near the entrance, then it begins to change with increasing rapidity with z in the output uptapered waveguide. The phase of $f(z)$ varies by 2π over a distance of 8.5 mm around $z = 7$ cm, and 6.5 mm towards the end of the interaction region. The pitch length for the electron beam at 60kV (the beam voltage around which modes of interest get excited), with a pitch factor of 0.9245, is 0.12 mm, which is very small compared to the phase length of $f(z)$. So, the linear theory used in this study may be treated as valid over the entire interaction region.

E. Dependence of start current calculations on the choice of exit coordinate

Though the linear theory is valid over the entire interaction region, considerable variation in start currents was observed depending on where the exit coordinate is fixed. In Fig. 8.7, start currents as a function of beam voltage are plotted for the $TE_{28,7,1}$ - mode (solid line) and $TE_{-25,8,1}$ - mode (dashed line) for four different exit coordinates, (a) $z = 6.36$ cm, (b) $z = 6.9$ cm, (c) $z = 7.35$ cm, and (d) $z = 7.75$ cm. The four exit coordinates correspond to a phase shift of π, 2π, 3π and 4π, respectively, with respect to the phase at the entrance of the cavity for the $TE_{28,7,1}$ - mode. Also, the beam current as a function of beam voltage is plotted in each of the plots of Fig. 8.7 (dash-dotted line). The mode whose start current curve is first intersected by the beam current line starts to grow first and hence is likely to dominate. In Fig. 8.7, we see that there is significant variation in start currents depending on the choice of exit coordinates. Also, we see that for cases (a) and (d),

the beam current line crosses the $TE_{-25,8,1}$ - mode curve at a lower beam voltage than for $TE_{28,7,1}$ - mode. However, for case (c) and (d), it is the other way around. Therefore, from these results, it is difficult to predict which mode dominates, though it clearly suggests the stiff competition between the two modes.

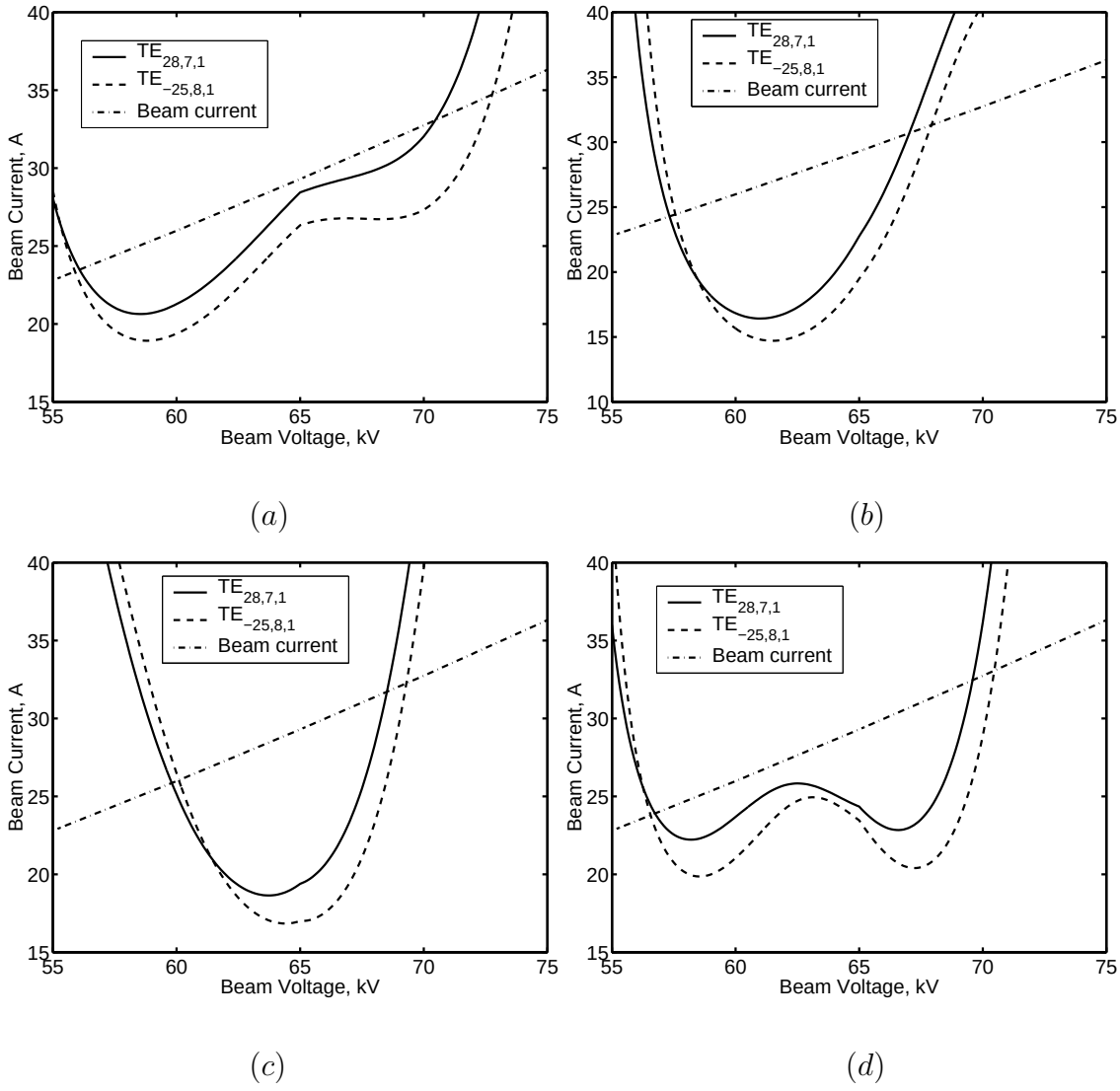

Figure 8.7: Start current as a function of beam voltage for the two competing modes with exit coordinates at (a) $z = 6.36$ cm (b) $z = 6.9$ cm (c) $z = 7.35$ cm (d) $z = 7.75$ cm

Also, it should be noticed that there is a significant difference in the start

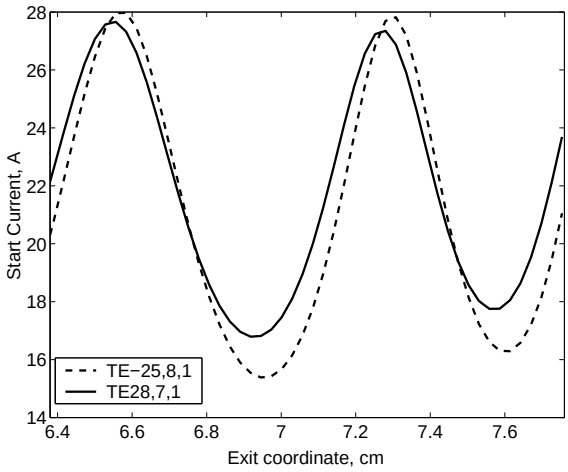

Figure 8.8: Variation of starting current with the choice of the exit coordinate for the two competing modes at a constant beam voltage of 60kV

current values depending on the choice of exit coordinates, at all beam voltages. Fig. 8.8 shows the change in start current, for a fixed beam voltage of 60 kV, with the change in exit coordinate, for both the competing modes. We see that, for a fixed beam voltage, the mode with the lower start current depends on the choice of the exit coordinate. Also, there is a large variation in start current with varying exit coordinate. Thus, it is very difficult to model the up-taper region for start current calculations. The reason for this variation in start current can be attributed to the electrons continuing to exchange energy with the modes in the up-taper region. In the up-taper region, the axial wave number increases with z, due to the growing radius of the waveguide wall. This exchange of energy will continue in z until the combined effects of the increasing axial wave number of the RF fields due to the up-tapered wall radius and the decreasing cyclotron frequency due to the expanding magnetic field lines removes the beam from the cyclotron resonance. Both of these

disturb the cyclotron resonance, although in some specific cases they can compensate each other. We treat this process heuristically by averaging the energy extracted from the electron beam over a range of exit coordinates corresponding to a period of phase variation of $f(z)$ (Fig. 8.5). This corresponds to averaging the denominator of equation (7.9) for the said range of exit coordinates.

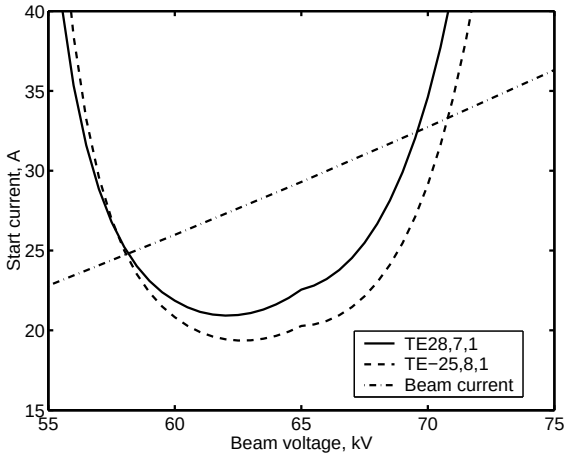

Figure 8.9: Start current as a function of beam voltage for the two competing modes. The denominator of (7.9) is averaged for exit coordinates varying between $z_{max} = 6.36$cm and $z_{max} = 7.35$cm to account for the variation in start currents with the choice of exit coordinate.

Such start currents averaged over varying exit coordinates for the two modes are shown in Fig. 8.9 as functions of the beam voltage. Also shown is the electron beam current. The minimum and maximum exit coordinates were chosen as $z_{max} = 6.36$cm and $z_{max} = 7.35$cm, respectively. We can see that the electron beam line crosses the start current curves of $TE_{28,7,1}$ and $TE_{-25,8,1}$ modes at almost the same beam voltage. The start current for the $TE_{-25,8,1}$ - mode is slightly lower than that

of the $TE_{28,7,1}$ - mode, indicating the possibility for its dominance as observed in the experiment. However, the results of Fig. 8.9 cannot conclusively establish the fact due to the very small margin in the difference in start currents for the two modes and due to the uncertainties in our approximate linear theory.

It should also be noted that for these two modes the start currents shown in Fig. 8.9, as compared to the currents calculated for the Gaussian RF field profiles (Fig. 8.6), are much different. Also the fact that a considerable RF power is outside the cavity region makes the start current greater than for the case of an ideal Gaussian RF field distribution. Moreover, the difference in start currents for the two modes and the sequence of their excitation is different when the actual RF field profile is considered. This indicates that the actual cold-cavity RF field profile not only affects the start current values but also, as in this case, makes the mode competition more acute.

F. Effect of radial beam thickness

A real electron beam has a finite radial beam thickness R_b. Let us find how this thickness affects the start currents and mode competition. In Fig. 8.10, the start currents are plotted as a functions of an RMS radial beam spread expressed as percent of the average beam radius, for fixed beam voltages. We have used a unit rectangular function as the distribution function W_R in (7.9). We have chosen two different voltages, (a) 58.15kV and (b) 70kV, around which the beam current curve crosses the start current curves of the two modes under study (Fig. 8.9). Also, we

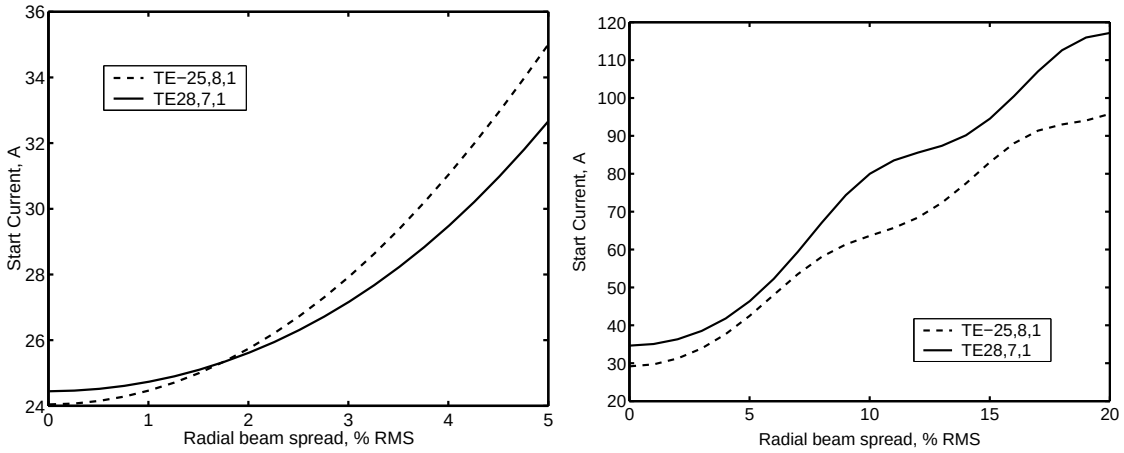

(a) **(b)**

Figure 8.10: Start currents as functions of the radial spread at a constant beam voltage of (a) 58.15kV and (b) 70kV. The denominator of (7.9) is averaged as in Fig.8.9

can observe from Fig. 8.9 that, the margin of difference in start current for the two modes around 58.15kV is much smaller than about 70kV. It should be remembered that the beam voltage corresponding to the first point where the beam current curve crosses the start current curve is the excitation voltage for the corresponding mode. Hence, only the case (a) is of real interest when the question is to determine which mode is excited first, while the case (b) only suggests what might happen if the difference in start currents for the competing modes is large, around the beam voltage where the modes are excited. We see from Fig. 8.10 that the start currents for both modes increase with increasing radial beam spread at both beam voltages. However, in case (a), the $TE_{28,7,1}$ - mode has a lower rate of increase in the start current than the $TE_{-25,8,1}$ - mode and, as the radial spread increases beyond 1.75%, the $TE_{28,7,1}$ - mode attains a lower start current than the $TE_{-25,8,1}$ - mode. The

RMS radial spread for the electron beam used in the device under study is about 1.2%. We see that the radial spread in the device and the radial spread that can affect mode competition for this device are of the same order. But, in the case (b), for all reasonable values of the spread in the beam radii, the $TE_{-25,8,1}$ - mode has lower start current than the $TE_{28,7,1}$ - mode. This implies that the radial spread can affect the sequence of mode excitation and hence mode competition only if the margin of difference in start current for the competing modes is very small (case (a)) and is largely unaffected when the difference is very large (case (b)). For the particular device being studied, it is clear that the radial spread can be a real issue in the mode competition. (This issue is analyzed in more detail in [42]).

G. Effect of electron velocity spread

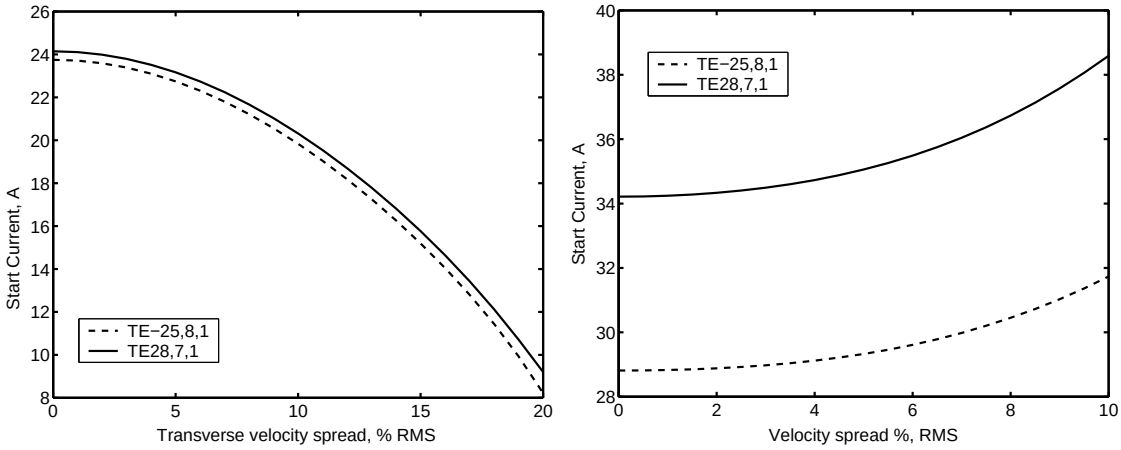

(a) **(b)**

Figure 8.11: Start current as a function of electron velocity spread at a constant beam voltage of (a) 58.15kV (mean value of $\alpha = 0.89$) and (b) 70kV (mean value of $\alpha = 1.25$). The denominator of (9) is averaged as in Fig.8.9

In addition to a finite beam thickness in a real electron beam, there exists a finite velocity spread. To study the effect of electron velocity spread on start currents we have chosen the same fixed beam voltages as we did in the study of the beam spread in radii. The velocity distribution in (7.9) was described by a triangular function W_β . Fig.8.11a shows the start currents for the two modes as functions of the RMS velocity spread for a beam voltage of 58.15 kV, which is the excitation voltage for both modes (Fig. 8.11). As seen in Fig. 8.11a, as the velocity spread increases, the start current for both modes decreases, while one might expect an increase in the start current due to deterioration in the electron beam quality. This can be explained by the fact that the susceptibility increases due to the presence of electrons with smaller axial velocities more than it decreases from the appearance of electrons with larger axial velocities. Indeed, first, the electrons with small axial velocities interact with the cavity field longer, and second, these particles have higher transverse velocity, thus further enhancing their contribution to the susceptibility.

Such reduction in start currents was also found in [51]. According to Fig. 8.3 of [51], for large values of beam pitch angle ($\alpha > 2$) the start currents, in general, increase with the velocity spread. However, when the pitch angle gets smaller, the start current first reduces at small velocity spreads, and then increases at larger spreads. In [51], the results were given for $\alpha \geq 2$. Our simulations done for $\alpha \leq 1$ (for a beam voltage of 58.15 kV, $\alpha = 0.89$) show that the reduction in the start current with the velocity spread shown in Fig. 8.9a takes place for all practical ranges of the spread in real beams.

Note that the start currents for both modes reduce at almost the same rate

with the increase in velocity spread. This indicates that electron velocity spread should have little effect on the mode competition in this case. Fig. 8.11b shows a plot where the beam voltage considered is 70kV. Here we see that the start currents increase for both modes with the increase in velocity spread, while not affecting the sequence of mode excitation. So, we see that the increase or decrease in start currents with the velocity spread depends on the beam voltage and pitch angle.

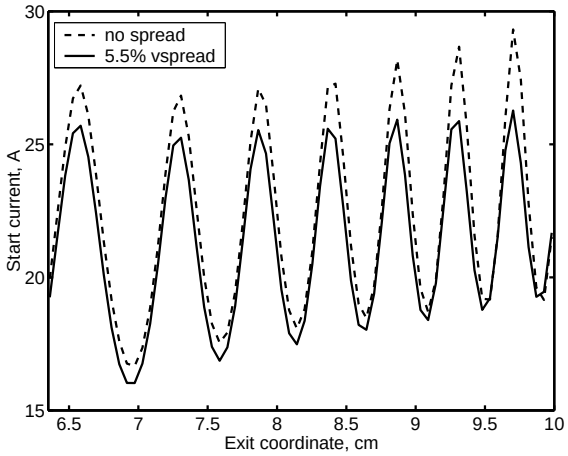

Figure 8.12: Variation of start current with the choice of exit coordinate for the $TE_{28,7,1}$ - mode at a constant beam voltage of $60kV$ for an ideal beam (dashed line) and a beam with 5.5% velocity spread (solid line)

The interaction of electrons with the outgoing radiation which propagates in the uptapered waveguide should be affected by an electron velocity spread stronger than in a regular cavity. This is because the axial wave number of the EM wave increases with the waveguide radius in the uptaper region. Correspondingly, the effect of the axial velocity spread on the Doppler term, $k_z v_z$, in the cyclotron resonance condition becomes more pronounced. Roughly, one can expect significant smoothing

of the oscillations in the start currents shown in Fig. 8.8 when at one period of these oscillations, d (about 0.7 cm, see Fig. 8.8), the velocity spread causes the deviation in the Doppler term, $k_z d(\Delta v_z/v_{z0})$, on the order of π. This statement is illustrated by Fig. 8.12 where we have plotted the start currents for the $TE_{28,7,1}$ - mode for the case of an ideal beam (dashed line) and with an electron velocity spread of 5.5% (solid line). It can be seen from Fig. 8.12 that the velocity spread gradually reduces the oscillations in the start current with the change in exit coordinates.

H. Studies on new design

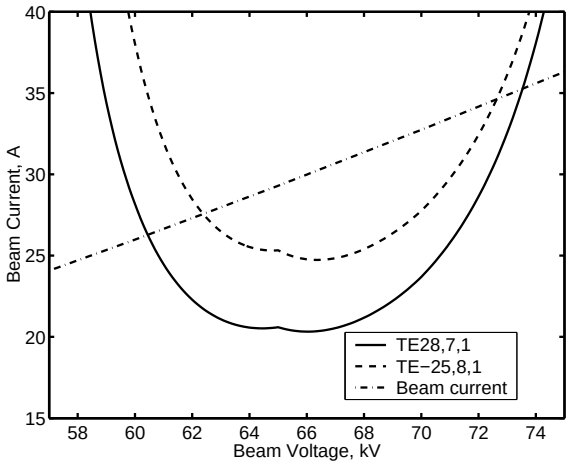

Figure 8.13: Start current as a function of beam voltage for the two competing modes for the redesigned cavity. The denominator of (7.9) is averaged as in Fig.8.9.

In the new design for the gyrotron that is being built, CPI has redesigned the interaction cavity, gun position and magnetic field profile so that the beam is positioned for maximum interaction with the $TE_{28,7,1}$ - mode inside the cavity. In

addition, the cavity up-taper in the new design has been made sharper than in the old cavity to improve mode stability. We have repeated some of the studies that were performed on the initial design considered until now for the new design also. In Fig. 8.13, start currents for the two competing modes $TE_{28,7,1}$ and $TE_{-25,8,1}$ in a gyrotron with an ideal electron beam are shown as functions of the electron beam voltage. This plot corresponds to Fig. 8.9, where the initially designed cavity was considered. It is clearly evident that now the $TE_{28,7,1}$ - mode has unambiguously lower start current than the $TE_{-25,8,1}$ - mode due to preferred radial positioning of the electron beam to interact with the $TE_{28,7,1}$ - mode. As there is a sufficient margin of difference in start currents for the two modes, it is unlikely that such effects as the radial spread and electron velocity will cause the $TE_{-25,8,1}$ - mode to start before the $TE_{28,7,1}$ - mode.

We have also performed MAGY simulations to study the start-up scenario for the new design in the presence of two triplets of modes, Triplet1 ($TE_{-24,6,1}$, $TE_{-25,6,1}$, $TE_{-26,6,1}$) and Triplet2 ($TE_{27,7,1}$, $TE_{28,7,1}$, $TE_{29,7,1}$). We have started the simulations at 50 kV beam voltage and after reaching steady state for all the modes the beam voltage was incremented by 2 kV (along with the corresponding beam current and pitch factor). Using the steady state conditions of the preceding simulations at 50 kV as the starting conditions the simulations was repeated. The process was repeated in 2 kV increment until the final design voltage of 80 kV was reached. In Fig. 8.14 we show the results of the simulations starting from 64 kV. We find that there is no significant power in any of the competing modes for voltages less than 64 kV (the simulation results for those beam voltages are not shown in

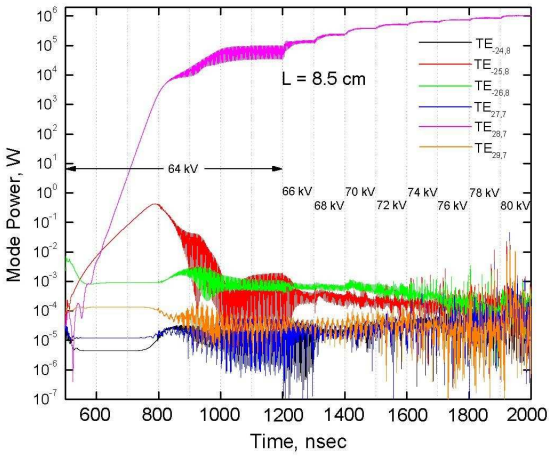

Figure 8.14: Two triplets of modes, Triplet1 ($TE_{-24,6,1}, TE_{-25,6,1}, TE_{-26,6,1}$) and Triplet2 ($TE_{27,7,1}, TE_{28,7,1}, TE_{29,7,1}$), considered in MAGY simulations to study start-up scenario in the new design. $TE_{28,7,1}$ - mode is established suppressing all other modes. (Simulations by Oleksandr Sinitsyn)

the figure). We can see from Fig.8.14 that the design mode $TE_{28,7,1}$ - mode is the dominant mode and is established much before the final beam voltage is reached. No other mode offers any serious competition to the design mode.

From these results we can see that in the new design, $TE_{28,7,1}$ - mode will be the dominant mode in the new design of the CPI 140 GHz gyrotron. CPI has experimentally verified that indeed this mode is dominant.

Chapter 9

Conclusions

This work may be broadly divided into two parts.

- Theory of gyro-peniotron oscillator and the possibility of its self excitation
- Start-up scenario in a 140 GHz gyrotron developed by Communication and Power Industries

9.1 Gyro-peniotron

In a Cyclotron Resonance Maser (CRM), two energy exchange mechanisms viz., O-type interaction and M-type interaction, are recognized. O-type interaction causes electron bunching while M-type interaction causes electron segregation. Gyrotrons whose operation is based on O-type interaction are capable of delivering very large RF power (> 1 MW) at frequencies greater than 100 GHz, as the interaction cavity can have a smooth walled cylindrical structure with a high energy annular electron beam. However, the efficiency of gyrotrons is limited due to the fact that

all electrons are not gathered in bunches and those electrons outside the bunches absorb energy from the RF wave. The gyro-peniotron whose operation is based on M-type interaction also requires a smooth-walled cylindrical waveguide and an annular beam of electrons. It has been shown that a gyro-peniotron has the potential to operate at very high efficiencies because in a M-type interaction there are no "bad" electrons that absorb energy from the RF wave. However, as the M-type interaction is weaker than O-type interaction, gyrotron modes invariably suppress gyro-peniotron modes. Due to this mode competition from gyrotron modes, it has not been possible to build a working gyro-peniotron, to date.

In this work we have developed a non-linear of a CRM device with a smooth-walled cylindrical interaction cavity and an annular beam of electrons. We have developed this theory from first principles and showed that a gyro-peniotron mode has a possibility of self excitation even when the electron guiding center radius is at the RF null of the operating mode.

Using the linear approximation of the nonlinear theory we have studied the self excitation conditions for a gyro-peniotron for various device parameters. We have also considered the self excitation conditions for $TE_{-2,2}$ and $TE_{-3,2}$ - modes that are adjacent to the $TE_{0,2}$ - mode in the eigenvalue spectrum of the interaction waveguide, to see the possibility of mode competition. We have found that the minimum cavity Q required to excite the $TE_{-2,2}$ and $TE_{-3,2}$ - modes is much smaller than that of the $TE_{0,2}$ - mode operating in the gyro-peniotron regime. However, for the range of parameters over which the $TE_{0,2}$ - gyro-peniotron mode can operate, the two adjacent $TE_{-2,2}$ and $TE_{-3,2}$ - modes do not satisfy the self excitation conditions.

This leads to the exciting possibility of a self excitable gyro-peniotron that can potentially deliver very high RF energy with very high efficiency.

We have also studied the single mode evolution of a $TE_{0,2}$ - gyro-peniotron mode. The results confirm the conclusions of the linear theory that a gyro-peniotron can be self excited in the linear regime. We have also found that for the design parameters used in the simulation, a saturation trnasverse efficiency greater than $> 90\%$ is possible for a gyro-peniotron oscillator.

9.2 Start-up scenario in a 140 GHz CPI gyrotron

In the design of gyrotrons operating in high order modes in the presence of a dense spectrum of competing modes it is extremely important to make a systematic study of the start-up scenario in order to determine that the desired mode alone dominates while suppressing all other modes. In this work we have presented a study of starting currents of competing modes using a linear analysis that includes the effect of tapering of magnetic field profile, cavity wall tapering, phase variation in RF field profile and finite beam thickness, as well as electron beam velocity spread. Also, we have considered a Gaussian RF field profile as well as the RF cold-cavity field profile obtained from MAGY simulations for an actual device being built at CPI. It is seen that the start currents differ considerably for the case of a realistic field profile compared with the case of Gaussian field profile. The effects of the non-zero beam thickness and velocity spread have also been studied.

In this work we have presented the results of our study for a 140 GHz gyrotron

operating in the $TE_{28,7,1}$ - mode. From experimental results, we know that the $TE_{-25,8,1}$ - mode, and not the $TE_{28,7,1}$ - mode, had dominated over all the other modes. The start current analysis presented in this paper indicates that the $TE_{-25,8,1}$ - mode has a slightly lower start current than the $TE_{28,7,1}$ - mode, suggesting the reason as to why this mode was excited in the experiment. However, the difference in start current is so small that less than 2% spread in beam radius could change the sequence in which the two modes excite, though a reasonable electron velocity spread did not affect mode competition. Moreover, when the difference in the start currents of competing modes is very small, any non-linear effect can swing the advantage in favor of any mode, which cannot be accounted for in the framework of the linear theory. Thus, there is an ambiguity as to which of these two modes $TE_{28,7,1}$ and $TE_{-25,8,1}$ will be excited in the device due to the very severe mode competition. From these results it is hard to predict which mode dominates. Being a counter rotating mode, the $TE_{-25,8,1}$ - mode could have been trapped inside the tube and reflections back into the cavity may have served to increase the advantage decisively in its favor. In any case, in order to ensure the dominance of the required mode, the design should be such that that mode has, unambiguously, the lowest start current for any interaction length with a sufficiently large start current margin from the nearest competing mode.

From the studies of the interaction impedance for the competing modes and the beam position in the cavity, we have found that it is highly critical to position the beam such that there is maximum interaction with the desired mode. When the beam radius is adjusted for maximum interaction with the desired mode inside the

cavity, it is found in our calculations that the start current required for the $TE_{28,7,1}$ - mode is unambiguously less than that for the $TE_{-25,8,1}$ - mode.

As was mentioned, CPI has redesigned the device with modifications in the axial magnetic field profile, gun position and cavity profile. Our studies have shown that in this new design, the desired mode will dominate during the start up and this has been demonstrated in the experiments

So, for any design of a high-order mode gyrotron, in order to make sure that the desired mode dominates, the radial beam position, magnetic field tapering and cavity profile have to be carefully designed such that the desired mode always has lower start current than any other mode with as much margin as possible from the closest competing mode.

Bibliography

[1] V. A. Flyagin and G. S. Nusinovich, "Gyrotron oscillators," *IEEE Trans. Plasma Sci.*, vol. 76, no. 6, pp. 644–656, June 1988.

[2] S. Ono, K. Tsutaki, and T. Kageyama, "Proposal of a high efficiency tube for high power millimeter wave generation: The gyro-peniotron," *Int. J. Electronics*, vol. 56, no. 4, pp. 507–519, 1984.

[3] A. Gaponov, "Interaction of irrectilinear electron beams with electromagnetic waves in transmission lines," *Izv. VUZov, Radiofizika*, vol. 2, no. 3, pp. 450–462, 1959.

[4] R. Q. Twiss, "Radiation transfer and the possibility of negative absorption in radio astronomy," *Aust. J. Phys*, vol. 11, pp. 564–79, 1958.

[5] J. Schneider, "Stimulated emission of radiation by relativistic electrons in a magnetic field," *Physical Review Letters*, vol. 2, p. 504, 1959.

[6] A. Gaponov, M. Petelin, and V. Yulpatov, "The induced radiation of excited classical oscillators and its use in the high frequency electronics," *Radiophys. and Quantum Electron*, vol. 10, pp. 794–813, 1967.

[7] M. Read, R. Gilgenbach, J. R.F. Lucey, K. Chu, A. Drobot, and V. Granatstein, "Spacial and temporal coherence of a 35-ghz gyromonotron using the TE_{01} circular mode," *IEEE Trans. Microwave Theory Tech.*, vol. 28, no. 8, pp. 875–978, August 1980.

[8] K. L. Felch, B. G. Danly, H. R. Jory, K. E. Kreischer, W. Lawson, B. Levush, and R. J. Temkin, "Characteristics and applications of fast-wave gyrodevices," *Proc. IEEE, New vistas for vacuum electronics*, vol. 87, pp. 752–781, May 1999.

[9] G. S. Nusinovich, *Physics of gyrotrons.* Johns Hopkins University Press, 2004, ch. 6,13.

[10] A. Singh and D. S. Weile and S. Rajapatirana and V. L. Granatstein, "Integrated design of depressed collectors for gyrotrons," *IEEE Trans. Plasma Sci.*, vol. 25, no. 3, pp. 480–491, 1997.

[11] K. Yamanouchi, S. Ono, and Y. Shibata, "Cyclotron fast wave tube. The double ridges travelling wave peniotron," in *Proc. 5th Int. Congr. on Microwave Tubes*, Paris, France, 1964, pp. 96–102.

[12] K. R. Chu and J. L. Hirshfield, "Comparative study of the axial and azimuthal bunching mechanisms in electromagnetic cyclotron instabilities," *Phys. Fluids*, vol. 21, no. 3, pp. 461–466, 1978.

[13] R. H. Pantell, "Electron beam interaction with fast waves," *Proceedings of the Symposium on Millimeter Waves*, pp. 301–311, April 1959.

[14] E. Weibel, "Spontaneously growing transverse waves in a plasma due to anisotropic velocity distribution," *Physical Review Letters*, vol. 2, pp. 82–83, 1959.

[15] A. V. Gaponov, "Instability of a system of excited oscillators with respect to electromagnetic perturbations," *Sov. Phys. JETP*, p. 232, 1961.

[16] V. Y. Davydovskii, "The possibility of accelerating charged particles by electromagnetic waves in a constant magnetic field," *Sov. Phys. JETP*, vol. 16, no. 3 (9), p. 629, 1963.

[17] A. A. Kolomenskii and A. N. Lebedev, "Autoresonance motion of particles in a plane electromagnetic wave in a constant magnetic field," *Sov. Phys. JETP (Engl Transl.)*, vol. 145, no. 7, p. 745, 1963.

[18] M. I. Petelin, "On the theory of ultrarelativistic cyclotron self-resonance masers," *Radiophys. and Quantum Electron.*, vol. 17, no. 6, pp. 685 – 689, Jun 1974.

[19] V. L. Bratman, N. S. Ginzburg, G. S. Nusinovich, M. I. Petelin, and P. S. Strelkov, "Relativistic gyrotrons and cyclotron autoresonance masers," *Int. J. Electronics*, vol. 51, no. 4, pp. 541–567, 1981.

[20] K. D. Pendergast, B. G. Danly, R. J. Temkin, and J. S. Wurtele, "Self-consistent simulation of cyclotron autoresonance maser amplifiers," *IEEE Trans. Plasma Sci.*, vol. 16, pp. 122–128, 1988.

[21] K. R. Chu and A. T. Lin, "Gain and bandwidth of the gyro-TWT and CARM amplifiers," *IEEE Trans. Plasma Sci.*, vol. 16, no. 2, pp. 90–104, 1988.

[22] J. M. Baird, L. R. Barnett, R. C. Grow, and R. C. Freudenberger, "Harmonic auto-resonant peniotron (HARP) interactions," *IEDM Tech. Dig. (Washington, DC)*, pp. 913–916, 1987.

[23] K. Yokoo, S. Musyoki, N. Sato, and S. Ono, "Auto-resonant peniotron amplifier with a down tapered DC magnetic field," *Int. J. Electronics*, vol. 69, no. 6, pp. 827–834, 1990.

[24] K. Yokoo, Y. Nakazato, N. Sato, and S. Ono, "The autoresonant peniotron with a quadrupole interaction circuit," *IEEE Trans. Electron Devices*, vol. 38, no. 12, pp. 2677–2681, 1991.

[25] N.Sato, O. Kamohara, K. Sagae, and K. Yokoo, "Experiments of autoresonant peniotron using a parallel transmission line with double pairs of ridges," *IEEE Trans. Plasma Sci.*, vol. 30, no. 3, pp. 859–864, Jun 2002.

[26] V. L. Bratman, G. G. Denisov, B. D. Kol'chugin, S. V. Samsonov, and A. B. Volkov, "Experimental demonstration of high-efficiency cyclotron-autoresonance-maser operation," *Physical Review Letters*, vol. 75, no. 17, pp. 3102–3105, Oct 1995.

[27] P. Vitello and K. Ko, "Mode competition in the gyro-peniotron oscillator," *IEEE Trans. Plasma Sci.*, vol. PS-13, no. 6, pp. 454–463, Dec 1985.

[28] Q. Li, S. Park, and J. Hirshfield, "Theory of gyrotron traveling-wave amplifiers," *IEEE Trans. Microwave Theory Tech.*, vol. 34, no. 10, pp. 1044–1058, October 1986.

[29] A. P. Chetverikov, "Intensification of electromagnetic oscillations in a gyropeniotron," *Radiophys. and Quantum Electron.*, vol. 33, no. 6, pp. 741–746, Jun 1990.

[30] B. N. Basu, *Electromagnetic theory and applications in beam-wave electronics.* World Scientific, 1995, ch. 8.

[31] M. I. Petelin and V. K. Yulpatov, "Linear theory of a monotron cyclotron-resonance maser," *Radiophys. and Quantum Electron.*, vol. 18, no. 2, pp. 290–299, Feb 1975.

[32] G. Dohler, "Peniotron interactions in gyrotrons. I. qualitiative analysis," *Int. J. Electronics*, vol. 56, no. 5, pp. 617–627, 1984.

[33] ——, "Peniotron interactions in gyrotrons. II. qualitative analysis," *Int. J. Electronics*, vol. 56, no. 5, pp. 629–640, 1984.

[34] G. S. Nusinovich, "Mode interaction in gyrotrons," *Int. J. Electronics*, vol. 51, pp. 457–474, 1981.

[35] M. Yeddulla, G. Nusinovich, and T.M. Antonsen, Jr., "Start currents in a overmoded gyrotron," *Phys. Plasmas*, vol. 10, no. 11, pp. 4513–4520, November 2003.

[36] G. S. Nusinovich, O. V. Synitsyn, L. Velikovich, M. Yeddulla, T. M. Antonsen Jr., A. N. Vlasov, S. R. Cauffman, and K. Felch, "Startup scenarios in high-power gyrotrons," *IEEE Trans. Plasma Sci.*, vol. 32, no. 3, pp. 841–852, June 2004.

[37] G. S. Nusinovich, "Linear theory of a gyrotron with weakly tapered magnetic field," *Int. J. Electronics*, vol. 51, pp. 127–135, 1988.

[38] K. Chu, A. Drobot, H. Szu, and P. Sprangle, "Theory and simulation of the gyrotron traveling wave amplifier operating at cyclotron harmonics," *IEEE Trans. Microwave Theory Tech.*, vol. 28, no. 4, pp. 313–317, April 1980.

[39] P. S. Rha, "Self-consistent large-signal theory and simulation of high harmonic gyrotron and peniotron oscillators operating in a magnetron type open cavity," Ph.D. dissertation, University of Utah, Dec 1986.

[40] M. Abromowitz and I. A. Stegun, Eds., *Handbook of Mathematical Functions*. New York: Dover Publications, Inc.,, 1972.

[41] J. M. Baird, *High-power microwave sources*, V. L. Granatstein and I. Alexeff, Eds. Boston and London: Artech House, 1987.

[42] B. G. Danly and R. J. Temkin, "Generalized nonlinear harmonic gyrotron theory," *Phys. Fluids*, vol. 20, no. 2, pp. 561–567, 1986.

[43] G. S. Nusinovich, M. Yeddulla, L. Velikovich, and T. M. Antonsen Jr., "Start-up scenarios in high-power gyrotrons," in *27th International Conference on IRMMW*, R. Temkin, Ed., MIT, Cambridge, MA, USA, 2002, pp. 329–330.

[44] B. Levush and T. M. Antonsen Jr., "Mode competition and control in high-power gyrotron oscillators," *IEEE Trans. Plasma Sci.*, vol. 18, no. 3, pp. 260–272, 1990.

[45] D. R. Whaley, M. Q. Tran, S. Alberti, T. M. Antonsen Jr., and C. Tran, "Startup methods for single-mode gyrotron operation," *Physical Review Letters*, vol. 75, p. 1304, 1995.

[46] M. Yeddulla, G. S. Nusinovich, T. M. Antonsen Jr., A. N. Vlasov, K. Felch, and S. Cauffman, "Start-up scenario in a 140 GHz gyrotron," in *27th International Conference on IRMMW*, R. J. Temkin, Ed., San Deigo, CA, USA, Sept 2002, pp. 9–10.

[47] G. Nusinovich, "Review of the theory of mode interaction in gyrodevices," *IEEE Trans. Plasma Sci.*, vol. 27, no. 2, pp. 313–326, April 1999.

[48] M. Botton, T. M. Antonsen, Jr., B. Levush, K. T. Nguyen, and A. N. Vlasov, "MAGY: A time-dependent code for simulation of slow and fast microwave sources," *IEEE Trans. Plasma Sci.*, vol. 26, no. 3, pp. 882–892, Jun 1998.

[49] S. Cauffmann, "Voltage current characteristics of the electron gun used in a cpi 140 ghz gyrotron," Personal communications, 2003.

[50] K. Kreischer and R. Temkin, "Mode excitation in a gyrotron operating at the fundamental," vol. 2, no. 2, pp. 175–196, 1981.

[51] E. Borie, *Gyrotron oscillators, their principles and practice.* Taylor & Francis Ltd., 1993, ch. 3, pp. 45–86.